DEUTSCHES ELEKTRONEN-SYNCHROTRON

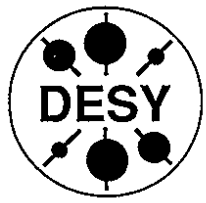

DESY 95-025
March 1995

Physics Results from the First Electron-Proton Collider HERA

A. De Roeck

Deutsches Elektronen-Synchrotron DESY, Hamburg

ISSN 0418-9833

NOTKESTRASSE 85 - 22607 HAMBURG

To be sure that your preprints are promptly included in the
HIGH ENERGY PHYSICS INDEX,
send them to (if possible by air mail):

DESY **Bibliothek** **Notkestraße 85** **22607 Hamburg** **Germany**	**DESY-IfH** **Bibliothek** **Platanenallee 6** **15738 Zeuthen** **Germany**

DESY 95-025
March 1995

ISSN 0418-9833

PHYSICS RESULTS FROM THE FIRST ELECTRON-PROTON COLLIDER HERA *

Albert De Roeck

Deutsches Elektronen-Synchrotron DESY, Hamburg

1 Introduction

On the 31st of May 1992 the first electron-proton (ep) collisions were observed in the H1 and ZEUS experiments at the newly commissioned high energy collider HERA, in Hamburg, Germany. HERA is the first electron-proton collider in the world: 26.7 GeV electrons collide on 820 GeV protons, yielding an ep centre of mass system (CMS) energy of 296 GeV. Already the results from the first data collected by the experiments have given important new information on the structure of the proton, on interactions of high energetic photons with matter and on searches for exotic particles. These lectures give a summary of the physics results obtained by the H1 and ZEUS experiments using the data collected in 1992 and 1993.

Electron-proton, or more general lepton-hadron experiments, have been playing a major rôle in our understanding of the structure of matter for the last 30 years. At the end of the sixties experiments with electron beams on proton targets performed at the Stanford Linear Accelerator revealed that the proton had an internal structure.[1] It was suggested that the proton consists of pointlike objects, called partons.[2] These partons were subsequently identified with quarks which until then were only mathematical objects for the fundamental representation of the SU(3) symmetry group, used to explain the observed multiplets in hadron spectroscopy.[3] This process of probing the internal structure of the proton with lepton beams, termed deep inelastic scattering (DIS), has made a substantial contribution to the development of modern high energy physics over the last three decades. In particular, in addition to the discovery of the partonic content of hadrons, it was established that the quarks carry only about 1/2 of the momentum of the proton (the other half later assumed to be carried by gluons), have a spin of 1/2 and carry fractional electric charge. It was also found that the evolution of the parton momentum distributions in nucleons could be described by perturbative QCD. Furthermore weak neutral currents were discovered. In all, lepton-hadron interactions have proven to be an important testing ground for QCD and the electroweak theory.

*Lectures given at "Frontiers in Particle Physics" Cargese, August 1994

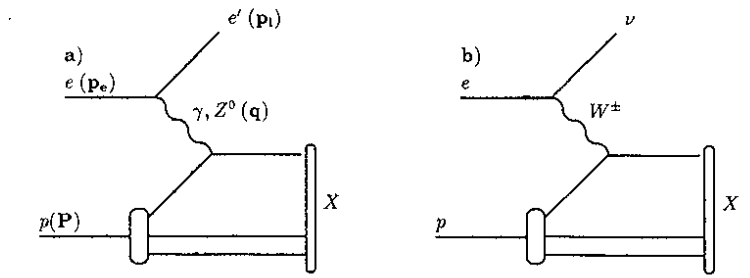

Figure 1: Deep inelastic scattering at HERA for (a) a neutral current process, (b) a charged current process.

The basic processes for deep inelastic scattering at HERA are depicted in Fig. 1, using the language of Feynman diagrams and the Quark Parton Model (QPM). The incoming electron interacts via the exchange of a γ, Z^0 or W boson with a quark of the proton. This quark – often referred to as *current quark* – is being kicked out of the proton, leaving behind a *proton remnant*. Both the current quark and the proton remnant hadronize into a hadronic final state, X in Fig. 1. The proton remnant essentially continues into the proton direction, and will to some extent remain undetected due to the beampipe holes which are inevitable for detectors at a collider. Since both the struck quark and remnant are coloured, one expects a colour connection between these objects. We expect therefore that the region between struck quark and remnant will be filled with particles.

Processes where a photon or Z^0 boson is exchanged (Fig. 1a) are termed *neutral current processes*, while processes where a W boson is exchanged (Fig. 1b) are termed *charged current processes*. For the latter the outgoing lepton is a neutrino ν. At fixed CMS energy, $\sqrt{s}$, the kinematics of the inclusive ep scattering process, $ep \to lX; l = e, \nu$, is determined by two independent variables, conventionally chosen to be two of x, y and Q^2. These kinematical variables are defined as follows:

$$Q^2 = -q^2 = -(p_e - p_l)^2, \quad x = \frac{Q^2}{2P.q}, \quad y = \frac{P.q}{P.p_e}, \quad W^2 = (q+P)^2 = Q^2\frac{1-x}{x} + {m_p}^2, \quad (1)$$

where Q^2 is the (minus) four-momentum transfer squared, x the Bjorken-x, y the fraction of the electron energy transfered to the proton in the proton rest system, and W^2 the hadronic invariant mass squared of the system X. In the naïve quark parton model, i.e. the parton model with no QCD effects, the x variable measures the fraction of the proton momentum carried by the struck quark. In these definitions p_e, p_l and P denote the four-momenta of the incoming and scattered lepton and the incoming proton respectively, as indicated in Fig. 1. At HERA the centre of mass system energy squared $s = 4E_eE_p = 87\,600$ GeV^2, with E_e and E_p the energy of the incoming electron and proton respectively. The deep inelastic regime is generally taken to be that part of the phase space where Q^2 and W^2 are larger than a few GeV^2. As Q approaches the mass of the heavy W and Z^0 bosons, the cross section for W and Z^0 exchange become competitive with the γ-exchange. For small Q, well below these masses, the photon exchange diagram dominates the cross section by orders of magnitude. As an illustration, the analyses of the H1 and ZEUS experiments contain at present a few ten thousand neutral current events and only a few tens of charged current events.

The resolution to resolve the internal structure in the proton is determined by the four-momentum transfer $Q = \sqrt{-q^2}$ between the lepton and the hadron, where q is the four-momentum vector of the exchanged boson in Fig. 1. The smallest distance a virtual photon can resolve is proportional to $1/Q$. The maximum value for the four-momentum transfer Q_{max} is given by the centre of mass energy of the collision $\sqrt{s}$. For example for the "first DIS experiments" at SLAC, the incident electron energy was about 20 GeV, which yields a centre of mass energy (and Q_{max}) of about 6 GeV. Thus distances of the order of 10^{-14} cm, i.e. ten times smaller than the radius of the proton, could be resolved and revealed a new partonic substructure of matter. The obvious question arises: what will happen if still smaller distances are probed? Will a new underlying structure in the partons appear? In order to increase the resolving power experiments with muon and neutrino beams of several hundreds of GeV were used to probe matter, resolving distances of 10^{-15} cm. So far no new substructure has been detected and the quarks and leptons are still considered to be pointlike particles, but deep inelastic scattering has contributed to answering many important questions on the fundamental nature of matter, as mentioned above. HERA is the new frontier for DIS, with a gain in Q^2 of two orders of magnitude, such that a spatial resolution of 10^{-16} cm can be reached. As will be explained in chapter 5, another important gain is to reach very small values in x. Indeed since $Q^2 = xys$, x values down to a few times 10^{-5} in the deep inelastic regime can be accessed at HERA, two orders of magnitude smaller than previously achieved.

The kinematic variables in neutral current ep scattering are traditionally determined from the angle θ_e, and the energy, E'_e, of the scattered lepton through the relations:

$$Q^2 = 4E_eE'_e\cos^2(\frac{\theta_e}{2}), \quad y = 1 - \frac{E'_e}{E_e}\sin^2(\frac{\theta_e}{2}) \tag{2}$$

and x can then be determined as $x = Q^2/(sy)$. At HERA we adopt the convention that all polar angles are measured relative to the proton beam direction, termed forward direction in the following. The H1 and ZEUS experiments at HERA are designed to measure both the scattered electron and the hadrons produced from the struck quark and the proton remnant, thus the collision kinematics can be determined from the scattered electron, the hadrons or a mixture of both. A variable which has turned out to be particularly useful is y calculated by the Jacquet Blondel[4] method y_{JB}:

$$y_{JB} = \frac{\Sigma_h(E - P_z)_h}{2E_e} \tag{3}$$

where the sum includes all detected hadrons h, which have an energy E and longitudinal momentum component P_z. More methods to calculate the event kinematics will be discussed in chapter 5 on the measurement of the proton structure.

So far we discussed the region where Q^2 and W^2 are larger than a few GeV^2, i.e. the region where the exchanged photon is highly virtual and the hadronic invariant mass is significantly larger than the proton mass. We will start the physics discussion in these lectures however with interactions for which $Q^2 \simeq 0$ GeV^2, i.e. where the exchanged photon is almost on mass shell. These processes are usually termed (almost) real photoproduction processes. For photoproduction (γp) interactions, HERA allows to study collisions with a centre of mass energy approximately one order of magnitude larger than presently achieved in fixed target γp experiments. Due to this increase in CMS energy hard scattering in photon-proton collisions is expected to become clearly visible. This will lead to the production of jets, which can be used for detailed QCD tests and to derive information on the partonic structure of the photon. Additionally, heavy quark flavours (charm and bottom) are expected to be copiously produced in photoproduction interactions, leading to an additional field of interest at HERA.

Next, deep inelastic scattering interactions will be discussed. These will be used to explore the proton structure for the first time at x values down to $\sim 10^{-4}$, and large Q^2 values up to

5000 GeV^2. HERA enters at low x a new kinematical region where it has been speculated that new physics may be observed.[5] Further, in the study of the hadronic final state in DIS, a class of events was observed which have a large rapidity gap between the current jet and the proton remnant, and possibly result of a diffractive-like mechanism. The first electroweak results from HERA have emerged with the measurement of the charged and neutral current cross sections in the high Q^2 range. Finally, a search for exotic particles was performed. HERA is particularly suited for production of s-channel resonances from the fusion of two incoming partons (electron with a quark or gluon from the proton for leptoquarks and leptogluons respectively) or of the electron with an exchanged boson (e.g. to produce excited leptons), since the full centre of mass energy of the collision can be used to produce these states.

Before discussing the physics results, we will briefly introduce the HERA collider and the experiments. Both experiments have shown similar results on many of the physics topics discussed, but the data are mostly shown only once.

2 The HERA Collider

About 15 years ago several proposals were discussed for electron-proton colliders at DESY, CERN and Fermilab. This appeared to be the obvious possibility for extending the centre of mass energy, and hence the maximum momentum transfer squared Q^2, from $s = 2 \cdot M_p \cdot E_l \leq$ 1000 GeV^2 for the ongoing fixed target lepton-proton experiments to $s = 4 \cdot E_e \cdot E_p \leq 10^6$ GeV^2 at HERA. In July 1981 the construction of the Hadron-Elektron-Ring-Anlage (HERA) was proposed to collide 10-30 GeV electrons or positrons off 300-820 GeV protons with a luminosity above 10^{31} cm^{-2}s^{-1}. Ten years after, in October 1991, the first interactions of 12 GeV electrons and 480 GeV protons were observed at DESY. In spring 1992 the first ep collisions at 26.7 x 820 GeV were registered by the detectors. That year both experiments accumulated about 25 nb^{-1} integrated luminosity. For neutral current interactions with $Q^2 > 10$ GeV^2 the cross section is about 100 nb, thus about 2500 events are expected to be produced for the accumulated integrated luminosity. In 1993 the experiments accumulated a total of 500 nb^{-1}. For H1 about 150 nb^{-1} of the 1993 data are of limited use due to a failure of the main magnet of the detector. This year the experiments accumulated as much as 4 pb^{-1}. We still expect HERA to increase the luminosity in the next years, leading to data samples of 20-30 pb^{-1} in 1995 and 1996. Hence, HERA's physics potential is still growing each year.

HERA is an accelerator with both warm and superconducting magnets and cavities. The *proton ring* consists of 104 cells of superconducting magnets (4 dipoles, 2 quadrupoles and correction magnets, 47 m long each cell) for bend and focus. One of the straight sections contains warm cavities, a 52 MHz system accelerating bunches of 1.15 m length at an *RF* voltage of 280 kV and a 208 MHz cavity system leading to a bunch length of 0.27 m at 820 GeV proton energy. The small extension of the interaction region over a few tens of centimeters has important implications for triggering and analyzing ep interactions. The *electron ring* consists of 416 warm magnet modules (1 dipole, 1 quadrupole, 2 sextupoles and correction dipoles, 12 m long each module). Acceleration is achieved by 82 warm cavities (from PETRA) which are designed to run at about 27 GeV with 60 mA current. The HERA design energy can be reached utilizing the 16 superconducting cavities providing a gradient of about 5 MV/m which gives about 3 GeV more electron energy at the same currents. Synchrotron radiation leads to transverse electron polarization via the Sokolov-Ternov effect.[6] This is a very important feature for the HERMES experiment (see below) and for electroweak studies by the H1 and ZEUS experiments. The achieved level of polarization with 26.7 GeV electron beams at HERA is as large as 60%. Longitudinal polarization of the electrons provides more interesting physics. Spin rotators have been installed and successfully used to convert the transverse polarization to longitudinal polarization at the interaction region. During the luminosity phase operation of the machine now routinely longitudinal polarizations larger than 50% are reached.

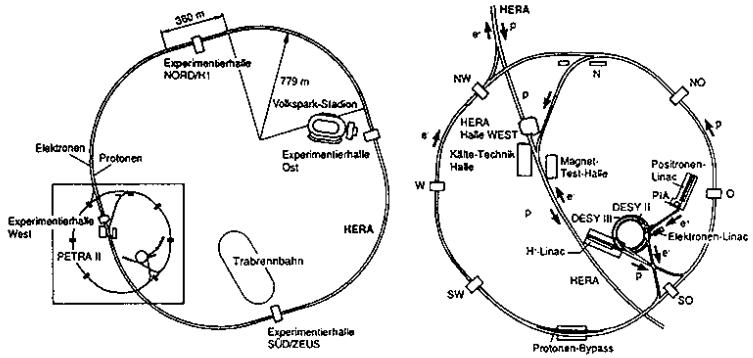

Figure 2: A schematic view of the HERA accelerator complex. The figure on the left shows the HERA ring and location of experimental halls. The figure on the right shows the pre-accelerators for protons and electrons, before injection into HERA.

In order to inject electrons and protons into the HERA ring, various pre-accelerators had to be built or/and reconstructed: three LINACs of 20, 70 and 32 m length for the acceleration of e^- (I), e^+ (II) and negative hydrogen ions (III) to energies of 220, 450 and 50 MeV, respectively. In 1986 the electron synchrotron DESY II replaced the old DESY I acting as the injector of 7 GeV electrons into the PETRA ring where the electrons are accelerated to maximum 14 GeV. A new proton synchrotron (DESY III) of 317 m diameter was constructed to reach 7.5 GeV energy prior to injection into PETRA which in turn provides 40 GeV proton injection energy. An overview of the accelerator system is given in Fig. 2.

HERA is designed to contain 210 e and p bunches. Some of those are $e(p)$ pilot bunches which pass through the detectors without being collided against $p(e)$ bunches coming the other way. These are of particular use for background and timing studies. For data taking and analysis, HERA is a very complicated environment as it combines the disadvantages of e^+e^- machines (large synchrotron radiation and electroweak cross sections) and proton rings (large backgrounds due to protons scattering from residual gas and beampipe wall). For the 1992 analysis the deep inelastic signal to beam background ratio is of the order of 10^{-4}. The bunch crossing frequency is 10.4 MHz, i.e. bunches cross every 96 ns. Table 1 compares some of the relevant characteristics for the years 1992, 1993 and 1994 with the design values.

During 1994 HERA it was realized that longer beam lifetime, and hence better effective luminosity could be reached by changing from e^-p to e^+p collisions. The electron current was found to be limited, probably because of disturbing interference due to too many remaining positive ions in the ring. Since positrons are much less sensitive to positive ions, larger currents, of about 55% of the design value could be reached. The luminosity reached accordingly about $5 \cdot 10^{30}$ cm^{-2} s^{-1}. The result of the change over is shown in Fig. 3, where around day 200 the polarity of the magnets in the electron ring and pre-accelerators was changed. After this short period one sees that the slope of the produced luminosity is much larger than for the first part of the year.

3 The H1 and ZEUS Detectors

Two experiments, H1[7] and ZEUS,[8] were ready to record ep collisions at HERA in summer 1992. Both experiments have tracker, calorimeter and muon detectors and a small angle electron tagger system. The experiments are large detectors, covering 4π solid angle apart from

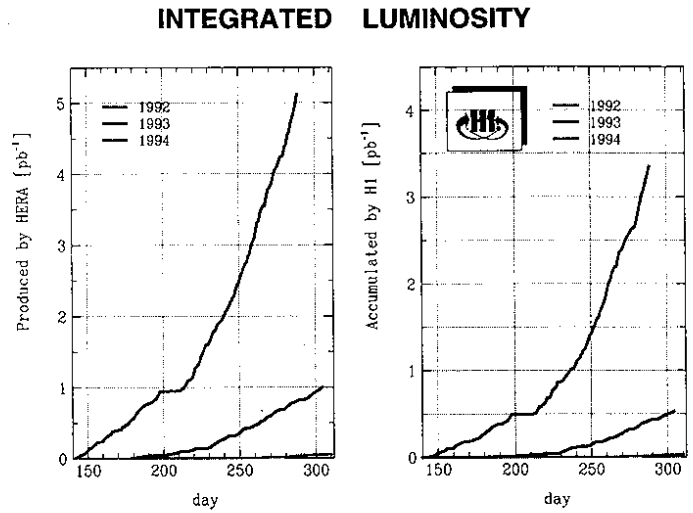

Figure 3: The integrated luminosity produced by HERA (left) and used by the experiments for physics (right) for the years 1992, 1993 and 1994. This result is for the H1 experiment; the ZEUS result is very similar.

parameter	1992	1993	1994	design value
E_p	820 GeV	820 GeV	820 GeV	820 GeV
E_e	26.7 GeV	26.7 GeV	27.5 GeV	30 GeV
nr of bunches	9	84	153	210
p current	2.0 mA	14 mA	54 mA	163 mA
e current	2.5 mA	16 mA	32 mA	58 mA
$\int_{year}$ lumi	50 nb^{-1}	1 pb^{-1}	6 pb^{-1}	50 pb^{-1}

Table 1: Comparison of some HERA parameters reached over the last 3 years of running in collider mode, with their design values. The number of bunches only counts the ep colliding bunches, the integrated luminosity is the one delivered by HERA.

losses in the beampipe. The calorimeter is an important component in the design of both detectors. The H1 collaboration has opted for liquid argon calorimetry, which is well tailored to identify and measure electrons. The large granularity of this calorimeter is exploited to compensate the intrinsically different e/π response by software weighting algorithms. In the backward region H1 has an electromagnetic calorimeter which is made of lead/scintillator stacks. ZEUS has chosen to emphasize on the quality of the hadron measurement by constructing an inherently compensating uranium-scintillator calorimeter.

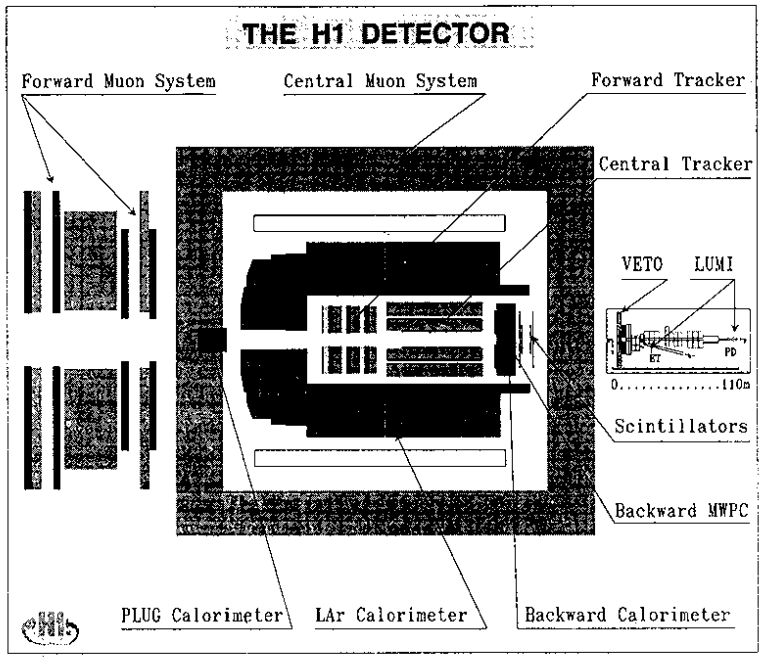

Figure 4: Schematic view of the H1 detector. Note that the luminosity detector, downstream in the electron beam is not on scale.

The H1 detector is schematically shown in Fig. 4. A detailed description of the detector and its performance is given elsewhere.[7] Charged particle tracks are measured in a central tracker (CT), forward tracker (FT) and a backward proportional chamber (BPC). The central tracker consists of two large jet drift chamber modules, two z drift chambers and two multiwire proportional chambers for triggering. Its angular acceptance is $15^0 - 165^0$. The forward tracking detector accepts tracks between 7^0 and 25^0. It consists of three modules of drift and multiwire proportional chambers. The BPC has 4 wire planes and an angular acceptance of $155^0 - 175^0$. A superconducting coil provides a uniform magnetic field of 1.15 T in the tracking region which allows the determination of charged particle momenta. The vertex position of an interaction is determined on an event by event basis from tracks reconstructed in the CT and FT, originating from the interaction region. The presently achieved resolutions for charged track parameters are $\sigma_{r\varphi} = 170$ μm and $\sigma_z = 2$ mm for the CT and $\sigma_{r\varphi} = 170$ μm and $\sigma_{xy} = 210$ μm for the FT.

The tracking detectors are surrounded by calorimeters. The liquid argon (LAr) calorimeter[9] consists of an electromagnetic section with lead absorber and a hadronic section with stainless steel absorber. The total depth of the electromagnetic part varies between 20 and 30 radiation lengths whereas the total depth of both calorimeters varies between 4.5 and 8 interaction lengths. The LAr calorimeter covers the angular range between 4° and 153°. Test beam measurements of LAr calorimeter modules have demonstrated energy resolutions

of about $0.12/\sqrt{E/\text{ GeV}} \oplus 0.01$ for electrons and about $0.5/\sqrt{E/\text{ GeV}} \oplus 0.02$ for charged pions.[7,9,10] The electromagnetic energy scale is verified to a 3% accuracy in the H1 detector by comparing the measured track momentum of electrons and positrons with the corresponding energy deposition in the calorimetric cells. The absolute scale of the hadronic energy is presently known to 5% as determined from studies of the p_T balance for deep inelastic scattering events.

The Backward Electromagnetic calorimeter (BEMC) is made of 88 lead-scintillator sandwich stacks, each with a depth of 22 radiation lengths, corresponding to about one interaction length. It covers the angular range of $155^0 < \theta_e < 176^0$. A 1.5 cm space resolution for the reconstructed centre of gravity of an electromagnetic cluster has been achieved. The energy scale of the BEMC is known to 1.7% and its resolution is described by $\sigma(E)/E = 0.1/\sqrt{E} \oplus 0.42/E \oplus 0.03$, where E is in GeV.

The calorimeters are surrounded by an iron structure, which is instrumented with streamer tubes to act as a backing calorimeter and muon filter. The forward region is equipped with a forward muon spectrometer, consisting of a toroidal magnet and drift chambers. The total angular coverage of the H1 detector for muons is $4^\circ - 171^\circ$.

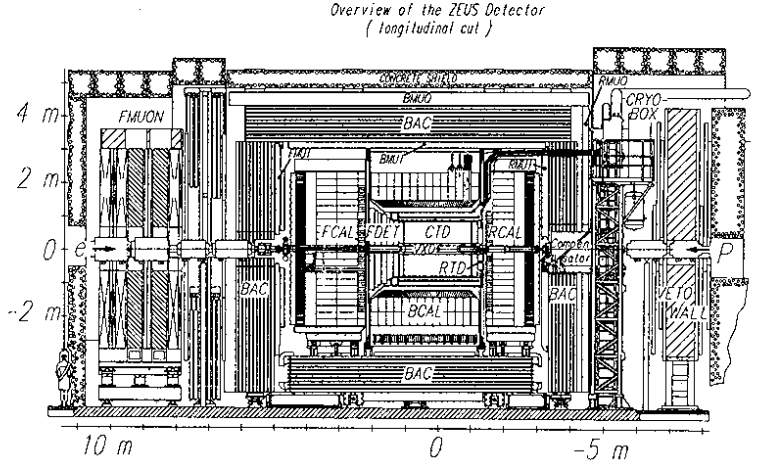

Figure 5: Schematic transverse view of the ZEUS detector. The electron and photon tagger detectors, downstream of the electron beam, are not shown.

A view of the ZEUS detector is shown in Fig. 5, together with a typical collaborator in the left down corner. Charged particles are measured by the inner tracking system consisting of a vertex detector (VXD), a central tracking detector (CTD), and a forward tracking detector (FTD). The VXD consists of 12 layers of axial sense wires. The CTD has 9 superlayers (5 axial and 4 small angle stereo), each with 8 layers of sense wires. A superconducting solenoid surrounds the inner tracking system, and produces a magnetic field of 1.43 T. Similar resolutions for charged tracks as for H1 have been achieved for the CTD.

An uranium-scintillator calorimeter (CAL) surrounds the solenoid. It is divided into a forward (FCAL), barrel (BCAL) and rear (RCAL) calorimeter. In total the calorimeter covers the full azimuthal angle and the polar angle range from 2.6^0 to 176^0. The calorimeter

is subdivided longitudinally into an electromagnetic part and two (one) hadronic parts in the FCAL, BCAL (RCAL), representing a total depth of 7 to 4 absorption lengths. The scintillator plates form 5 x 20 cm^2 (10 x 20 cm^2) cells in the electromagnetic section and 20 x 20 cm^2 cells in the hadronic sections of FCAL, BCAL (RCAL). From test beam results the electromagnetic energy resolution is $\sigma(E)/E = 0.18/\sqrt{E}$ and the hadronic energy resolution is $\sigma(E)/E = 0.35/\sqrt{E}$. Compensation has been checked up to 3%. A small tungsten-silicon calorimeter (BPC) positioned at the beampipe behind the RCAL tags electrons scattered with Q^2 down to 0.5 GeV^2

The iron yoke is instrumented with proportional tube chambers and LST chambers, and serves as a backing calorimeter and muon filter. For the identification and momentum measurement of muons, the yoke is magnetized to 1.6 T with copper coils. In the forward direction a spectrometer of two iron toroids and drift- and LST-chambers (FMUON) identifies muons and measures their momenta up to 100 - 150 GeV/c.

At HERA the luminosity is measured with the elastic bremsstrahlung reaction $ep \rightarrow ep\gamma$ which, according to the Bethe-Heitler[11] cross section formula, depends on the secondary energies E_e' and E_γ only. The experiments have installed luminosity monitor systems to measure both energies with an electron tagger for very small angle scattering at about -30 m downstream the electron beam and a photon detector at about -100 m. These detectors are electromagnetic calorimeters using TlCl/TlBr crystals for H1[12] and a Pb/SCSN38 scintillator sandwich for ZEUS.[13] The integrated luminosity measurement for the 1993 data was quoted to be accurate to 4.5 (3.5) % for H1 (ZEUS).[14,15]

Apart from H1 and ZEUS, two more experiments HERMES[16] and HERA-B,[17] have been approved for the HERA physics program. The HERMES experiment is designed to make use of the electron beam polarization at HERA. It is planned to install a polarized target (protons, deuterons and ^{3}He) to measure the proton and neutron spin dependent structure functions. Besides the scattered electron also the final state will be detected in HERMES allowing for semi-inclusive charged hadron cross section asymmetry measurements. Data taking could start as early as 1995. HERA-B is designed to make use of the high intensity of the HERA proton beam to study b-quark production and decay in fixed target pp collisions. These decays will be used to study CP violation (i.e. the subtle disregard of physics for invariance under simultaneous particle-antiparticle and left right reversal, observed so far only in the decays of neutral kaons). The pp collisions are produced by exposing thin wires in the beampipe to the halo of the proton beam. The experiment is optimized to study the channel $B^0 \rightarrow J/\psi$, with the J/ψ meson decaying into a lepton pair, which has the advantage that the theoretical predictions are particularly clean and model independent. Other channels will be studied as well. The schedule is to have a full detector available for data taking in 1998.

4 Photoproduction

In this chapter we consider interactions for which the four-momentum transfer Q^2 is small, in all cases less than a few GeV^2, and in most cases even less than 0.01 GeV^2, depending on the detection method used. Thus the virtuality of the exchanged photon is small and these interactions are called real photon collisions or *photoproduction* interactions. The scattered electron is not detected in the central detector, but for a fraction of the events the electron is detected in the small angle electron tagger of the experiments.

4.1 Introduction: Photoproduction Processes

Real photons can interact with matter *directly* through the pointlike coupling of this gauge particle with partons of the hadrons, or via the so called *hadronic* component of the photon.

Additionally the photon can split up into a quark-antiquark pair before the interaction, which does not form a bound hadronic state; this will be referred to as the *anomalous* component (see below). The hadronic component is expected to dominate the total photoproduction cross section[18] and is phenomenologically described by the Vector Dominance Model (VDM). Here the photon is pictured to couple to and fluctuate into a vector meson which has the same quantum numbers as the photon: e.g. $\rho(770), \omega(782), \phi(1020), J/\psi(3097)$. This vector meson interacts subsequently with the proton. Hence photon-hadron collisions are expected to follow largely the same phenomenology as hadron-hadron collisions. Consequently the majority of the γp are expected to be of rather soft nature, as for hadronic collisions.

In hadron-hadron scattering some fraction of the interactions exhibit hard scattering features, leading to jets with large transverse energy in the final state. These jets originate from the occasional hard scattering between constituents –quarks or gluons– from both hadrons, and are well described by QCD theory. In this hadronic picture of the γp interaction, we expect similar hard scatters to occur in photoproduction. The study of these processes is an important aspect of the HERA physics program.

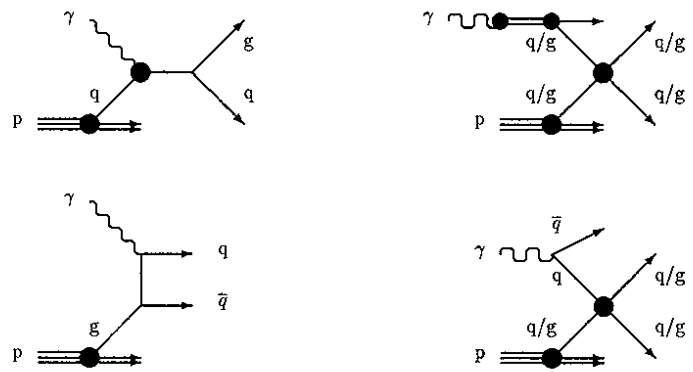

Figure 6: Hard γp processes: left part with the direct processes QCD Compton (top) and photon-gluon fusion (bottom); right part with resolved processes from the hadronic VDM component (top) and anomalous or pointlike component (bottom).

The leading order (LO) QCD diagrams leading to hard γp processes are pictured in Fig. 6. The diagrams on the left result from the direct interaction of a photon with a quark from the proton and are called *direct photon processes*. The most important direct processes are the photon-gluon fusion (PGF) and the QCD Compton (QCDC) process. The hadronic VDM component of the γp interactions contributes to hard scattering with similar diagrams as the ones in hadron-hadron interactions. Such diagrams are termed *resolved photon processes*. In fact the hadronic VDM component constitutes only part of the resolved processes. Additionally resolved processes are expected to have a contribution of the so called *anomalous component* or pointlike component, mentioned above, which results from the direct splitting of the photon in a $q\bar{q}$ pair that does not form a bound state such as a vector meson. Such diagrams are not present in hadronic collisions and are a special feature of the photon, together with the direct interactions. In case of resolved processes one can define the photon as having a structure, described by a structure function or parton densities in the photon, similar to the structure function of a hadron. These parton densities are a measure of the probability to find in the photon a parton with a certain fraction of the original photon momentum. The

analysis of hard processes in γp interactions at HERA will contribute to the exploration of the structure of the photon, as will be shown below.

The high energy interactions of real photons with matter have been studied in fixed target experiments with photon beams, and in $\gamma\gamma$ interactions at e^+e^- colliders. However, the different components of the γp interaction (direct/resolved) have not yet been unambiguously isolated by these experiments. Due to the colliding beam environment of HERA, centre of mass energies of 200 GeV can be reached for almost real γp collisions, roughly one order of magnitude larger than what has been reached so far in fixed target experiments. The large centre of mass energy should allow a clean separation of the resolved and direct components and, similar to high energy hadronic interactions, clear jet production and jet structures should become visible.

At HERA two methods are used for isolating photoproduction interactions.

- Tagged events. For this sample the small angle electron tagger is used, located at about 30 m downstream of the interaction point, to detect the scattered electron. This limits the acceptance for the virtuality of the incident photons to the range 3×10^{-8} GeV^2 $< Q^2 <$ 10^{-2} GeV^2 (4×10^{-8} GeV^2 $< Q^2 < 2 \times 10^{-2}$ GeV^2) for H1 (ZEUS). Since for this method the energy of scattered electron, E'_e, is measured, the energy of the interacting photon is simply $E_\gamma = E_e - E'_e$. The fractional energy of the photon $y \simeq E_\gamma / E_e$ (see eqn. 2) as measured by the small angle electron detector is required to be in the interval $0.25 < y < 0.7$, where the acceptance can be well controlled. This range in y corresponds to the CMS energy interval of the γp system ($W_{\gamma p}$) from 150 GeV to 250 GeV, with an average of about 200 GeV. The tagging efficiency for events in this Q^2, y region amounts to about 50%.

- Untagged events. For this sample there is no requirement on the scattered electron in the tagger. The main requirement is that no electron should be detected in the main detector, which means that Q^2 is smaller than about 4 GeV^2. The y of the photon is not measured directly but can be deduced from y_{JB} (eqn. 3) calculated from the hadrons. Analysis dependent restrictions on y are usually imposed (e.g. $0.05 < y_{JB} < 0.8$) in order to remove beam-gas background and DIS events where the scattered electron was not identified and therefore was mistakenly included in the hadronic system. Untagged event samples are roughly a factor 5 to 10 larger in statistics compared to the tagged samples.

An example of a photoproduction event, observed in the H1 detector, is shown in Fig. 7. The upper left corner shows the energy deposit of the electron in the small angle electron tagger. The central detectors show the activity of the γp hadronic final state.

In the following, we will first discuss some aspects from soft processes in γp interactions. These constitute the bulk of the collisions. Then hard scattering processes are discussed and the hadronic structure of the photon is explored. A special class of events, so called diffractive events, will be studied in terms of hard scattering in the subsequent section. Finally, the production of heavy quark flavours is considered.

4.2 Soft Processes in Photoproduction

Following the classification proposed by Storrow,[19] soft or "low-p_T" collisions are those interactions where the differential p_T cross section is well described by an exponential fall off. The dynamics of soft physics is generally regarded to be of a non-perturbative nature and not to be calculable in QCD. In hadron-hadron collisions this has been an active field of research since

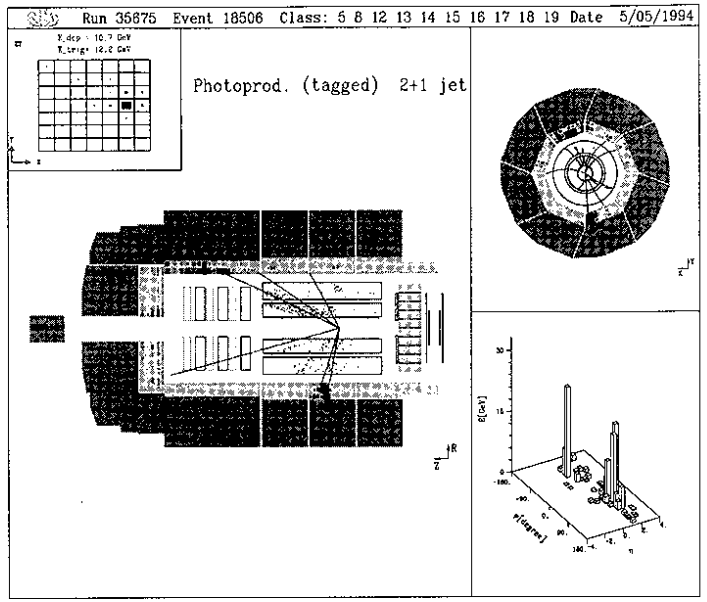

Figure 7: Photoproduction event with the electron tagged in the small angle electron tagger (upper left corner), observed in the H1 detector.

many years. Although progress has been made, details on the dynamics and possible rôle of partons in soft hadronic collisions have not yet been fully understood. It remains however one of the challenges in high energy physics to get a better insight in these processes.[20] In this section we will discuss general aspects of multi-particle production in dominantly soft collisions in γp interactions.

Fig. 8 shows the differential p_T cross section for charged particles in γp interactions at HERA, compared with measurements from proton-antiproton collisions, at a CMS energy of 200 GeV. The dominant part of the cross section shows indeed an exponential fall off, up to p_T values of 1-2 GeV/c. Thus most γp interactions are soft interactions. At larger p_T values the data behave more like a power law. This is the region we identify with hard scattering, where we can hope to use perturbative QCD to describe the scattering process, and which will be studied in detail in the next section.

Soft hadron-hadron collisions are traditionally subdivided into elastic and inelastic diffractive, and inelastic non-diffractive processes. As a result of the similarity with hadron-hadron collisions one expects a diffractive scattering component in the γp cross section. Diffractive scattering involves the exchange of energy-momentum between the incident hadrons, but no exchange of quantum numbers. Due to the interaction both or either one of the incident particles can dissociate into a multi-particle cluster. Fig. 9 shows the elastic and the inelastic diffractive process. For the latter the proton dissociates but the vector meson keeps its original identity, and is called single proton diffractive dissociation. Further processes are single vector meson diffractive dissociation and double diffractive dissociation. Diffraction is phenomenologically described by the exchange of an object called the Pomeron[21] ($\mathbb{P}$), postulated by I. Pomeranchuk. The exact nature and the very question whether this object is a particle

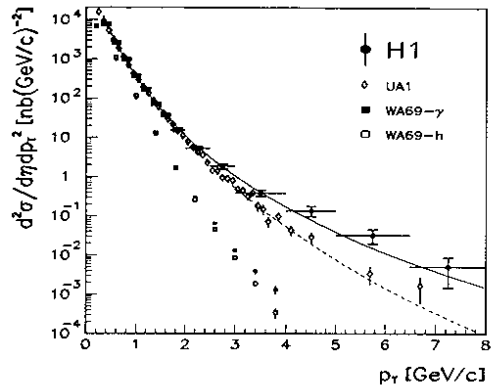

Figure 8: The inclusive ep cross section for charged particles in photoproduction (full circles) measured by the H1 experiment in the kinematical region $|\eta| < 1.5$, $Q^2 < 10^{-2}$ GeV^2 and $0.3 < y < 0.7$, at an average $W_{\gamma p} \approx 200$ GeV. Also shown are cross sections for $p\bar{p}$ collisions measured by the UA1 collaboration (open diamonds) at $W_{\gamma p} \approx 200$ GeV for $|\eta| < 2.5$, normalized to the H1 data at $p_T = 1.5$ GeV/c. The rectangles show the shape of the cross section measurements by the WA69-collaboration at $W_{\gamma p} \approx 18$ GeV, for γp (filled rectangles) and for hadron-proton data (open rectangles).

state or has any particle like properties, is far from being resolved. As it turns out HERA will be perhaps the ideal machine to study this bizarre object, which nevertheless represents a remarkably successful phenomenology.[22] In section 4.4 we will show how one can learn more about the Pomeron in γp collisions.

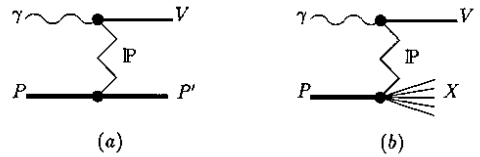

Figure 9: Examples of diffractive processes in γp: (a) elastic scattering, (b) inelastic single proton diffraction dissociation.

The total photoproduction cross section in the HERA energy region is an important measurement, due to speculations based on data from cosmic air showers.[23] These measurements have suggested, albeit with limited statistical significance, an anomalously high muon component in photon induced air showers, in the PeV energy range in the laboratory frame. This has led to predictions for the total photoproduction cross section in the HERA energy region which ranged from 100 to 700 μb.[24]

The total photoproduction cross section has been derived by ZEUS and H1 at the centre of mass energy of $\simeq$ 200 GeV, from the measured ep cross section, using the Weizsäcker-Williams approximation[26] for the photon flux. In these analyses tagged photoproduction samples have been used. The result of the total cross section measurement is shown in Fig. 10 together with the lower energy data. The measured value is $156 \pm 2(\text{stat}) \pm 18(\text{syst})$ μb at $\langle W_{\gamma p} \rangle = 200$ GeV for H1,[12] and $143 \pm 4(\text{stat}) \pm 17(\text{syst})$ μb at $\langle W_{\gamma p} \rangle = 180$ GeV for ZEUS,[27]

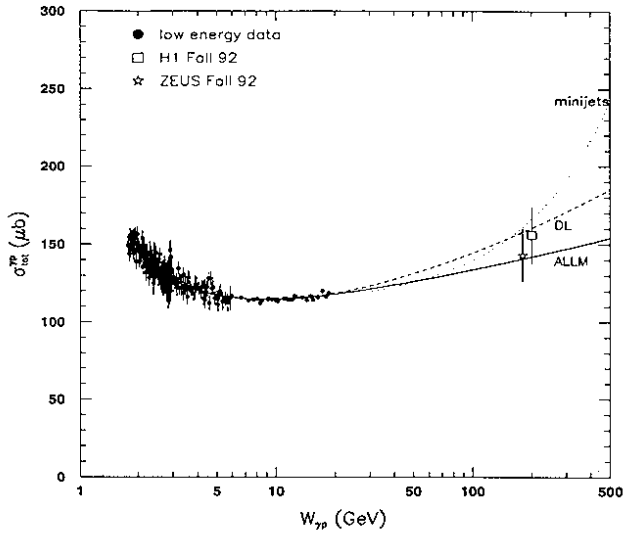

Figure 10: Energy dependence of the total γp cross section. Data from H1 (square) and ZEUS (star) are compared to model predictions from[22] (solid line) and[25] (dashed line). The dotted line is obtained with the PYTHIA Monte Carlo program using the ansatz $\sigma = \sigma^{soft} + \sigma^{jet}(s)$ for a minimum $p_T = 2$ GeV/c for the partonic collision.

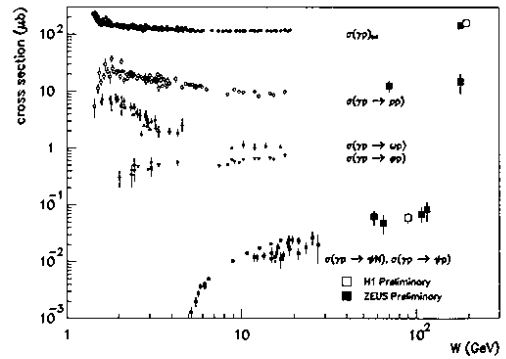

Figure 11: Photoproduction cross section measurements from HERA and lower energy experiments. The J/ψ production is discussed in section 4.5.

where $W_{\gamma p}$ denotes the CMS energy of the γp collision. The systematic error is dominated by the acceptance corrections for photoproduction events in the central detector. The total

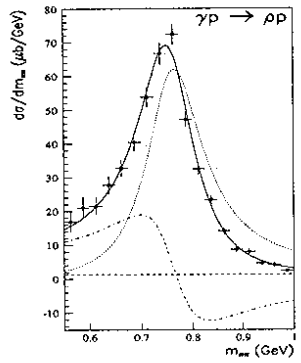

Figure 12: Distribution of the $\pi^+\pi^-$ invariant mass for elastic $\rho^0(770)$ candidates, measured with the ZEUS detector, with the curves showing the resonant (dotted line) and non-resonant (dashed line) production, and interference (dashed-dotted line) between the two.

photoproduction cross section is found to rise only weakly with the increasing centre of mass energy, as predicted by Regge inspired models.[22,25] No spectacular rise, as suggested by the photon induced air shower data, is observed!

Using tagged events global event characteristics have been used by the ZEUS collaboration to estimate the fraction of non-diffractive, inelastic and elastic diffractive components to be 64.0%, 23.3% and 12.7% respectively.[27] Assuming that 82% of the elastic cross section is due to $\rho^0(770)$ production leads to an indirect measurement of the cross section $\sigma(\gamma p \to \rho^0 p)$ of 14.8 ± 5.7 μb, and is shown in Fig. 11.

A direct measurement of the $\rho^0(770)$ elastic cross section has been made by ZEUS from the untagged γp event sample at $W_{\gamma p} \sim 50$ GeV.[28] The $\pi^+\pi^-$ mass spectrum for events with two oppositely charged tracks detected in the central tracker is shown in Fig. 12. The deviation from a Breit-Wigner shape of the $\rho^0(770)$ mass spectrum is well known and caused by the interference (dashed-dotted) of resonant (dotted) and non-resonant (dashed) $\pi^+\pi^-$ production.[29] The preliminary result for the cross section $\sigma(\gamma p \to \rho^0 p)$ is 12.5 ± 2.8 μb, and is shown in Fig. 11. Also the elastic γp cross sections show a small rise, if any, with increasing energy $W_{\gamma p}$.

H1 has further studied inclusive properties of soft hadronic collisions. Fig. 13 shows the corrected (preliminary) multiplicity distribution for a sample of tagged photoproduction events plotted in the KNO[30] variable $z = n/\langle n \rangle$, with n the multiplicity of the event. The average $W_{\gamma p}$ is about 200 GeV. The data are compared with results from $p\bar{p}$ collisions at 540 GeV in the same pseudo-rapidity region, from the UA1 experiment. The distributions look quite similar.

Particle correlations have already shown to be a useful tool to explore the dynamics of soft interactions for multi-particle data. One of the traditional investigations is correlations between identical bosons, so called Bose-Einstein (BE) correlations. The production of two identical bosons from two particle sources is governed by an amplitude which is symmetrized with respect to interchange of the bosons, resulting in an enhanced probability of emission if the bosons have similar momenta. As such, BE correlations were thought to provide information on the space-time structure of the region from which the particles originate i.e. the size

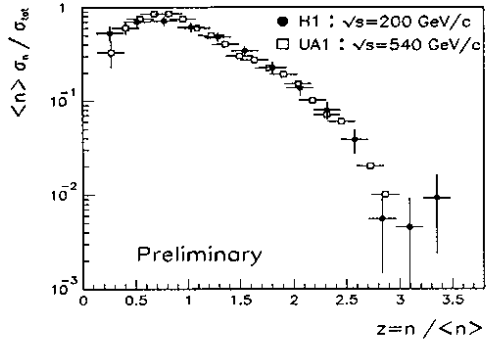

Figure 13: The γp multiplicity distribution for charged particles in the kinematical region $|\eta| < 1.5$, $Q^2 < 10^{-2}$ GeV^2 and $0.3 < y < 0.7$, at an average $W_{\gamma p} \simeq 200$ GeV (full circles), measured by the H1 experiment. The data are compared with results from $p\bar{p}$ interactions (open rectangles), and presented in KNO form.

of the particle emitting source, and on "freeze-out" properties of hadronization. Recent ideas however[31] tend to relate the strength of the BE effect observed in data to effects such as the string tension, rather than the particle emission volume.

H1 has presented preliminary results on BE correlations, based on tracks reconstructed in the central tracker, with a $p_T > 250$ MeV/c and $|\eta| < 1.5$ GeV, for tagged γp interactions. The charged particles were identified as pions, using dE/dx information. Figure 14 shows the ratio $R(Q^2_{BE}) = N(Q^2_{BE}(\pi^-\pi^-))/N(Q^2_{BE}(\pi^+\pi^-))$ of the Q^2_{BE} distributions for like-sign and unlike-sign pion pairs, where here Q^2_{BE} is defined as the (minus) square of the four-momentum difference between the two bosons: $Q^2_{BE} = -(q_1 - q_2)^2$. The unlike-sign pion pair sample does not exhibit a BE effect and is used as a reference. This sample however contains correlations resulting from particle decays ($K^0, \rho^0(770)$), in regions indicated in the figure. The $R(Q^2_{BE})$ distribution is shown for both data and Monte Carlo (which does not include the BE effect). A clear BE enhancement in like-sign pairs is observed for $Q^2_{BE} < 0.1$ GeV^2 in the data. A fit of the form $R(Q^2_{BE}) = 1 + \lambda \exp(-\beta Q^2_{BE})$ yields a radius $r_{BE} = 0.197\sqrt{\beta} = 1.04 \pm 0.04 \pm 0.1$ fm, $\lambda = 0.54 \pm 0.04 \pm 0.07$. The $\rho^0(770)$ and K^0 regions have been excluded for the fit. This parametrization corresponds to the assumption of a Gaussian shape of the source in the centre of mass of the pion pair. Here λ is the correlation strength and the radius r_{BE} a measure for the spatial dimension of the pion source. A comparison for different processes is shown in Fig. 14. The meson-proton data can be considered as reference for this γp measurement. Comparing with the (highest available energy) meson-proton data, recorded at ~ 10 times smaller CMS energy, does not reveal any significant energy dependence of r_{BE} or λ.

In all, soft γp interactions show a multi-particle production and cross section behaviour similar to hadron-hadron collisions. HERA can in this sense be considered as a "meson-proton" collider, and the γp data can be used to study soft hadronic collisions at a center of mass energy of 200 GeV.

4.3 Hard Processes in Photoproduction

Hard scattering in γp interactions is expected from partonic collisions between quarks and gluons of the incident proton and the resolved photon, and from the direct production diagrams

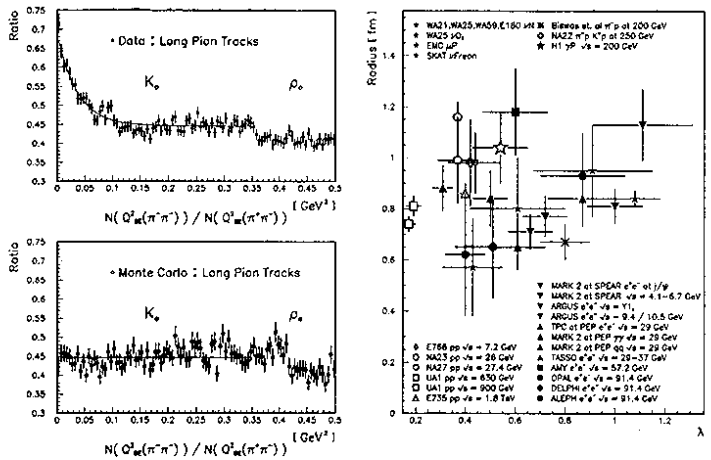

Figure 14: Preliminary distributions of Bose-Einstein correlations from H1: (left) the ratio $R(Q^2_{BE}) = N(Q^2_{BE}(\pi^-\pi^-))/N(Q^2_{BE}(\pi^+\pi^-))$ for data (top) and Monte Carlo (bottom); (right) a compilation of the radius and correlation strength (λ) values for different experiments, including the H1 result.

(photon-gluon fusion and QCD Compton scattering) as depicted in Fig. 6. In this section we will address the questions: do we have evidence for hard scattering in γp interactions, and, if yes, do we find any evidence for both the resolved and direct γp production? For resolved collisions this picture leads to the introduction of a "photon structure function", describing the probability for finding partons in the photon which carry a momentum fraction x_γ of the photon. One of the challenges at HERA is to measure the x_γ distribution in the photon: to measure the photon structure.

A high p_T tail, characteristic for a hard scattering process, is expected to be observed in the inclusive p_T spectrum of charged particles. Indeed, from Fig. 8 the presence of such a large p_T tail is evident. If hard parton scattering dynamics is the cause of this high p_T part of the data, we can compare it with QCD calculations. This is shown in Fig. 15, where the high p_T part is compared with a next to leading order (NLO) calculation[32] including resolved and direct processes. The agreement between the data and the calculation is very good. It also shows that indeed the resolved processes dominate at the lower p_T end of the distribution, but constitute only about 70% of the cross section at large p_T values, the remaining part are direct processes. Fig. 8 also displays the $p\bar{p}$ data at $\sqrt{s} = 200$ GeV. The high p_T tail in γp interactions is clearly larger. The effect due to the different structure function for the proton and photon (when taken to have the same parton distributions as a meson) cannot explain fully the discrepancy observed for the high p_T part of the differential cross section.[33] Hence extra non-VDM contributions are needed to explain the γp cross section, such as the direct and the anomalous component. Note that the later is often taken to be part of the photon structure function.

The next step towards establishing hard scattering in γp interactions is the observation of jets. In fact, the event shown in Fig. 7 shows clear jet structures, visible in the different detector views and from the energy flow in the $\eta - \varphi$ plot. Events such as this one were found soon after the startup of HERA, in the late spring of 1992. To be more quantitative

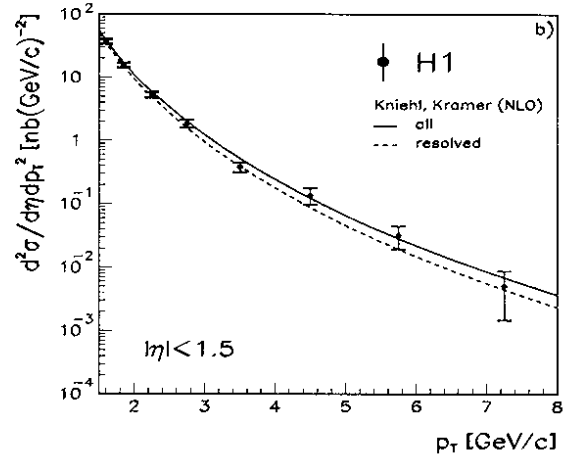

Figure 15: The measured single particle cross section of H1 from Fig. 8 (full circles), compared in the region $p_T > 1.5$ GeV/c with an analytical NLO QCD calculation.[32] The solid line represents the sum of the resolved (dashed line) and direct photon contributions.

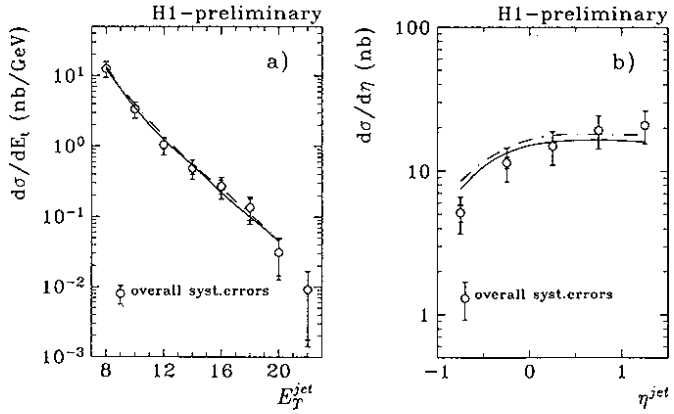

Figure 16: Preliminary H1 data showing: (a) the inclusive differential ep cross section $d\sigma/dE_T^{jet}$ integrated in the pseudo-rapidity interval $-1.0 < \eta^{jet} < 1.5$; (b) inclusive ep cross section $d\sigma/d\eta^{jet}$ for jets with $E_T^{jet} > 7$ GeV. The inner error bars represent statistical errors, the outer error bars the statistical and systematic errors added in quadrature. The overall systematic uncertainty is shown separately. The measurement is compared to PYTHIA predictions using the GRV-LO[34] (full line) and LAC2[35] (dashed-dotted line) parton distributions for the photon.

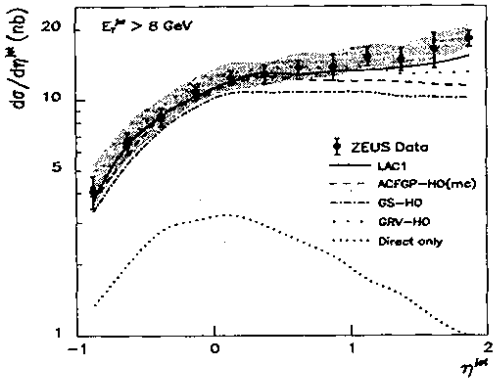

Figure 17: Measured differential ep cross section $d\sigma/d\eta^{jet}$ of the ZEUS experiment for inclusive jet production integrated over $E_T^{jet} > 8$ GeV, for $Q^2 < 4$ GeV^2 and $0.2 < y < 0.85$. The shaded band displays the uncertainty due to the energy scale of the jets. The data are compared with LO QCD calculations using PYTHIA, for different parton distributions in the photon.

a jet algorithm is used. For the H1 analysis presented in Fig. 16 jets within the range $-1 < \eta^{jet} < 1.5$ are selected using a cone algorithm,[36] requiring $E_T^{jet} > 7$ GeV in a cone with radius $R = \sqrt{\Delta\eta^2 + \Delta\varphi^2} = 1.0$ in the space of pseudo-rapidity η and azimuthal angle φ (in radians). In Fig. 16a the ep jet cross section, corrected for detector smearing to the cross section at the level of the final state hadrons (the hadron level), is shown as function of E_T^{jet}. A sample of tagged events is used for this analysis. The data follow an $E_T^{-5.6}$ dependence. The η dependence of the jet cross section is shown in Fig. 16b. The figures also show a LO QCD prediction calculated using the PYTHIA[37] Monte Carlo program for hard photon-hadron processes, using different assumptions for the parton density distributions – or structure – of the photon. These parton density distributions describe the results from $\gamma\gamma$ interactions from e^+e^- experiments. PYTHIA includes both direct and resolved processes. The QCD predictions describe the data quite well for the selected parton density parametrizations. In Fig. 17 the differential jet cross section from ZEUS is shown for jets with $E_T^{jet} > 8$ GeV.[38] The data show the same level of agreement with the LO QCD calculations.

A quantity of particular interest is the momentum fraction, x_γ, of the parton in the photon involved in the hard scattering. For direct processes $x_\gamma = 1$, since the full momentum of the photon enters the hard scattering, while for resolved processes $x_\gamma < 1$. The measurement of the distribution of x_γ is analogous to the measurement of Bjorken-x in deep inelastic scattering (see next chapter) and is a direct measure of the hadronic structure of the photon. The jet kinematics can be used to determine x_γ of the parton involved in the hard scattering collision. Indeed, for a LO QCD $2 \to 2$ scattering process x_γ can be approximately reconstructed as follows:

$$x_\gamma = \frac{E_T^{jet1} e^{-\eta^{jet1}} + E_T^{jet2} e^{-\eta^{jet2}}}{2E_\gamma}, \qquad (4)$$

where the indices refer to the two jets resulting from the two partons involved in the hard scattering (see Fig. 6).

First, we will establish the presence of a direct component in the γp cross section from 2-jet event studies. In an analysis performed by the ZEUS collaboration[39] events with at least two jets have been selected using a cone algorithm on a grid in pseudo-rapidity η and azimuthal angle φ with cone radius $R = 1$. Jets are required to have $E_T^{jet} > 6$ GeV and to be in the

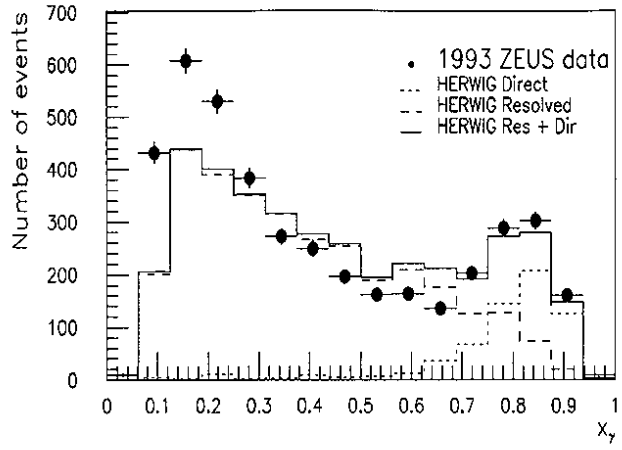

Figure 18: Reconstructed x_γ distribution for ZEUS (full circles). The histograms represent the prediction of the LO QCD calculation from HERWIG for the direct component (dotted line), the resolved component (dashed line) and the sum of these two contributions (full curve).

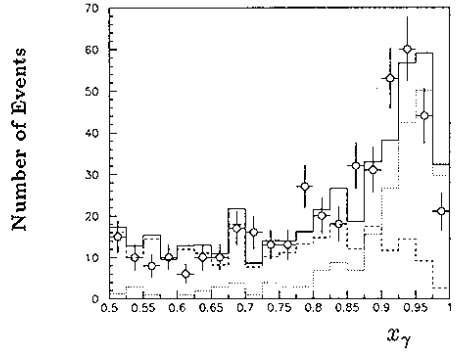

Figure 19: Preliminary reconstructed x_γ distribution for H1 (open circles). The histograms represent the prediction of the LO QCD calculation from PYTHIA, with full detector simulation, for the direct component (dotted line), the resolved component (dashed line) and the sum of these two contributions (full curve).

pseudo-rapidity interval $-1.125 < \eta^{jet} < 1.875$. For this analysis untagged γp interactions were used. The photon energy E_γ is given by $E_\gamma = yE_e$ and the y is reconstructed from the hadronic energy flow measured with the calorimeter using eqn. 3. The reconstructed x_γ spectrum is shown in Fig. 18. The curves in Fig. 18 are leading order QCD calculations,

this time using the HERWIG[40] Monte Carlo program for hard γp processes. The calculations include a full detector simulation and assume the LAC1 parametrization[35] for the parton distributions of the photon. The Monte Carlo predictions are also shown separately for the direct and the resolved component. In the high x_γ region ($x_\gamma > 0.6$) the data are well described by the sum of the two contributions: the resolved component alone is not able to reproduce the "peak" at $x_\gamma \approx 0.8$. Note that the measurement of x_γ in direct process extends to values smaller than 1, due to the experimental resolution. In the region of $x_\gamma < 0.5$ the direct contribution is negligible and the events observed in the data sample can only be explained by resolved photon processes. The prediction for this region depends critically on the assumed parton distributions for the photon, and will be explored below. Fig. 19 shows the x_γ distribution at high x_γ for untagged events, as measured by the H1 collaboration. Here jets with an $E_T^{jet} > 8$ GeV and $-1 < \eta^{jet} < 3$ have been used. The distance in η between the jets was required to be less than 1.5. The results are compared with predictions from the PYTHIA Monte Carlo program using the GRV parton distributions for the photon and proton. Again, the data can only be explained if a direct component is included in the data. In all, the x_γ distribution shows that both classes of processes, direct and resolved, shown in Fig. 6, are present in the data.

From Figs.15 and 18 it is clear that the bulk of hard scattering photoproduction events at HERA is due to resolved processes. In a resolved process only a part of the original photon momentum enters the hard subprocess and the rest is carried by other –spectator– partons, as is shown in Fig. 6. These spectator partons fragment into a photon remnant, similar to the proton remnant introduced earlier, and which is expected to appear in the detector close to the original photon direction. A study of this photon remnant was performed by the ZEUS collaboration. A clustering algorithm, called k_T algorithm[41] was used for the jet search. With this algorithm all calorimeter cells are grouped in three clusters, excluding the proton remnant (most of which disappears in the beampipe anyway). The clusters are ordered according to their p_T and the following cuts are applied for event selection: $p_T^{cluster1,2} > 5$ GeV, $\eta^{cluster1,2} < 1.6$ and $\eta^{cluster3} < -1$. Monte Carlo studies show that the selected sample is dominated by resolved photoproduction. The third cluster is associated with the photon remnant. Fig. 20 shows the average total transverse and longitudinal energy of this third cluster with respect to the cluster axis, as a function of the cluster energy. The data are compared with predictions from a Monte Carlo calculation (based on the PYTHIA generator and including a full detector simulation) in which the fragmentation of the remnant is treated the same way as the hard jets. The good agreement between data and Monte Carlo predictions demonstrates the jet-like properties of the photon remnant.

Finally, hard scattering events in photoproduction data will be used to retrieve information on the "partonic structure" of the photon. The quark content of the photon has been measured in $\gamma\gamma$ interactions in e^+e^- experiments, down to $x_\gamma \geq 0.007$.[42] For these measurements a highly virtual photon is used to probe a real photon. As for an ordinary hadron the real photon is expected to have a gluon content as well but, since a virtual photon does not couple directly to gluons, the gluon content is not directly accessible in these measurements. Some sensitivity to the gluon in the photon was shown in data from e^+e^- experiments by studying $\gamma\gamma$ interactions where both photons are essentially on mass shell.[43] Hence to date only poor constraints on the gluon density in the photon exist. Furthermore there is no momentum sum rule for the photon and therefore the present predictions for the gluon distribution from different parton parametrizations of the photon differ wildly.

At HERA a parton from the proton rather than a virtual photon is used to probe the photon structure. These partons evidently interact with both the quarks and the gluons in the photon, allowing for the first time to measure the gluon content of the photon. The price one has to pay is that at HERA one measures in this way always the sum of the quark and gluon component of the photon. Therefore, to isolate the gluon part one has to subtract the part induced by the quarks, using e.g. the measurements from e^+e^- experiments.

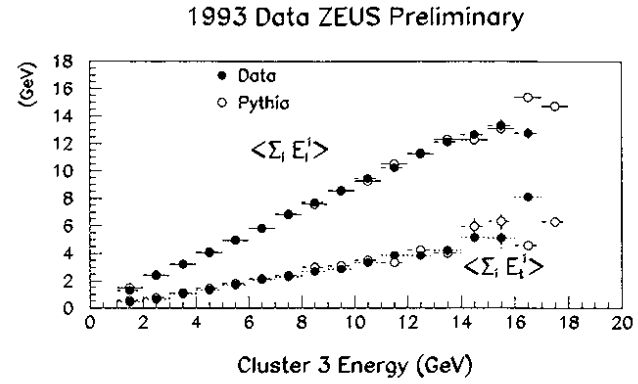

Figure 20: Average transverse $\langle \sum_i E_t^i \rangle$ and longitudinal $\langle \sum_i E_l^i \rangle$ energy as a function of the third cluster energy. The sum runs over all hadrons belonging to the cluster. The preliminary ZEUS data (full circles) are compared with Monte Carlo prediction (open circles).

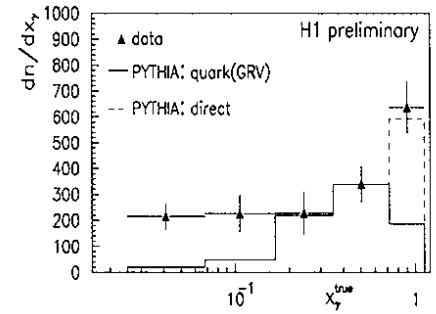

Figure 21: The distribution of the corrected parton momentum x_γ. The preliminary H1 data (full triangles) are compared to the PYTHIA prediction of the direct component (dashed line) and the quark part of the resolved contribution (full line) using the GRV-LO parametrization. Only statistical errors are shown.

A first attempt to measure the gluon in the photon was made by H1, using jets with a minimum transverse energy $E_T^{jet} > 7$ GeV in the pseudo-rapidity interval $-0.2 < \eta^{jet} < 2.5$, which give access to the partons in the range $0.03 < x_\gamma < 1$. A sample of tagged events is used so that the photon energy E_γ was given by the difference between the beam and the tagged electron energies. A problem encountered during this analysis is that the hard scattering Monte Carlo programs, like PYTHIA, give a poor description of the energy flow at large pseudo-rapidities. The data show a much higher pedestal energy between the jets compared to the predictions of these Monte Carlo generators. Allowing for events with multiple scattering, i.e. apart from the principally interacting partons additional partons from the proton and photon remnant can interact, the description of the energy flows can be substantially improved. In this study we take the multiple interaction scheme to be the physics process to describe the

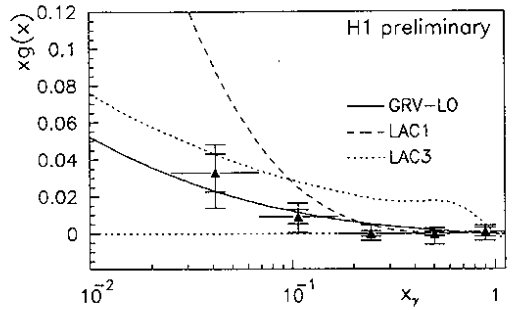

Figure 22: The gluon density in the photon (triangles), as measured by the H1 experiment compared with the GRV-LO (full), the LAC1 (dashed) and the LAC3 (dotted) distributions at the average scale of 60 GeV^2. The data are preliminary.

excess of energy flow between the jets and consequently assume that the pedestal energy seen between also affects the jet energy measurement and has to be subtracted. Next, an unfolding procedure[44] is used to convert the observed x_γ distribution into the "true" x_γ distribution, shown in Fig. 21. The correlations between observed x_γ and true x_γ are taken from the PYTHIA Monte Carlo program, introducing unavoidably a certain model dependence in the result. The data are compared to the LO QCD prediction, calculated with PYTHIA and normalized to the integrated luminosity, for the direct component and the quark part of the resolved photon contribution. These calculations use the GRV-LO parametrization[34] of the photon parton densities. The sum of the two components gives a good description of the data for $x_\gamma > 0.2$. The excess of events over the quark part of the resolved contribution in the region $x_\gamma < 0.2$ can be attributed to the gluon content of the photon.

After subtraction of the predicted direct contribution and the quark part of the resolved component predicted from e^+e^- data, the gluon density in the photon can be extracted. The result is shown in Fig. 22 where the gluon density $x_\gamma g(x_\gamma)$ at an effective scale ≈ 60 GeV^2 is given. It is important to note that this result was achieved in the framework of a leading order interpretation of the data. The inner error bars in Fig. 22 represent the statistical and the outer error bars the statistical and systematic errors added in quadrature. The dominating systematic errors are the uncertainty on the hadronic energy scale and the correction for the imperfect description of the energy flow by the Monte Carlo generator. The gluon content in the photon is restricted to small x_γ values as expected. Despite the large error bars the data already constrain the parton distributions in the photon and discriminate between different parametrizations. The measurement presented in Fig. 22 is compared to the LAC1, LAC3 and GRV-LO parametrizations of the photon parton distributions. The LAC3 distribution assumes a large gluon component at high x_γ. This scenario is clearly disfavoured by the data. The dashed curve shows the prediction for LAC1 assuming a very large gluon component at small x_γ. The GRV parton density parametrization gives the best description of the data

In summary, hard scattering and jets have been unambiguously observed in γp interactions at HERA. We have established the presence of both direct and resolved processes. The jet inclusive cross sections behave as expected from (LO) QCD. The 2-jet events give access to the parton distributions in the photon. For the first time a (LO) gluon extraction was performed relying on the validity of the PYTHIA model for the description of γp hard scattering interactions.

4.4 Hard Scattering in Diffractive Processes

In section 4.2 it was discussed that between 30% and 40% of the γp interactions are diffractive events. From the experimental and phenomenological point of view these events exhibit gaps in rapidity which are not exponentially suppressed.[45] Such a gap results from the absence of colour flow between the systems connected by the exchanged Pomeron as is shown in the examples given in Fig. 9.

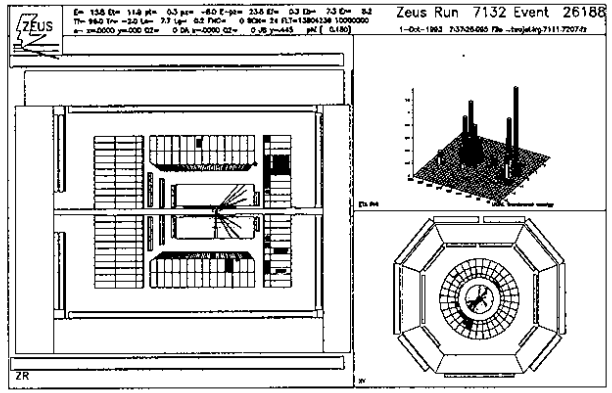

Figure 23: Display of a ZEUS photoproduction event with a large rapidity gap in the forward direction.

The technique used so far by both experiments to isolate events with rapidity gaps at HERA is based on the variable η_{max}. The η_{max} of an event is defined as the largest measured value of pseudo-rapidity for which activity is detected. The maximum value which can be reached is determined by the acceptance of the detector. Both experiments have used the main calorimeter for their initial studies, leading to maximum reachable values in the laboratory system of η_{max} of 4.3 for ZEUS and 3.7 for H1. Here η_{max} of an event is defined to be the largest η for which a cluster or condensate with energy larger than 400 MeV is found. Small values of η_{max} indicate that there is a large region between η_{max} and the detector edge with no activity in the detector. A measured η_{max} value equal to 0 means for the ZEUS detector that there is an empty gap of 4.3 units in rapidity in the forward direction. Such an event (with $\eta_{max} \approx 0$) is shown in Fig. 23.

The distribution of η_{max} for a sample of tagged photoproduction events is shown in Fig. 24 for H1 data. For small η_{max} values, i.e. for large gaps, the data clearly do not show an exponential decrease, and hint towards diffraction as the underlying dynamic process. The data are compared with predictions of a diffractive model (**sd**) and a model which does not contain diffractive events (**nd**). Clearly, the non-diffractive model describes well the values at large η_{max}, but fails completely in the region where the gap gets large. The diffractive model on the other hand gives a rather good description of the region $\eta_{max} < 2$. Hence diffractive production is a plausible interpretation for the events with a large rapidity gap in γp interactions.

Phenomenologically, the observed properties of the diffractive cross section in the framework of Pomeron exchange are described by triple-Regge theory.[46] This interpretation however gives no information on the details of the hadronic final states produced in diffractive

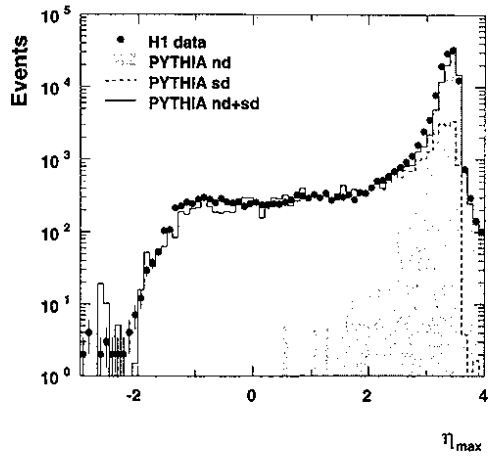

Figure 24: Maximum peudo-rapidity η_{max} distribution in γp events observed in the H1 detector, compared to a diffractive (dashed line) and a non-diffractive (shaded area) Monte Carlo model, and their sum (full line).

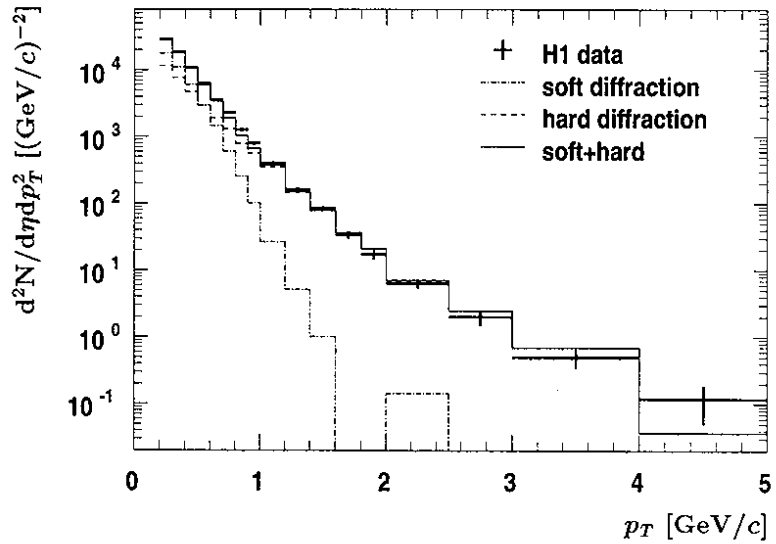

Figure 25: Transverse momentum distribution of charged particles for events with a large pseudo-rapidity gap (η_{max} <1.5), measured by the H1 experiment, compared to Monte Carlo predictions explained in the text.

events. Traditionally the final state in diffractive dissociation is assumed to be described by a multiperipheral[47] type of model in which particles are distributed throughout the final state

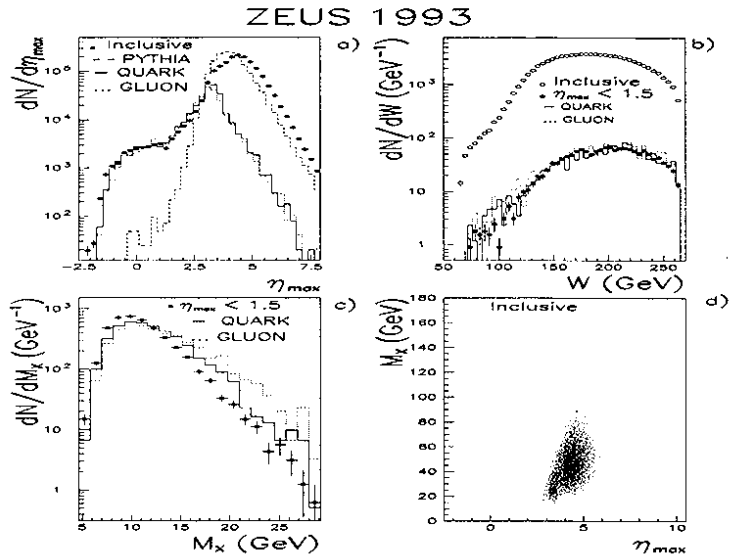

Figure 26: (a) The distribution of η_{max}, the pseudo-rapidity of the most forward calorimeter condensate with an energy above 400 MeV for the ZEUS photoproduction sample with $E_T > 5$ GeV along with the predictions from a non-diffractive model (dashed line) and model for diffractive hard scattering, with a quarkonic (solid line) or gluonic (dotted line) Pomeron of type $G0$. (b) The distribution in W for all events and for those with $\eta_{max} \leq 1.5$. (c) The mass of the visible hadronic system M_X for events with a large rapidity gap as defined by $\eta_{max} \leq 1.5$ along with model predictions. (d) A scatter plot of the mass of the visible hadronic system, M_X, versus η_{max}.

phase space with limited transverse momentum. This approach has been used successfully so far for comparisons with the available measurements of multiplicity and rapidity distributions of charged particles from the diffractive system. On the other hand, in modern QCD language it is tempting to consider the Pomeron as a partonic system[48] which can be probed in a hard scattering process. Models based on this idea assume that the Pomeron behaves as a hadron and the concept of a Pomeron structure function is introduced.[49–51] In contrast to the approach of assuming limited p_T phase space, these models predict that, similar to high energy hadron-hadron scattering, high mass diffractive dissociation exhibits the production of jets and a large p_T tail in the differential transverse momentum distribution. Thus hard hadron-Pomeron scattering events should be observed in diffractive hadronic collisions at high energies. The UA8 collaboration has shown evidence for jet production in diffractive $p\bar{p}$ events,[52] interpreted as resulting from collisions of partons from the proton with partons from the Pomeron. Furthermore, within this partonic picture, these data have shown sensitivity to the parton distribution in the Pomeron. On the latter relatively little information is known. Scenarios exist in which the Pomeron is pictured to consist either dominantly of quarks or gluons. For the distribution functions of the partons one assumes either a "hard" distribution, $\beta g(\beta) \sim \beta(1-\beta)$, (hereafter labeled "$G0$"), or a "soft" distribution, $\beta g(\beta) \sim (1-\beta)^5$, (hereafter labeled "$G5$"). The variable $\beta = x_{i/p}$ is the fraction of the Pomeron momentum carried by the struck parton i involved in the interaction. The results from high p_T jet production in diffractive proton-antiproton interactions mentioned above favour the hard $G0$ distribution.

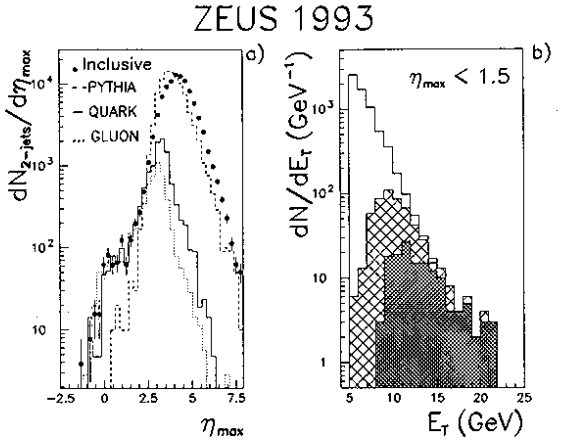

Figure 27: (a) The distribution of η_{max} for the ZEUS photoproduction sample with $E_T > 5$ GeV and two or more jets along with the prediction from a non-diffractive model (dashed line) and a diffractive model, with a quarkonic (solid line) and gluonic (dotted line) Pomeron of type $G0$. (b) The distribution of the total observed transverse energy E_T for the photoproduction event sample with a large rapidity gap ($\eta_{max} \leq 1.5$) and, in addition, for the subsample of those events with at least one (cross hatched area) and at least two (shaded area) jets in the final state.

In the present studies, the agreement with the partonic collision picture is tested with the aid of Monte Carlo programs. For this study we use a model which explicitly includes diffractive hard scattering: POMPYT1.0.[53] This model assumes the emission of a Pomeron at the proton vertex. The resulting photon-Pomeron interaction is simulated as the hard scattering of the photon (direct process) or partons in the photon (resolved process) with partons in the Pomeron according to LO QCD calculation for the hard scattering processes.

We show results from H1[54] and ZEUS[55] on the observation of hard processes in γp diffractive events. In Fig. 25 the transverse momentum distribution is shown for charged particles from events with a large rapidity gap ($\eta_{max} < 1.5$). The presence of a clear large p_T tail - similar to the one for all γp events as shown in Fig. 8 - is clearly visible. The data are compared to predictions of models with (hard diffraction; POMPYT) and without (soft diffraction) hard partonic scattering. It shows that the predicted shape of the first model is consistent with the data at large p_T values, while the model without diffractive hard scattering does not describe the data.

Next events are preselected which have a total E_T larger than 5 GeV. ZEUS data[55] for η_{max}, W and M_X are shown in Fig. 26. Here W is the total hadronic invariant mass of the event, M_X is the visible hadronic invariant mass of the system for all hadrons with $\eta < \eta_{max}$, i.e. the diffractive dissociated system. The POMPYT model predictions were calculated with the $G0$ parton distributions for the Pomeron, assuming either the quark and gluon hypothesis for the Pomeron structure. In Fig. 26a a clear shoulder is seen at small η_{max} indicating the presence of rapidity gap events in this large E_T sample. Values of $\eta_{max} > 4.3$, which are outside the acceptance of the calorimeter, occur when energy is deposited in many contiguous cells around the beampipe in the forward direction. It is interesting to note that at large W the data show a rather constant or slowly rising behaviour (Fig. 26b) consistent with the interpretation that the rapidity gap data are predominantly resulting from Pomeron exchange.

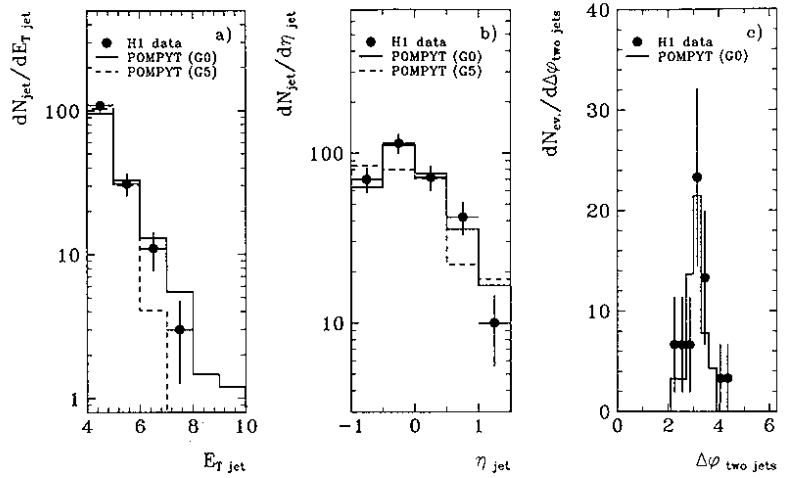

Figure 28: (a,b) Inclusive jet distributions for large pseudo-rapidity gap events (η_{max} <1.5) measured with the H1 detector: transverse energy E_T^{jet} and pseudo-rapidity η^{jet}. (c) Distribution of the azimuthal angle $\Delta\varphi$ between the jets for 2 jet events. The data are compared with Monte Carlo predictions assuming a Pomeron with hard ($G0$; full line) and soft ($G5$; dashed line) gluon momentum distribution.

The deviations close to the maximum W and at W below 150 GeV result from acceptance effects. Fig. 26c shows that the distribution of the visible hadronic mass dN/dM_X falls steeply with increasing M_X as expected for diffractive phenomena. In this high E_T sample jets we search for jets which have an $E_T^{jet} > 4$ GeV within a cone of radius equal 1. The sample is found to consist of 91.4% zero-, 6.5% one-, 2.0% two and 0.1% three or more-jet events. The η_{max} distribution for events with at least 2 jets and event E_T distribution are shown in Fig. 27. At large E_T the sample predominately consist of 2-jet events. The 2-jet event sample will allow us to study the Pomeron structure with future high statistics data. The parton densities in the photon will be measured at HERA and then used in jet analyses of diffractive events to unfold the parton densities of the Pomeron using the same technique as discussed in section 4.3. Characteristics of the jets are shown in Fig. 28. The model for diffractive hard scattering describes the data well. In particular the back-to-back behaviour of the jets for events where two jets were detected is clearly seen.

To restrict to a region where the data show dominantly hard scattering features, a comparison is made of the H1 data with the POMPYT model by increasing the minimum E_T requirement for the events to 9 GeV. The 1 and 2-jet event fractions are then 38.7% and 13.4% respectively, and the ratio (2 jets)/(1 jets) is 0.35 ± 0.09. These results are compared with POMPYT predictions in Table 2, assuming the Pomeron consists predominately of gluons. The (2 jets)/(1 jets) ratio, which is only weakly sensitive to the remaining soft diffractive contribution, compares favourably with the prediction of a hard Pomeron parton distribution. It depends however somewhat on the divergence limit ($\hat{p}_T^{min}$) used in the LO QCD matrix element calculation for the hard partonic scattering process.

In summary, we have observed hard processes in photoproduction with a large rapidity gap at HERA. Interpreted in terms of diffractive scattering, the results are sensitive to the parton distributions in the Pomeron (hard/soft; quark/gluon), where in general a harder

Sample	1 jet events(%)	2 jet (%)	2-jet/1-jet
Data (142 events)	38.7	13.4	0.35 ± 0.09
POMPYT $G0$ ($\hat{p}_T^{min}$ = 2 GeV)	46.4	10.1	0.22 ± 0.05
POMPYT $G5$ ($\hat{p}_T^{min}$ = 2 GeV)	27.3	-	< 0.1

Table 2: Jet rates: H1 data compared to POMPYT Monte Carlo calculations for γp events with $E_T > 9$ GeV and $\eta_{max} < 1.5$, and for jets with $E_T^{jet} > 4$ GeV and $-1 < \eta^{jet} < 1.5$.

type of parton distribution is prefered. Future precise data will allow to extract the parton distributions of the Pomeron.

4.5 Heavy Flavour Production

An important aspect of photoproduction studies at HERA is the production of heavy flavours, in particular charm quarks. Apart from properties of charmed mesons and baryons, heavy flavour studies in photoproduction are expected to give information on the gluon density in the proton and on the dynamics of strong interaction physics in kinematical regions in which the physics descriptions range from non-perturbative phenomenological approaches to perturbative QCD.

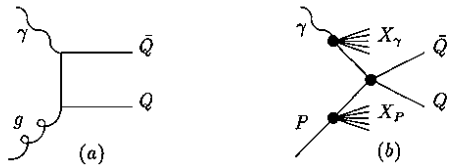

Figure 29: Mechanisms for heavy quark photoproduction: (**a**) direct photoproduction process, (**b**) resolved photoproduction process.

The luminosity collected by the experiments so far allows us to study (a) J/ψ production, particularly in the elastic channel, (b) the total charm production cross section from semi-leptonic decays and (c) the production of D^* mesons. Photoproduction LO QCD processes leading to inelastic production of heavy flavours are shown in Fig. 29a for direct and Fig. 29b for resolved production. The production of J/ψ mesons is in this context described by the colour singlet model,[58,57] where the $Q\overline{Q}$ pair can end up in a bound state via the emission of a gluon, which connects with the proton remnant. The photon-gluon fusion process (Fig. 29a) shows that these events give direct information on the gluon density in the proton, since the gluon enters at the Born level for this diagram. Measuring the cross section of these events will be one of the experimental handles at HERA to extract the gluon content of the proton, which will be elaborated on in the chapter on deep inelastic scattering. Elastic production of J/ψ mesons can in this QCD prescription be described by the exchange of 2 gluons.[59] On the other hand, for interactions with a small p_T vector meson dominance contributions are expected, as discussed in in section 4.2. The photon fluctuates into a J/ψ particle which can be observed in the final state if the meson-proton interaction is elastic (9a) or single proton diffractive dissociation (9b).

Both H1 and ZEUS have studied the production of "elastic" J/ψ mesons.[60,28] The J/ψ mesons are identified by their decay into leptons (e or μ) which are required to be the only particles visible in the detector. In fact the data selected this way contain a mixture of

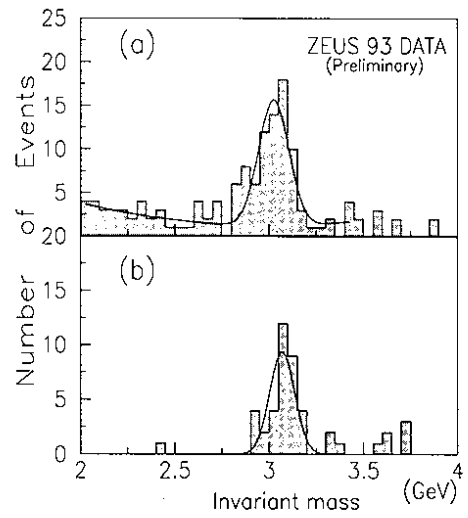

Figure 30: Invariant mass of lepton pairs in two-prong photoproduction events from ZEUS; (**a**) e^+e^-, (b) $\mu^+\mu^-$. The curves are fits to the preliminary data.

true elastic events and those where the proton breaks up into fragments (like in a diffractive dissociation process) which remain in the beampipe. In total 48 (40) muon (electron) pair events with 22 (10) in a region of ± 225 MeV around the nominal J/ψ mass, enter the H1 analysis, and 148 events the ZEUS analysis. The invariant mass of the lepton pairs is shown in Fig. 30. A clear signal is seen around the J/ψ mass of 3.097 GeV.

The cross section of $\sigma(\gamma p \to J/\psi + X)$ is $(56 \pm 13 \pm 14)$ nb at a mean $W_{\gamma p}$ of about 90 GeV for H1. In Fig. 31 the measured cross section for J/ψ production is shown as function of $W_{\gamma p}$, together with the preliminary ZEUS data. For comparison a diffractive and a QCD based model prediction are shown. Both models have free parameters which can be adjusted to the data. In the QCD model the "K-factor" was adjusted to describe the data at low $W_{\gamma p}$ and the MRSD–' or MRSD0' parton distributions[62] were chosen for the proton. The MRSD–' has a steeply rising gluon distribution for decreasing x while the MRSD0' has a rather flat gluon distribution (see chapter 5). Hence Fig. 31 shows the sensitivity of the measurement to the gluon distribution. Clearly MRSD–' describes the data better. In the diffractive model a substantial amount of proton dissociation has to be added to come close to the data.

A global way to search for heavy flavour production is the analysis of semi-leptonic decays into muons: $c\bar{c} \to \mu + X$. The H1 collaboration performed an analysis where the production of c and b quarks is tagged via high p_T muons. Events with a reconstructed muon with transverse momentum $p_T > 1.5$ GeV/c in the polar region $30° \leq \theta \leq 130°$ are selected. A severe problem for this measurement is the background which is dominated by muons from $\pi^{\pm}$, $K^{\pm}$ decays and fake muons: these are estimated to be responsible for half of the observed muons. After background subtraction the preliminary total photoproduction cross section derived is $\sigma(\gamma p \to c\bar{c} + X) = (3.6 \pm 0.8 \pm 1.8)\,\mu$b at a mean $W_{\gamma p}$ of about 114 GeV. The result

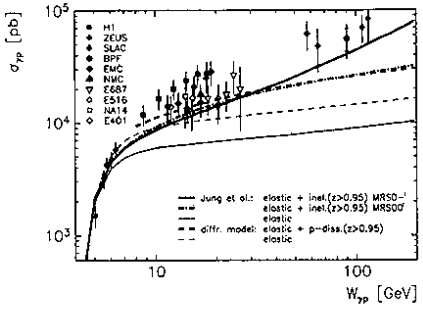

Figure 31: Total cross section for $\gamma p \to J/\psi + X$ from H1 and ZEUS. The data at lower CMS energies are from previous experiments; they were corrected with the new J/ψ decay branching ratio[56] and include systematic errors (added in quadrature). The dashed curves show the predictions from the VDM model in PYTHIA,[37] the thin dashed line is the elastic contribution only, the thick dashed line includes proton dissociation. The thick full line shows the QCD model by Jung et al.[57] with the MRSD–' parton density functions, the dash-dotted line with MRSD0'. The thin full line represents the purely elastic contribution in the QCD model.

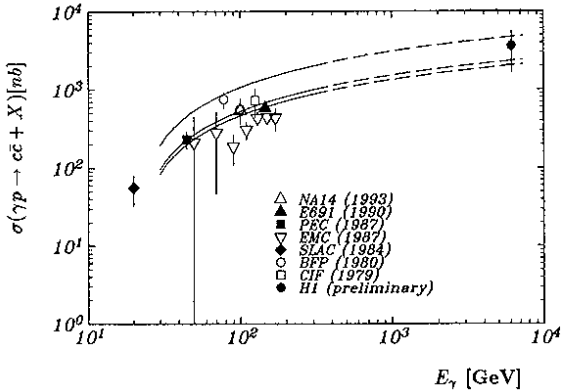

Figure 32: Total cross-section for $\gamma p \to c\bar{c} + X$, including the new preliminary data from H1. The solid curves show QCD calculations[61] for m_c=1.5 GeV and the dashed curves extrapolations to HERA energies assuming a logarithmic rise.

is shown in Fig. 32 together with earlier measurements at lower values of $W_{\gamma p}$and a QCD calculation by Ellis and Nason.[61]

The production of c quarks is further studied by tagging $D^{*\pm}(2010)$ mesons in the decay chain $D^{*\pm} \to D^0\pi_s^\pm, D^0 \to K^\pm\pi^\mp$. The mass difference distribution $m(K\pi) - m(D^0)$ shows a clear D^* peak and the $m(K\pi)$ mass distribution a clear D^0 peak (Fig. 33). ZEUS quotes

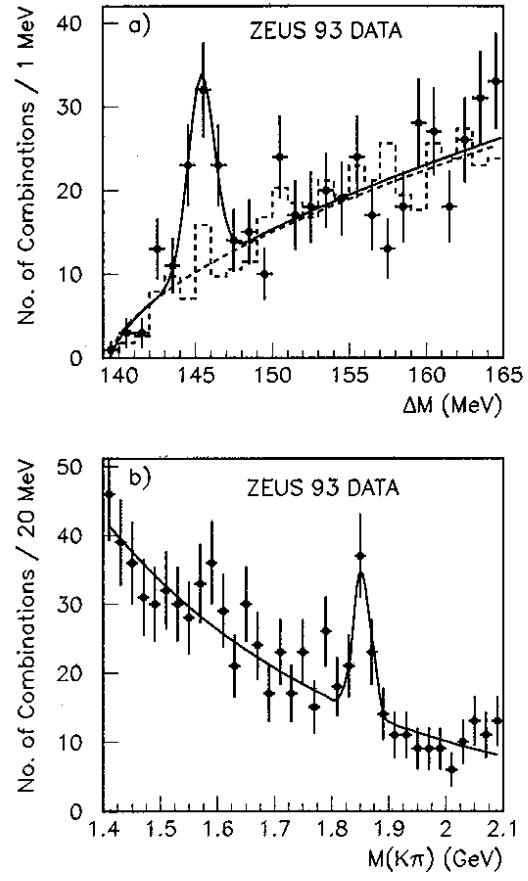

Figure 33: (a) ΔM distribution from ZEUS for photoproduction events having $1.80 < M(K\pi) < 1.93$ GeV: signal (dots) and wrong charge combinations (dashed histogram). The dashed line is a fit to the wrong charge background using the parametrization $A(\Delta M - m_\pi)^B$, where m_π is the mass of the pion. The solid line is a fit to the distribution, parameterised as a sum of the same function for the background plus a Gaussian for the signal. (b) $(K\pi)$ invariant mass distribution from ZEUS for those candidates with $142 < \Delta M < 149$ MeV. The fitting function is the sum of a Gaussian and an exponential.

a cross section of $\sigma(ep \to D^{*\pm} + X) = (32 \pm 7(\text{stat})^{+4}_{-7}(\text{syst}))$ nb[63] in the kinematic region of $p_T(D^*) > 1.7$ GeV, $|\eta(D^*)| < 1.5$ and $115 < W < 275$ GeV (and $Q^2 < 4$ GeV^2). This leads to a total charm cross section measurement of $\sigma(ep \to c\bar{c} + X)$ of $(6.3 \pm 2.2^{+6.3}_{-3.0})$ μb at $\langle W \rangle = 163$ GeV and $(16.9 \pm 5.2^{+13.9}_{-8.5})$ at $\langle W \rangle = 243$ GeV. This measurement is compatible with the results of the H1 muon analysis.

5 Deep Inelastic Scattering

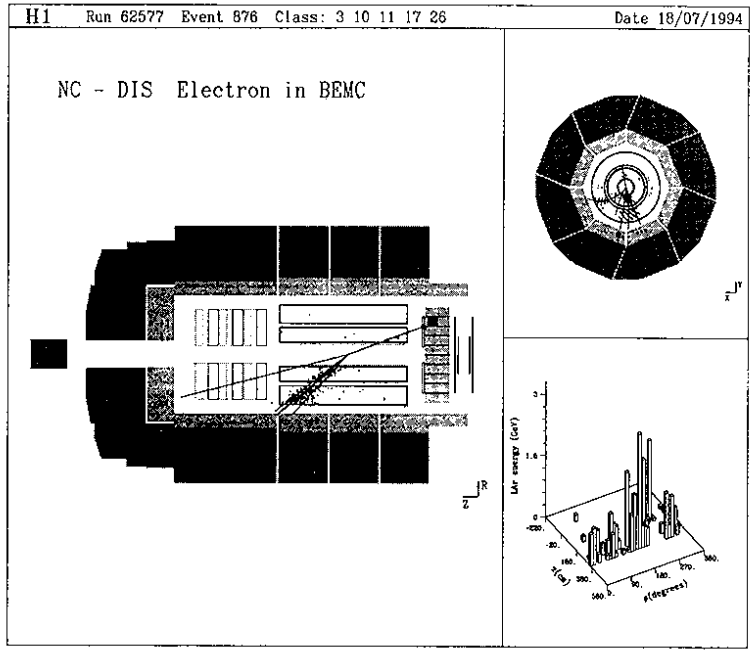

Figure 34: Example of a neutral current deep inelastic scattering event in the H1 detector. The electron is detected in the BEMC calorimeter, the hadronic final state in the main liquid argon calorimeter and central tracker.

The centre of mass energy squared $s = 87600$ GeV^2 at HERA opens a completely new kinematical domain to study deep inelastic scattering. Four-momentum transfers Q^2 of up to a few times 10^4 GeV^2 and x values down to about 10^{-4} can be reached. Compared to fixed target experiments, this is an extension of the kinematical domain by almost two orders of magnitude in both x and Q^2. Another advantage of the experiments at HERA is their ability to detect the full hadronic final state, apart from losses in the beampipe. This allows to determine the kinematical variables from the scattered electron, the hadronic final state, or a mixture of both. Further it enables one to study properties of hadron production in the final state.

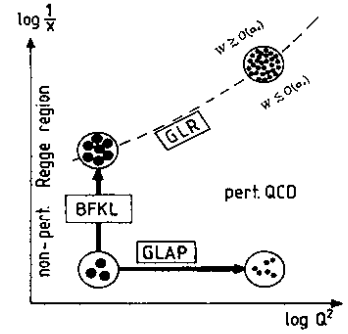

Figure 35: Schematic evolution of the quark densities in various (x, Q^2) regions according to the dominant dynamical effects. The dashed line is the theoretical limit of validity of perturbative QCD.

For values of Q^2 well below the mass squared of the W and Z^0 gauge bosons, the dominating process is the photon exchange process, thus most DIS events produced at HERA are neutral current events: the scattered lepton is an electron. A typical neutral current deep inelastic event is shown in Fig. 34 in the H1 detector. The scattered electron, detected in the BEMC calorimeter, is well isolated from the hadronic final state, which generally balances the electron in p_T. Note that around the beampipe, in the proton direction, some activity is seen which can be attributed to the fragmentation of the proton remnant or to the colour flow between current and remnant.

In this chapter we will discuss new results on the structure of the proton: the F_2 structure function measurements and attempts to extract the gluon distribution from these data. Further we will discuss the hadronic final state in DIS events, showing that with the present available data, the fragmentation of the current quark in lepton-hadron scattering and quarks produced in e^+e^- annihilation interactions is quite similar. However, the region between the current quark and the proton remnant turns out to be less understood, leaving room for the onset of new QCD effects. Finally, a quite different type of events has been found at HERA, in which no colour flow is seen between the system including the current quark and the proton remnant. These so called "rapidity gap" events are not yet fully understood, but turn out to be compatible with diffractive processes, similar to the ones discussed in the chapter on photoproduction. Hence HERA is likely to shed light on the dynamics of diffractive processes, known for about 30 years in hadronic physics, but not yet unambiguously explained within QCD.

5.1 Structure Functions

An introduction to the subject of structure functions can be found in the lectures of A. Mueller, in these proceedings. Basically, the structure function F_2 of the proton is derived from the one-photon exchange cross section:

$$\frac{d^2\sigma}{dxdQ^2} = \frac{2\pi\alpha^2}{xQ^4}(2 - 2y + \frac{y^2}{1+R})F_2(x, Q^2) \qquad (5)$$

where $d^2\sigma/dxdQ^2$ is the Born cross section, i.e. corrected for radiative events. Radiative events are events where a photon is emitted, mostly from the incoming or scattered electron. Consequently the x, Q^2 values measured from the scattered electron do not correspond to the true "x_t,Q_t^2" values of the genuine ep interaction. At higher $Q^2 > 1000$ GeV^2, effects due to Z^0 exchange have to be taken into account, but these remain small ($\sim 5\%$) for the data presented here. R is the ratio of the longitudinal to transverse photon absorption cross section and relates the structure functions F_1 and F_2 by $R = F_2/xF_1 - 1$. This quantity has not yet been measured at HERA, but calculations using the NLO QCD relations[64] lead us to expect that the effect on the F_2 measurements presented here is at most 5-10%.

Structure function measurements are a key ingredient for the determination of parton distributions in nucleons. These parton distributions $f_i(x)$ give the probability to find a parton i with a momentum fraction x from the original proton momentum. Precise knowledge of parton distributions is important, for example for the calculation of production rates of hadronic processes which can be described by perturbative QCD. Since future high energy colliders (e.g. the LHC) will be sensitive to x values of $O(10^{-3}-10^{-4})$, measurements at HERA will be a key input for understanding the production rates for QCD processes. Moreover, the dynamics that generates parton distributions at low x is a field of strong theoretical interest. In particular, novel perturbative QCD effects could show up at x values below 10^{-3}, as we will discuss below.

The behaviour of the parton distributions at small values of x was, prior to HERA data, dictated by data from fixed target muon-proton experiments, which include measurements down to $x = 8.10^{-3}$.[80] For smaller x values there was no direct guide from data, leaving room for theoretical speculation on the behaviour of the parton distributions in this region.[66] In fact, extrapolations of parton distributions varied wildly in the low x region. These extrapolations were often motivated by either studying the asymptotic behaviour of perturbative QCD evolution equations, or by expectations based on Regge theory. Until now mostly the Dokshitzer-Gribov-Lipatov-Altarelli-Parisi (DGLAP) QCD evolution equations[67] have been used to study and successfully interpret the Q^2 evolution of the available deep inelastic data from fixed target experiments, which are essentially limited to the region $x > 10^{-2}$.

However, the linear evolution equation particularly adapted to study the small x region is the Balitskii-Kuraev-Fadin-Lipatov (BFKL) equation.[68] This is an evolution equation in the variable x, i.e. it relates the parton densities at a value x_0 to any value x. This equation can so far only be used to predict the evolution of the gluon density and is calculated up to LO in QCD. The BFKL equation predicts a characteristic $x^{-\lambda}$ behaviour of the gluon density at small x, with $\lambda \sim 0.5$. At low x the sea quark distribution is expected to be driven by the gluon distribution, thus the $F_2(x, Q^2)$ evolution at small x is expected to reflect the behaviour of $xg(x)$. A $x^{-0.5}$ behaviour of the gluon density will result in a rapid growth of $F_2(x, Q^2)$ with decreasing x.

This perturbative QCD result has to be contrasted with the expectations of the Regge limit where it is expected that $xg(x) \sim x^{1-\alpha_{\mathbf{P}(0)}}$, with the soft Pomeron intercept $\alpha_{\mathbf{P}(0)} \simeq 1$, hence $xg(x) \sim$ constant. This could be a valid scenario for not too large Q^2, but for $Q^2 > 10$ GeV^2 eventually perturbative effects as prescribed by the DGLAP equations, have to become more and more visible.

The DGLAP evolution equations can in fact also cause F_2 to rise at low x. These equations, contrary to the BFKL equation, prescribe the evolution in Q^2, i.e. one can calculate parton densities for $Q_0^2 \rightarrow Q^2$, but one needs an explicit non-perturbative input distribution of the x behaviour at a starting Q_0^2. The different approach in evolution for BFKL and DGLAP is pictured in Fig. 35. In principle using the DGLAP equations at low x is questionable since these account only partially for the $\ln 1/x$ terms, which become large at low x. The choices for the non-perturbative input at the scale Q_0^2 can range from a flat – Regge inspired soft

Pomeron – behaviour, to an already steeply rising – BFKL inspired – behaviour. It will be demonstrated in the next section that the rise of F_2 at small x is either a result of the choice of the non-perturbative input, or a result from the lever arm in evolution in Q^2.

Since $F_2(x, Q^2) \sim \sigma_{tot}^{\gamma^*}$ a continuing increase of F_2 can lead to an unphysical blowup of the cross section. Therefore, it is expected that at very small x the rise should be damped by a new mechanism. A proposed scenario is that at small x the parton densities become so large that annihilation and recombination of parton pairs will start to compete with the parton decay processes included in the standard evolution equations. These "screening" or "shadowing" effects damp the fast increase of the parton density. Such processes have been included in the Gribov-Levin-Ryskin (GLR) equation,[69] and the qualitative results are shown in Fig. 35. In the $x - Q^2$ plane a region will be reached where strong non-linear effects due to parton recombination become important. The border line of this region is often termed the "critical" line. It is however not clear if HERA data will finally probe this new region, since the position of the critical line depends strongly on the strength of the rise of the gluon density at small x. However, an observed strong rise of $F_2(x, Q^2)$ at HERA considerably enhances the probability of observing these novel effects at small x values.

Both the H1 and ZEUS experiments have released new data on structure function measurements[70,15] at small x. We have noted in chapter 1 that, to determine the kinematical variables x and Q^2, we can use two out of four experimentally accessible quantities: energy E'_e and angle θ_e of the scattered electron, and energy E_h and average angle θ_h of the hadron flow. The ultimate method is a global fit of all observed quantities, which requires a level of understanding of the detector response and of the error correlations that the experiments have not yet achieved. In total four methods are currently used in the analyses to reconstruct the event kinematics. The electron method (1), as given in eqn. 2 is the method used so far in all fixed target experiments. It remains at HERA the most precise way to reconstruct Q^2 in the whole kinematic range. However at low y ($y < 0.1$) the measurement of x becomes poor[71] and at large y ($y > 0.8$) the radiative corrections to apply to the observed cross section to extract the Born cross section are very large.[72] The mixed method (2) used by the H1 collaboration in 1992 takes Q^2 from the electron according to eqn. 2 and y from the hadronic variables (y_{JB}) according to eqn. 3. The resolution of y_{JB} is better than the resolution of y_e for low y values but becomes inferior at large y values. For the double angle method (3)[73] only the angles of the scattered electron and the hadronic system are used. The method is almost independent of energy scales in the calorimeters but, at very low y, the method is very sensitive to noise in the calorimeters. The variables y and Q^2 are reconstructed from

$$y_{DA} = \frac{\sin\theta_e(1-\cos\theta_h)}{\sin\theta_h + \sin\theta_e - \sin(\theta_e+\theta_h)} \tag{6}$$

$$Q^2_{DA} = 4E_e^2 \frac{\sin\theta_h(1+\cos\theta_e)}{\sin\theta_h + \sin\theta_e - \sin(\theta_e+\theta_h)} \tag{7}$$

$$\tan\frac{\theta_h}{2} = \frac{\Sigma_h(E-P_z)_h}{P^2_{T,h}} \tag{8}$$

A new method used by the H1 collaboration,[70,74] called the Σ method (4), combines y from the following expressions: :

$$y_\Sigma = \frac{\Sigma_h(E-P_z)_h}{(E-P_z)_e + \Sigma_h(E-P_z)_h} \tag{9}$$

where the sum runs over all hadrons in the numerator and over all hadrons plus the scattered electron in the denominator, and Q^2

$$Q^2_\Sigma = \frac{E'^2_e \sin^2\theta_e}{1-y_\Sigma} \tag{10}$$

In this method the energy of the incident electron in the interaction is reconstructed, which reduces drastically the sensitivity to the main radiative process. The resolution in x at low y is good enough to allow the H1 collaboration to reach $y = 0.01$. The resolution at large y is worse but less sensitive to radiative corrections than when using only the measurement of the scattered electron. For precision measurements of the structure function all of the different methods are used to control the systematics of event smearing and radiative corrections.

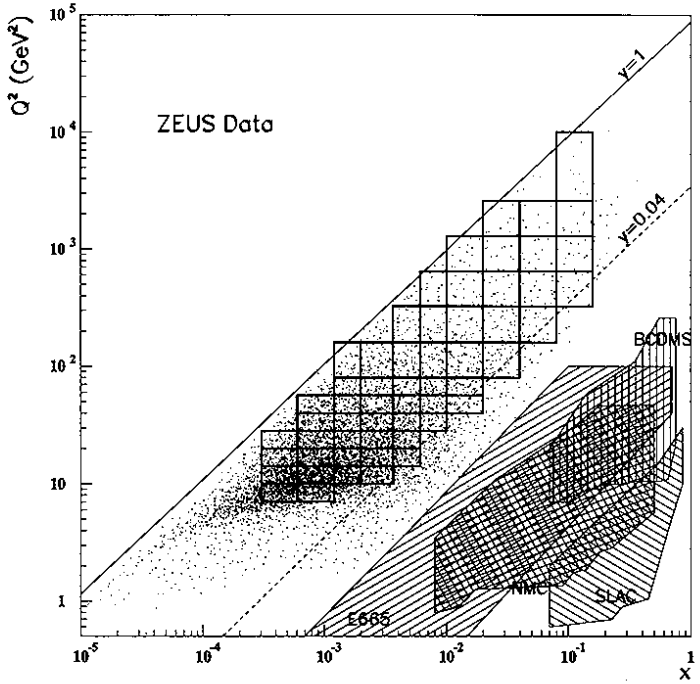

Figure 36: Distribution of the neutral current event sample in the $x-Q^2$ plane. The regions covered by fixed target experiments are shown, together with $x-Q^2$ bins used by ZEUS for the F_2 measurement.

For the final presentation of the results, ZEUS uses the double angle method, while H1 uses the electron method at high y (roughly $y > 0.15$) and the Σ method at low y. The distribution of the events in the $x-Q^2$ plane is shown in Fig. 36 for ZEUS, together with the regions covered by data from fixed target experiments.

Already the analysis of the 1992 data revealed the interesting and perhaps somewhat unexpected result that the proton structure function F_2 rises strongly towards low x.[75,76] However, the significance was limited due to the statistics. The high statistics of the 1993 data enables us to make a more precise measurement and extend the analysis to higher values of $Q^2(\sim 2000\ \mathrm{GeV}^2)$. Also very low values of $Q^2(4\text{–}8\ \mathrm{GeV}^2)$ could be studied, due to a few hours of data taking when the interaction point was shifted by 80 cm towards the proton direction in order to increase the detector acceptance for electrons scattered under very small angles.

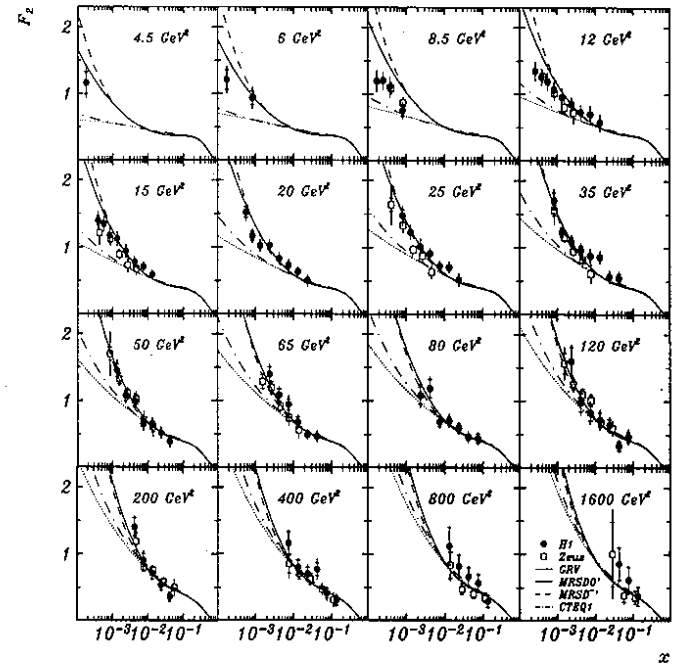

Figure 37: The proton structure function from H1 (full points[70]) and ZEUS (open points[15]) as a function of x for different values of Q^2. The inner error bars show the statistical error, the outer error bars include the systematical error added in quadrature. An overall normalization uncertainty of 4.5% for H1 and 3.5% for ZEUS is not shown. The curves represent pre-HERA fits to previous data.

Fig. 37 shows the result for F_2, obtained by H1 and ZEUS from the '93 data. The strong rise observed in the '92 data is definitely confirmed with much higher statistical significance. The data of both experiments are found to agree nicely. In Fig. 39 a summary plot is shown with the new data from HERA and the new data from E665[77] as a function of Q^2 at fixed x, compared to published fixed target data. The HERA data agree with a smooth extrapolation from SLAC,[78] BCDMS,[79] NMC[80] and E665 data. Positive scaling violations are clearly visible at low x and are more and more pronounced as x decreases.

5.2 Comparison of F_2 with Model Predictions

In Fig. 37 predictions for F_2 are shown, calculated from parton density parametrizations which were available prior to the data from HERA. All these calculations assume a certain shape of the x behaviour at small x –where no measurements existed– at a Q_0^2 value and use DGLAP equations to get predictions at other values of Q^2. For the MRS[81] distributions two

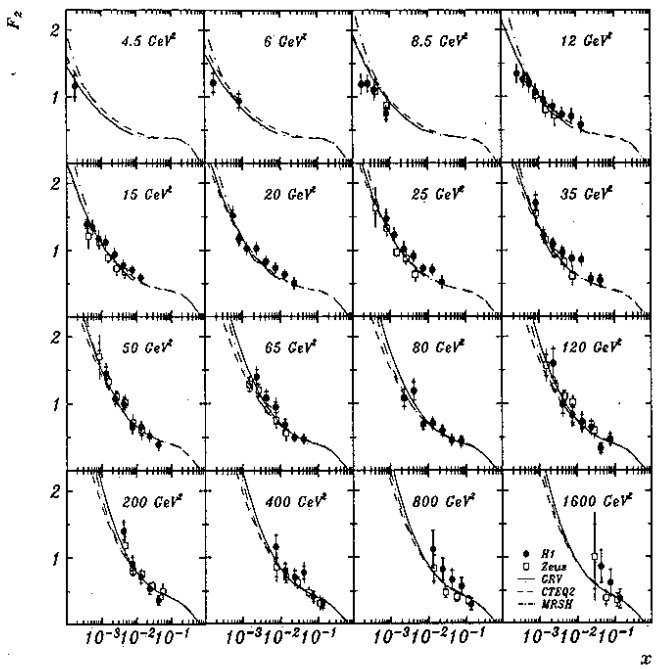

Figure 38: The proton structure function from H1 and ZEUS (same data as Fig. 37). The curves show fits including 1992 HERA data.

different scenarios were proposed for the behaviour for $x \to 0$ at a starting $Q_0^2 = 4$ GeV^2: a flat, Regge inspired behaviour (MRSD0'; $\sim x^0$) and a singular, Lipatov inspired behaviour (MRSD−'; $\sim x^{-0.5}$). These parton distributions are evolved in Q^2 with the DGLAP evolution equations, and show that a flat input becomes indeed rather singular for $Q^2 >> Q_0^2$. However the MRSD−' remains steeper than the MRSD0' for all Q^2 values. The CTEQ1MS approach is similar to the MRSD−' approach, but here the sea-quark distributions are not forced to be strongly coupled to the gluon distribution. The parametrization shown contains a singular gluon distribution, but the F_2 extrapolated in the small x region turns out to be rather flat in x. This results in an F_2 prediction from CTEQ1MS which is close to the MRSD0' calculation. The data clearly exclude the MRSD0'/CTEQ1MS scenarios, and favour more a scenario such as MRSD−'. For $Q^2 < 15$ GeV^2 however, the MRSD−' prediction tends to rise too fast compared to the data.

The GRV[82] calculation assumes that parton distributions at a very low Q^2, namely $Q_0^2 = 0.3$ GeV^2, have a valence quark behaviour, i.e. they are expected to vanish for $x \to 0$. The functional form used is $x^\alpha(1-x)^\beta(\alpha > 0)$ for the parton distributions to fit to fixed target data. These data fix the prediction and there is little or no freedom left for further adjustments at HERA. Despite the valence behaviour ansatz, which results in a dramatic decrease of the

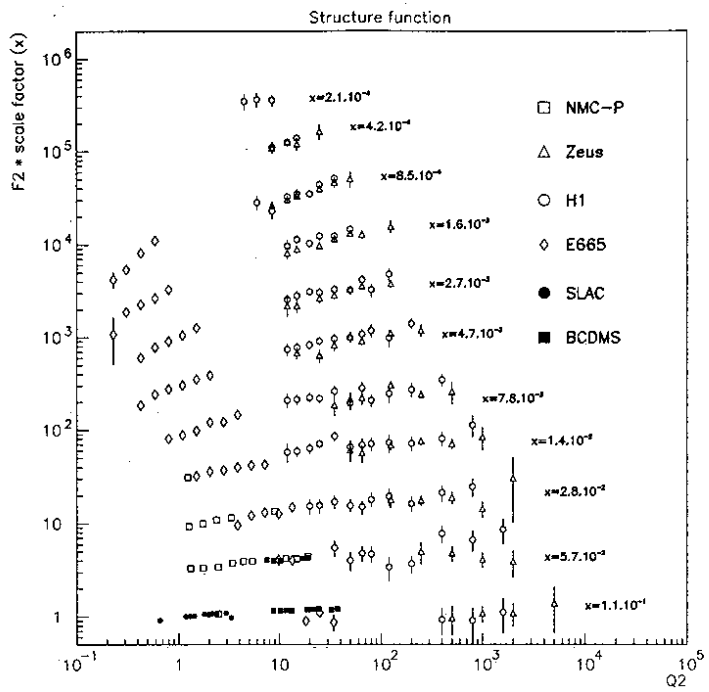

Figure 39: $F_2(x, Q^2)$ at fixed x values as a function of Q^2 from H1 and ZEUS together with data points from E665, SLAC, NMC and BCDMS in the same x bins as the HERA experiments. The data points of fixed target experiments have been slightly rebinned in x to match the HERA values. The error bars show the total errors. For clarity of the picture, common scale factors which are different for the different x values have been applied to all data sets.

parton distributions at small x for small Q^2, the predictions show a strong rise over the measured Q^2 range. This is a result of the long lever arm used in the DGLAP evolution from the starting scale Q_0^2 to measured Q^2 values. Note that differences are apparent between the MRSD−' and GRV at low x and low Q^2, slightly favouring the GRV distributions.

The 1992 HERA data clearly gave a major clue on the behaviour of F_2 in the new small x domain, for the region $Q^2 \geq 8.5$ GeV^2. These data were subsequently used in fits by the MRS and CTEQ group to produce new parametrizations. The results are shown in Fig. 38. The new CTEQ and MRS distributions now evidently show better agreement with the data. Note that also the new, lower Q^2 region is rather well described. The GRV distributions were updated w.r.t. to the treatment of the charm quark threshold in the evolution, which affects mainly the lower Q^2 region.[83] These distributions also show a good agreement with the data, which is less trivial, since these do not include the HERA measurements in the fit. In general one can say that parametrizations using the DGLAP equations are able to describe our data, provided a suitable non-perturbative input is chosen (e.g. $\sim x^{-0.3}$ for MRSH[84]), or a large lever arm is taken for the DGLAP evolution (GRV).

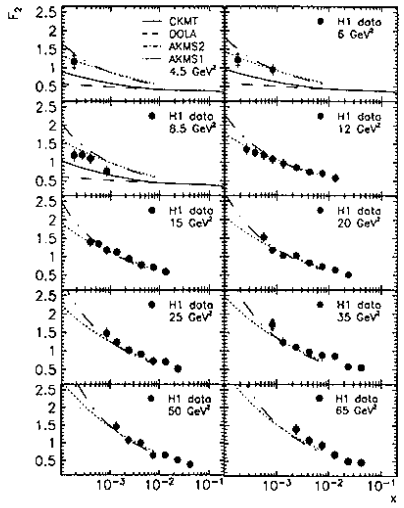

Figure 40: The proton structure function from H1 as a function of x for low Q^2 values, compared with model predictions described in the text: DOLA (dashed lines), CKMT (solid line), AKMS without shadowing (dash-dotted line), AKMS with shadowing (dotted line).

In Fig. 40 we have a closer look at the low Q^2 region, comparing the data with parametrizations based on the BFKL – instead of the DGLAP – evolution equations, and with some recent prediction of Regge theory inspired models.

The Regge theory motivated parametrization relates the structure function to Reggeon exchange phenomena which successfully describe e.g. the rise of the total cross section in hadron-hadron collisions and γp interactions. Using the "bare" instead of the "effective" Pomeron intercept to guide the calculations, the new CKMT predictions[85] rise faster with x compared to former DOLA calculations.[86] The latter ones were already shown to be significantly below our '92 data. The CKMT curves shown were calculated using the Pomeron intercept $1 - \Delta$, with $\Delta = 0.25$ and without the QCD evolution term, hence they are compared the data in the lowest Q^2 bins only. The newly measured F_2 at small Q^2 values, down to 4.5 GeV^2 opens a new region for testing this Regge assumption. Fig. 40 shows that the parametrization undershoots the data at low Q^2.

The Durham group has used the BFKL evolution equations to predict the x dependence of F_2 at low Q^2.[87] Here we show the sets AKMS1 and AKMS2. The difference between these two sets is the effect of gluon shadowing at very small x. AKMS1 does not include shadowing, while AKMS2 represents the scenario of "hot spots", i.e. it is assumed there are small regions in the proton where shadowing has set in. From Fig. 40 it is shown that these parametrizations describe the data with a similar quality to the ones shown in Fig. 38, based on the DGLAP evolution equations. A similar calculation was presented[88] by another group.

Shadowing was recently studied[89] using the GLR equation, and it was found that it will be necessary to detect electrons at smaller scattering angles at HERA to have a chance to identify these effects. Furthermore, restoring the momentum sum rule in the GLR equation introduces additional "anti-shadowing" terms,[90] which will reduce the shadowing effect.

In summary, it turns out that the present data can be described by both approaches: assuming the parton evolution to be dictated by DGLAP or BFKL evolution equations. Presently proposed Regge inspired models are somewhat disfavoured by the data but can most likely be rescued by lowering the Q_0^2 value of the initial non-perturbative part and allow for more QCD evolution lever arm. In the currently covered x, Q^2 range the effect of shadowing is probably small. More precise future data and, in particular, data at lower x values could shed important light on these assumptions and have the potential to discriminate between scenarios. Such data will become available at HERA in the near future from special runs and by the improved coverage of the detectors for DIS events with the electron scattered under small angles.

5.3 QCD Interpretation of F_2 and Determination of the Gluon Density

In this section the F_2 data will be analysed in the framework of perturbative QCD. LO and NLO QCD fits to F_2 will be shown, as well as approximate methods to extract the gluon.

In section 5.2 it was shown that the GRV distributions are in accord with the data. These distributions are essentially generated by the DGLAP equations and probed in a region ($Q^2 > 5$ GeV^2) far away from the scale of the starting distributions ($Q_0^2 = 0.3$ GeV^2). A similar analysis[92] showed that evolving a flat input distribution with the DGLAP equations at a scale of $Q_0^2 = 1$ GeV^2 leads to a strong rise of F_2 at low x in the region measured at HERA. An interesting feature is that if pure DGLAP evolution is the underlying dynamics of the rise, the structure function should exhibit scaling in the two variables $\sqrt{(\ln 1/x)(\ln\ln Q^2)}$ and $\sqrt{(\ln 1/x)/(\ln\ln Q^2)}$ at sufficiently large Q^2 and low x values.[91,92] This confirms a prediction from 1974[93] where the asymptotic form of $F_2(x, Q^2)$ at small x had been calculated based on the operator product expansion and renormalization group at leading perturbative order.

In order to test the prediction of double asymptotic scaling we present the F_2 data in a different way.[92] The variables ρ and σ are defined as $\sigma \equiv \sqrt{\ln\frac{x_0}{x}\ln\frac{t}{t_0}}$ and $\rho \equiv \sqrt{\ln\frac{x_0}{x}/\ln\frac{t}{t_0}}$ with $t \equiv \ln(Q^2/\Lambda^2)$. The starting values of the evolution x_0 and Q_0^2 are chosen to be $x_0 = 0.1$ and $Q_0^2 = 1$ GeV^2. To present the data as a linear dependence on σ in the region of scaling, the F_2 is rescaled by a factor $R'_F \equiv N\sqrt{\sigma}\rho e^{\delta\sigma/\rho}$, with $\delta = 61/45$ for four flavours and three colours. Fig. 41 shows clearly a linear rise of $\ln(R'_F F_2)$ with σ, confirming scaling in this variable in the range of the data. For this figure only data with $\rho^2 > 2$ are included, which means that points with $x > 0.02$ are excluded, and Λ was taken to be 240 MeV. The LO prediction for the slope of σ with $\ln R'_F F_2$ is 2.4, but higher order corrections are expected to reduce the slope[94] somewhat. A linear fit $\ln R'_F F_2 = a\sigma + c$ to our data gives a (preliminary) slope $a = 2.07 \pm 0.03$(stat.). Changing Λ by 40 MeV changes the value of the slope by 5%.

Scaling in ρ can be shown by multiplying F_2 with the factor $R_F \equiv R'_F e^{-2\gamma\sigma}$. We observe scaling for $\rho \geq 1.5$ in Fig. 41. This figure is interesting also because the presence of a 'hard Pomeron' behaviour, as given by the BFKL dynamics, is expected to violate the scaling by producing a rise at high ρ. With the available data a moderate increase at high ρ is not excluded. However, also the inclusion of higher loop corrections is expected to give a rise at high ρ.[94] In all, double asymptotic scaling seems to work quite well in the region of our data.

Next, we turn to the extraction of the gluon distribution $xg(x)$ in the proton. A first glimpse of the gluon was already presented in section 4.5, in the discussion of the production of heavy quark flavours in γp interactions. Here we will extract the gluon distribution from the

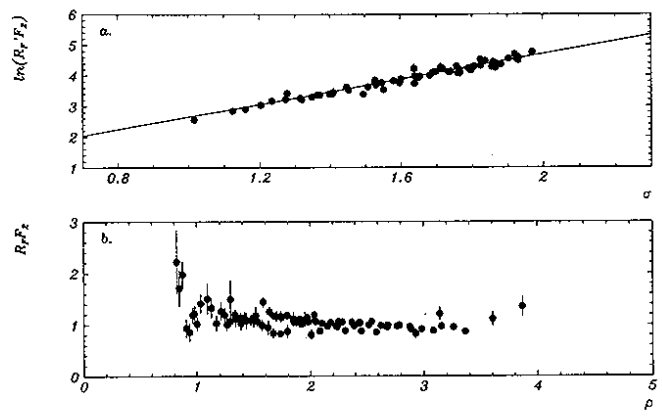

Figure 41: The rescaled structure functions $R'_F F_2$ and $R_F F_2$ plotted against (a) σ and (b) ρ where $\sigma = \sqrt{\ln \frac{x_0}{x} \ln \frac{t}{t_0}}$, $\rho = \sqrt{\ln \frac{x_0}{x} / \ln \frac{t}{t_0}}$ and $t_0 = \ln Q_0^2/\Lambda^2$. The starting values are $x_0 = 0.1$ and $Q_0^2 = 1$ GeV^2. R_F and R'_F are simple rescaling factors explained in the text.

structure function measurements. Assuming the DGLAP equations to be valid, the behaviour of $dF_2/d\ln Q^2$ can be used to extract the gluon density in the proton. H1 performed a leading order QCD fit to the F_2 data using only its own data.[39] The result is shown in Fig. 42. Parameters relevant to the high x region have been fixed to values known from fixed target experiments; Λ_{QCD} was set to 240 MeV and the momentum sum rule was imposed. Free parameters are the exponent λ in the gluon distribution $xg(x) \sim x^{-\lambda}$ and the exponent and normalization of the quark-singlet distribution. The χ^2 of the fit is 65 for 86 degrees of freedom, which shows again that the data with the current precision can be described by LO QCD and DGLAP evolution. We obtain $\lambda = 0.38 \pm 0.08$ at $Q^2 = 20$ GeV^2. The fit is shown in Fig. 42a for a Q^2 of 20 GeV^2 as a function of x. ZEUS performed a next to leading order fit, including the NMC and BCDMS data.[28] The NLO fit takes the functional form for the singlet, valence, non-singlet and gluon distribution form the MRS parametrizations. From the fit a value of $\lambda = 0.35$ for a $Q^2 = 7$ GeV^2 is obtained. The result is shown in Fig. 42b.

Several approximative methods have been used to deconvolute the gluon density. The method proposed by J. Prytz[95] consists of neglecting the quark contribution and doing a Taylor expansion of the splitting function around $x = \frac{1}{2}$, leading to a very simple LO expression of the gluon density :

$$xg(x,Q^2) \approx \frac{27\pi}{20\alpha_s(Q^2)} \frac{\partial F_2(\frac{x}{2},Q^2)}{\partial \ln Q^2} \qquad (11)$$

It is a crude approximation which is expected to hold to within 20% at $x = 10^{-3}$ for a steeply rising gluon.[96] Approximate NLO corrections have been calculated.[97,95] The method of Ellis, Kunszt and Levin (EKL) consists in solving the DGLAP evolution equation in momentum space.[98] This leads to the following relation,

$$xg(x,Q^2) = f_1 \otimes \frac{\partial F_2(x,Q^2)}{\partial(\ln Q^2)} + f_2 \otimes F_2(x,Q^2) \qquad (12)$$

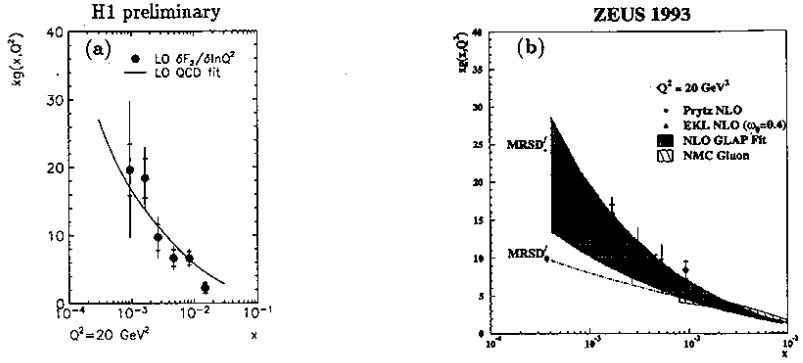

Figure 42: (a) The preliminary gluon density $xg(x,Q^2)$ as a function of x at $Q^2 = 20$ GeV^2 as obtained from a LO QCD fit of the H1 F_2 data (full line), and from an analysis of the H1 F_2 data according to the LO Prytz prescription. (b) The gluon density $xg(x,Q^2)$ from the ZEUS collaboration using a NLO QCD fit, the NLO Prytz method and the NLO EKL method. In the EKL method it is assumed that F_2 behaves in $x^{-\omega_0}$ with $\omega_0 = 0.4$. Also shown are the parametrizations MRSD–' and MRSD0'.

where f_1 and f_2 are known functions to fourth order in α_s and depend on the slope of F_2 in x. The relation is only valid when F_2 has a steep rise at low x. The results for both approximations are shown in Fig. 42.

The errors on the gluon distribution are still large but the message is clear, at $Q^2 = 20$ GeV^2 $xg(x)$ rises by about a factor 5 to 10 as x decreases from 10^{-1} to 10^{-3}. It exhibits a $x^{-\lambda}$ behaviour with $0.2 < \lambda < 0.5$. The NLO gluon data have also been compared to the MRSD0' and MRSD–' parametrizations. The gluon data disfavour the MRSD0' parametrization, in accord with the F_2 measurements and the results of heavy quark production in γp. If this rise continues with decreasing x, these gluons are expected to saturate the transverse size of the proton. A naïve calculation on the limit where the uniform gluon density saturates the proton[99] leads to $xg(x) \simeq 6Q^2$, Q^2 in GeV^2. Hence the data are still well below this limit.

In summary, it is now unambiguously established that the structure function rises at small x for Q^2 values down to 4.5 GeV^2. Models which do not predict such strong rise are disfavoured by the data. From the scaling violations of F_2 it follows that also the gluon distribution rises strongly with decreasing x. The inclusive F_2 measurement has turned out not to be conclusive (yet) on the question of whether HERA data at low x are in a new region where conventional DGLAP fails and BFKL evolution has to be used instead. Therefore, it was suggested that additionally exclusive final states should be studied. These are expected to show sensitivity to QCD evolution in the initial state, a topic which will be discussed in the next section.

5.4 The Hadronic Final State: Spectra and Multiplicities

In the naïve quark-parton model (QPM) the transverse momentum of the scattered electron is balanced by a single jet resulting from the hadronization of the struck quark, usually called the current jet. Higher order QCD processes modify this picture. Examples of first order processes are shown in Fig. 43, namely photon-gluon fusion (PGF) and QCD Compton (QCDC) processes. These processes can lead to multi-jet final states and can be used to determine e.g. the strong coupling constant α_s or to make a direct measurement of the gluon

distribution $xg(x)$. An important question is: what is the nature of the quark kicked out by the exchanged boson? Is it the same object as a quark created in e.g. e^+e^- annihilation? The observed jet universality observed in available e^+e^- and lepton nucleon and data at lower energies clearly hint in that direction, but new tests at higher energies are essential. In this section we will compare the spectra and event multiplicities with those from e^+e^- and low energy lepton-hadron experiments to further check this hypothesis in the HERA kinematical domain.

Predictions for the properties of hadronic final states are available in the form of analytical calculations and Monte Carlo models, which are in general based on standard QCD evolution. In this report we will refer only to two of the currently available Monte Carlo programs: the MEPS and CDM models. The MEPS model is an option of the LEPTO generator[100] based on DGLAP dynamics. MEPS incorporates the QCD matrix elements up to first order, with additional soft emissions generated by adding leading log parton showers. The CDM model[101] provides an implementation of the colour dipole model of a chain of independently radiating dipoles formed by emitted gluons. Since all radiation is assumed to come from the dipole formed by the struck quark and the remnant, photon-gluon fusion events have to be added and are taken from the QCD matrix elements. It is claimed that CDM should approach more the BFKL type of evolution[102] although it does not explicitly include the BFKL evolution equation.

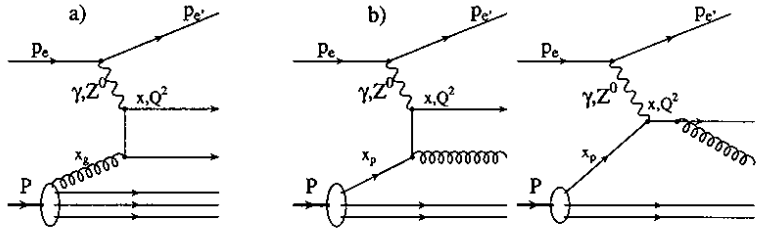

Figure 43: Feynman diagrams for (a) the photon-gluon fusion process and, (b) the QCD-Compton process.

Charged particle production has been studied by both collaborations. Results are presented in the hadronic CMS and in the Breit frame. The hadronic CMS frame is defined as the centre of mass system of the incoming proton and the virtual photon, i.e. the centre of mass system of the hadronic final state with invariant mass W. The z-axis is defined by the direction of the virtual photon. In the quark parton model, the scattered current quark and the proton remnant are back to back along the z-axis. Traditionally the current quark region is defined by all particles with longitudinal momentum $p_z > 0$. A further linear boost along the z-axis from the hadronic centre of mass frame can give a system in which the exchanged current is entirely space-like, having just a z-component of momentum $-Q$. This is called the Breit frame and has been claimed[103] to be the preferred system to study current quark properties because the separation of remnant from current region is theoretically easier to handle. In the simple QPM picture the convention is used that the incident parton approaches with momentum $+Q/2$, absorbs the photon, and leaves with momentum $-Q/2$, in what is called the current hemisphere.

In Fig. 44 the x_F distribution of charged particles is shown for DIS events in the CMS system, compared to results from e^+e^- interactions. The data are corrected for detector effects.[104] The variable x_F is defined as $2p_z/W$, hence Fig. 44 shows essentially the result

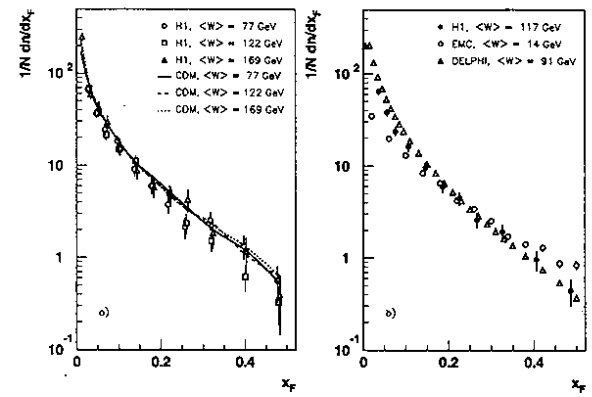

Figure 44: Scaled charged particle spectrum x_F in the hadronic CMS frame. The distributions are normalized to the number of events, and n refers to the number of charged particles in a given bin. In (a) the H1 data for three different W bins are shown, together with the CDM Monte Carlo prediction. In (b) the H1 data are compared with data from EMC and DELPHI. The DELPHI data are divided by two to account for the two jets in e^+e^- annihilation.

of the current quark fragmentation. Compared to lepton-hadron collisions at lower energy (EMC, $\langle W\rangle$=14 GeV), the HERA data (H1, $\langle W\rangle$=117 GeV) are clearly falling steeper, an indication for QCD induced scaling violations, which have been observed in e^+e^- interactions as well.[105] The HERA data compare quite well with the e^+e^- data (DELPHI, $\langle W\rangle$ = 91 GeV) at a similar hadronic centre of mass energy for the region of $x_F > 0.15$.

Next we investigate the $\langle p_t^2\rangle$ in the CMS frame, in the current quark region. In the simple QPM diagram the quark and proton remnant are back to back, along the z-axis such that the p_T comes essentially from the fragmentation. The QCD diagrams shown in Fig. 43 and similar higher order diagrams are expected to give a significant rise of the p_T with increasing CMS energy. This is shown in Fig. 45 for the lower energy (EMC) and the HERA (ZEUS) data. A clear rise is observed with increasing W. The $\langle p_t^2\rangle$ and the rise with $\langle W\rangle$ is larger for high x_F values compared to lower ones. Fig. 45 also shows a comparison made as function of Q^2 instead of W. It is tempting to conclude that W and not Q^2 is the variable controlling the increase of $\langle p_t^2\rangle$, however one has to note that x_F is not a Lorentz invariant variable.

In Fig. 46a the average charged multiplicity is shown for the current quark region as function of Q^2, in the Breit frame, for e^+e^- data and HERA data.[106] Since the current quark has the momentum $Q/2$, Q is the natural scaling variable in the Breit system. The HERA data are scaled up by a factor 2 to account for the two jets in the electron positron annihilation data. The data show good agreement with the e^+e^- data. In Fig. 46b, the shape of the multiplicity is presented in KNO form: the distribution of events multiplied by $\langle n\rangle$ is plotted in the variable $z = n/\langle n\rangle$, allowing a comparison of distributions from different kinematical regions. The KNO spectra are found to be approximately independent of Q^2. Finally we show in Fig. 47 the fragmentation function for HERA and e^+e^- data. The hadronic fragmentation variable x_p is defined as the fraction of the QPM quark momentum carried by the hadron. In

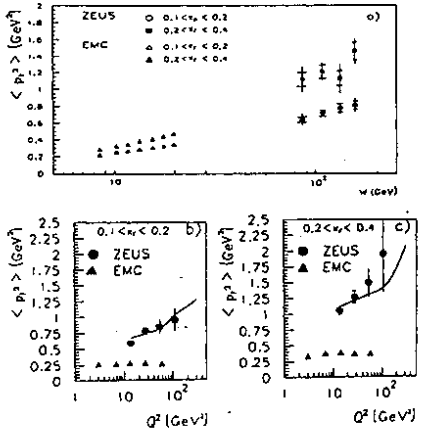

Figure 45: Preliminary ZEUS data showing the rise in track $\langle p_T^2 \rangle$ in the hadronic centre of mass frame as function of W and Q^2 for different x_P intervals.

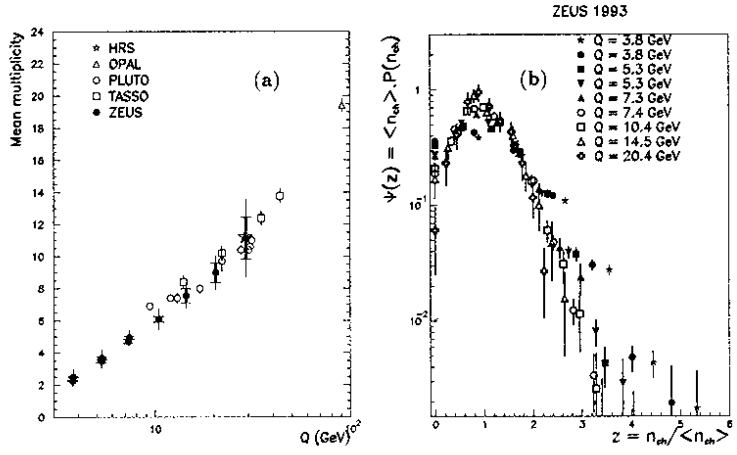

Figure 46: (a) ZEUS data on mean charged multiplicity in the Breit current region as a function of Q. The ZEUS data are scaled up by a factor 2. The data are corrected for K^0 and Λ decays. The fat error bars are statistical errors, the thin ones statistical and systematic errors added in quadrature. Also shown are e^+e^- data from PETRA, PEP and LEP. (b) The KNO distribution for ZEUS data of the current region in the Breit frame, at different values of Q. Only statistical errors are shown.

the Breit frame we have $x_p = 2p_h/Q$. It is common to show these particle spectra as function of $\ln(1/x_p)$, where Modified Leading Log QCD Approximations (MLLA) coupled with the assumption of Local Parton Hadron Duality (LPHD) predict a Gaussian shape for the data, confirmed by the data in Fig. 47a for seven Q^2 intervals. The area is a measure of the average multiplicity. The peak of the distribution is moving to larger $\ln(1/x_p)$ values with increasing

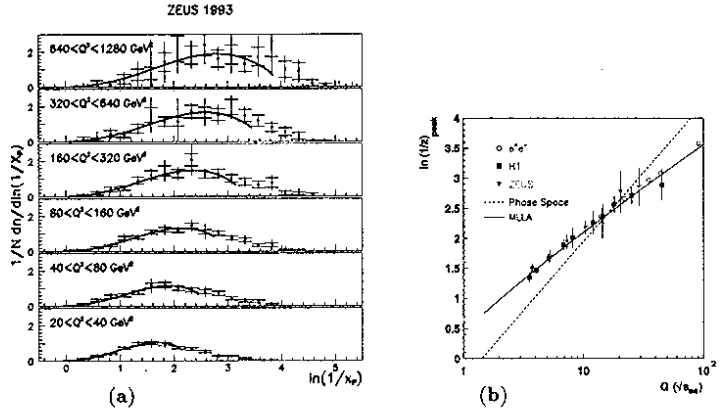

Figure 47: (a) Charged particle spectra $\ln(1/x_p)$ with $x_p = 2p_h/Q$ in the Breit current region from ZEUS, forming the "hump backed" plateau. The inner error bars are statistical only. (b) Peak position of the $\ln 1/x_p$ distributions as a function of Q. The ZEUS and H1 data (preliminary; statistical errors only) are compared with data from e^+e^- annihilation.

Q^2. This is more clearly demonstrated in Fig. 47b, where the ep data are also compared with the e^+e^- data, showing again excellent agreement. The data show a slope different from the expectation of a phase space model. This deviation is sometimes claimed to be due to colour coherence effects, resulting from interference in gluon emission.

In summary distributions concerning quark fragmentation in ep and e^+e^- data show a very good agreement. Within the sensitivity of the present data, the performed studies show no evidence that quarks kicked out of the proton and quarks created in e^+e^- annihilation are different objects, or behave differently.

5.5 The Hadronic Final State: Jets

Already with the data collected in 1992 multi-jet events have been observed and measured[107,108] in DIS events. With the 1993 data we are able to use the jet rates for quantitative measurements. Here we will show:

- the jet rates at the parton level
- extraction of the gluon distribution in the proton from jets
- extraction of the strong coupling constant α_s
- demonstration of the angular asymmetry.

Jets are experimentally defined using a jet algorithm. So far mainly the *JADE* algorithm[109] and the *cone* algorithm[36] have been used for jet studies at HERA. For the JADE algorithm

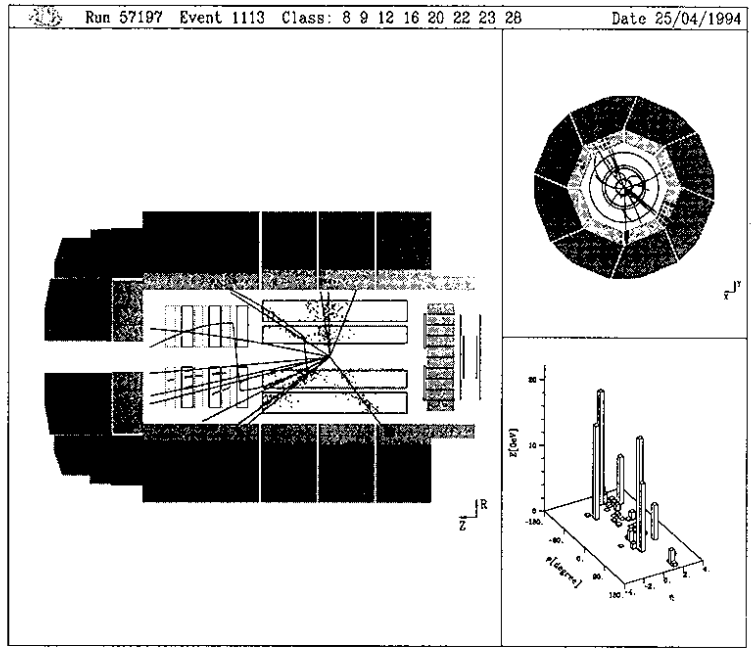

Figure 48: Example of a (2+1) jet deep inelastic scattering event in the H1 detector.

resolution (y_{cut}) dependent jet multiplicities are determined by calculating scaled invariant masses y_{ij} defined as

$$y_{ij} = \frac{m_{ij}^2}{W^2}, \qquad \text{with} \qquad m_{ij}^2 = 2E_iE_j(1-\cos\theta_{ij}),$$

that is, neglecting the masses of clusters i and j. The invariant mass of the hadronic system W is chosen as the scale. Clustering is repeated until y_{ij} is above the jet resolution parameter y_{cut} for all clusters. The jet resolution parameter is necessary both for the assignment of final states with soft and nearly collinear partons to a given cross section class and for the regularization of infinities in the theoretical expressions. The remaining clusters are counted as jets. The loss of a large fraction of the proton remnant jet in the beampipe is compensated in the jet algorithm by introducing a pseudoparticle carrying the missing longitudinal momentum of the event. The cone algorithm on the other hand searches for cones with an $E_T > E_T^{min}$ in the azimuthal φ angle and pseudo-rapidity η space, within an area with fixed radius $R = \sqrt{\Delta\varphi^2 + \Delta\eta^2}$. The cone radius is chosen to be $R = 1$, the same as for the photoproduction analyses discussed in section 4.

At HERA we use the following terminology. In the quark parton model (QPM), one jet arises from the struck quark scattering into the detector, while the proton remnant leads to another jet. This is called a "1+1" jet event configuration. The jet of the proton remnant is generally lost in the beampipe. Due to QCD processes to $O(\alpha_s)$, such as gluon radiation in

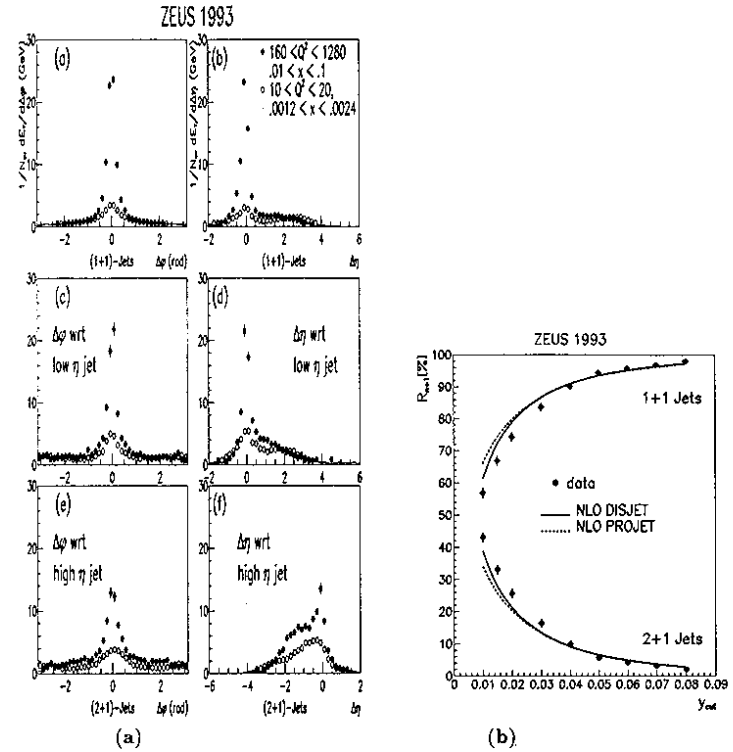

(a) (b)

Figure 49: (a) Jet profiles from ZEUS for 1+1 and 2+1 jet events. Plotted is the energy flow transverse to the beam axis around the jet axis in azimuth φ and pseudo-rapidity $\eta = -\ln\tan\theta/2$, where θ is the angle of the energy deposition w.r.t to the proton beam axis. The distance in pseudo-rapidity $\Delta\eta$ is measured such that the proton direction is towards the right. The data from a high and a low Q^2 sample are shown. (b) The 1+1 and 2+1 jet rates R_j from ZEUS as a function of y_c. Calculations up to next to leading order from the programs DISJET and PROJET are compared to the measurements.

the initial or final state or photon-gluon fusion, a further jet can appear. These events are termed 2+1 jet events. Fig. 48 shows a 2+1 jet event in the H1 detector. Two well separated jets are visible in the detector and in the energy flow plot, with a possible third jet close to the proton remnant direction.

Fig. 49 shows jet profiles and jet rates for 1+1 and 2+1 events measured by the ZEUS experiment using the JADE algorithm. The jet rates are presented as function of the cut-off parameter y_{cut} and corrected from observed jets in the detector to jets at the parton level.[110] These corrections were made with the MEPS model. The results are compared with NLO calculations using the programs PROJET[111] and DISJET.[112] The calculations agree rather well with the measurements.

H1 used the measured 1+1 and 2+1 jet rates to extract values of α_s as function of Q^2, identified with the scale in the renormalization group equations (RGE). This technique has been exploited at e^+e^- colliders before and uses the fact that the hard emission of a gluon in

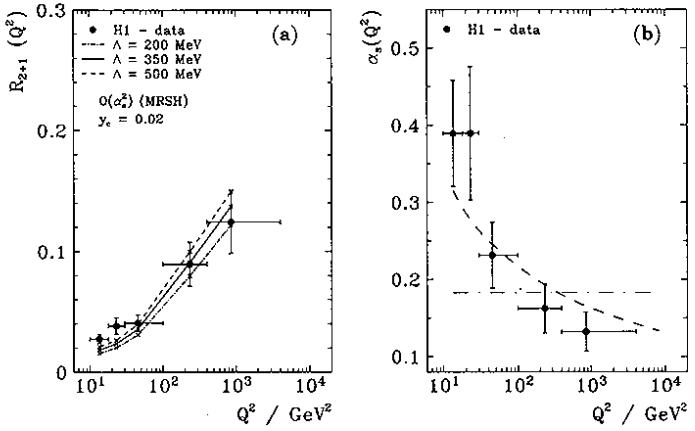

Figure 50: (a) Comparison of jet rates at the parton level from H1 data to QCD in next to leading order using PROJET, for various Λ values and the MRSH parton density. The vertical error bars correspond to the statistical error of the data and the correction factors. (b) The measured value of α_s as a function of Q^2. The fit to the RGE prediction (falling dashed curve) is shown. For comparison, the fit to the ansatz of constant α_s is also included.

e.g. the QCDC diagram is suppressed by a factor α_s w.r.t. the QPM diagram. It is however not a priori clear that the same technique can be used in ep collisions due to the presence of strongly interacting partons in the initial state. Problems arising in this respect are multiple gluon emission, particularly in the initial state, and the limited precision on the knowledge of parton densities in the proton. The measurement is performed as follows.[113] In NLO QCD the cross sections for 1+1 and 2+1 jet events are given by

$$\sigma_{1+1}(Q^2, y_{cut}) = A_{1+1,0}(Q^2) + \alpha_s(Q^2) A_{1+1,1}(Q^2, y_{cut}) \tag{13}$$

and

$$\sigma_{2+1}(Q^2, y_{cut}) = \alpha_s(Q^2) A_{2+1,1}(Q^2, y_{cut}) + \alpha_s^2(Q^2) A_{2+1,2}(Q^2, y_{cut}). \tag{14}$$

The terms $A_{i,j}$ contain the hard scattering matrix elements (without the strong coupling constant) and the parton densities of the incoming proton. The first index stands for the jet multiplicity as defined above. The second index indicates the order α_s^j to which the process is calculated. The parameter y_{cut} is the jet resolution parameter, chosen to be 0.02 for this analysis. Using eqns. (13) and (14) the ratio of the 2+1 jets to the full cross section (which consists almost exclusively of 2+1 and 1+1 jet events) can also be expressed as a power series in α_s which is correct to $\mathcal{O}(\alpha_s^2)$. This ratio, corrected to the parton level using the MEPS model, can be measured at different values of the scale Q^2, as shown in Fig. 50a. In Fig. 50b the measured ratios are converted to values of α_s. The running of α_s with Q^2 is clearly seen. It has however turned out that the α_s values calculated this way at low Q^2 are rather sensitive to the QCD model used to correct the observed jets at the detector level, towards the parton level and to a lesser extend both to the cuts used to suppress higher order contributions (beyond NLO) and the limited knowledge of parton distributions in the proton. Therefore for

a quantitative determination of α_s only the two highest Q^2 points were taken. A fit of those points to the RGE and using the MRSH parton distributions leads to the value

$$\alpha_s(M_z^2) \;=\; 0.123 \pm 0.018\,.$$

The statistical and systematical errors are added in quadrature. The largest contributions to the systematic errors are given by the dependence of the correction factors on the QCD model to correct to the parton level, and the current 5% uncertainty of the hadronic energy scale of the LAr calorimeter in H1. The value can be compared with $\alpha_s = 0.119 \pm 0.010$ obtained from the LEP experiments using the same observable in NLO,[114] and with $\alpha_s(M_Z^2) = 0.117 \pm 0.005$ from the world average.[56] The agreement between the α_s values determined from the same observable in deep inelastic ep scattering and e^+e^- annihilation again demonstrates the coherence and consistency of the underlying QCD picture.

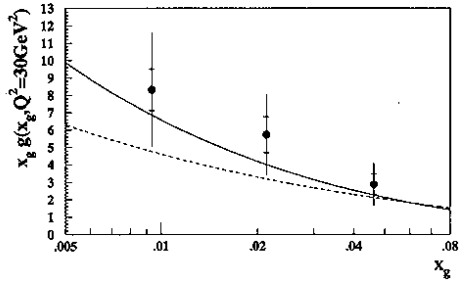

Figure 51: The preliminary gluon distribution extracted from the H1 2-jet data, as a function of x at $Q^2 = 30$ GeV^2.

Inspecting Fig. 43, shows that the gluon distribution of the proton enters the interaction at the Born level for the PGF diagram. Just as for photoproduction events, one can attempt to measure the gluon distribution in LO by trying to isolate this PGF diagram contribution. Heavy flavour tagging would be a natural choice, but the present statistics does not allow such measurement at this stage. Instead a region was selected were the 2+1 jet events are dominantly produced by the PGF mechanism, and the remaining background was estimated by QCD jet cross section programs and subtracted. Jets with $E_T > 3.5$ GeV are selected in the angular range $10° < \Theta_{jet} < 150°$, using the cone algorithm. The invariant mass of the 2-jet system has to be larger than 10 GeV, and the pseudo-rapidity difference between the two jets is required to be less than two units. The QCDC background prediction of the program PROJET was used, folded with the experimental acceptance calculated with Monte Carlo studies using the MEPS model. The resulting 2+1 event rates were corrected to cross sections. The gluon distribution is extracted at a $Q^2 = 30$ GeV^2, by a bin by bin reweighting of the gluon distribution used in PROJET, using the measured and predicted PGF cross section. The scale of the gluon extraction was taken to be the p_T of the hard scattering process. The preliminary result is shown in Fig. 51 and is compatible with the gluon distribution determined from scaling violations of the structure function data, discussed in section 5.3. A considerable rise is seen for decreasing x. The large systematical errors result mainly from present differences found when different jet algorithms are used, and are expected to be improved in the near future.

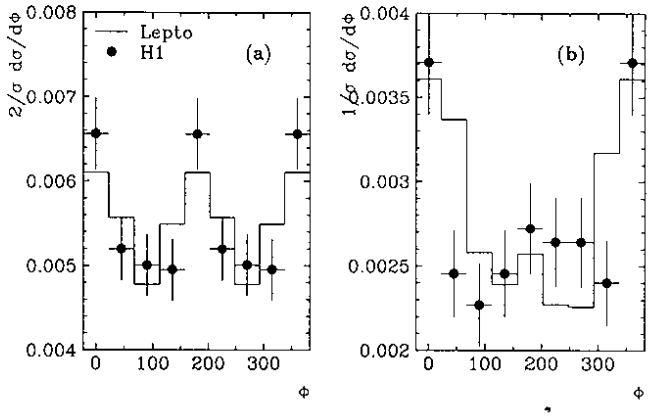

Figure 52: Preliminary azimuthal distribution[116] of the 2-jet plane with respect to the electron scattering plane in the hadronic centre of mass frame, using the H1 data; (a) including both jets of each event; (b) selecting only the most energetic jet. Only statistical errors are given.

A further study examines the azimuthal asymmetry of the 2-jet plane with respect to the electron scattering plane in the centre of mass frame. QCD predicts that QCDC and PGF diagrams exhibit an asymmetry in the distribution of the azimuthal angle between these planes.[115] Preliminary results are shown in Fig. 52 for jets with an $E_T > 4$ GeV (in hadronic CMS).[116] The MEPS Monte Carlo follows the general trend of the data. Future studies will increase the precision of the current methods and exploit new techniques for the extraction of the PGF component from the data.

5.6 BFKL and DGLAP Evolution Revisited

We turn back to the question of DGLAP and BFKL QCD dynamics at low x, introduced in the discussion on the structure function F_2. For events at low x, hadron production in the region between the current jet and the proton remnant is of particular interest, since it is expected to be sensitive to effects of BFKL dynamics. Indeed initial state QCD radiation is a testing ground for the BFKL and DGLAP hypothesis. This is depicted in Fig. 53, showing that before the struck quark is hit by the virtual photon, it may emit a number of gluons. The figure indicates the proton momentum fractions x_i and transverse momenta k_{Ti} (virtualities) of the quarks and gluons which are emitted. In the leading order DGLAP scheme the cascade follows a strong ordering in transverse momentum $k^2_{Tn} \gg k^2_{Tn-1} \gg ... \gg k^2_{T1}$, while there is only a soft (kinematical) ordering for the fractional momentum $x_n < x_{n-1} < ... < x_1$. For the BFKL scheme the cascade follows a strong ordering in fractional momentum $x_n \ll x_{n-1} \ll ... \ll x_1$, while there is no ordering in transverse momentum. In fact the transverse momentum undergoes a random walk type of diffusion: the k_{Ti} value is not to far from the k_{Ti-1} value, but it can be both larger or smaller.[117] Therefore BFKL evolution is expected to produce more E_T in the region between the current and remnant for low x events, compared

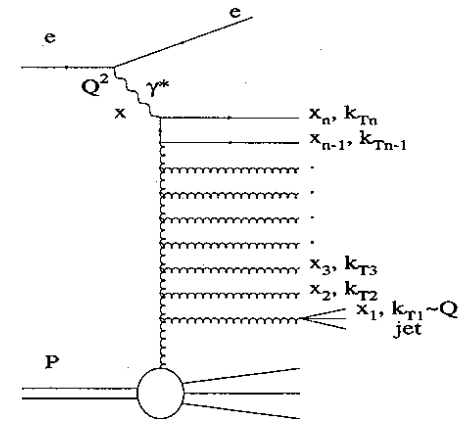

Figure 53: Parton evolution in the ladder approximation. The selection of forward jets in DIS events is illustrated.

to DGLAP evolution. Hence, the E_T flow measurement probes the evolution dynamics for small x processes.

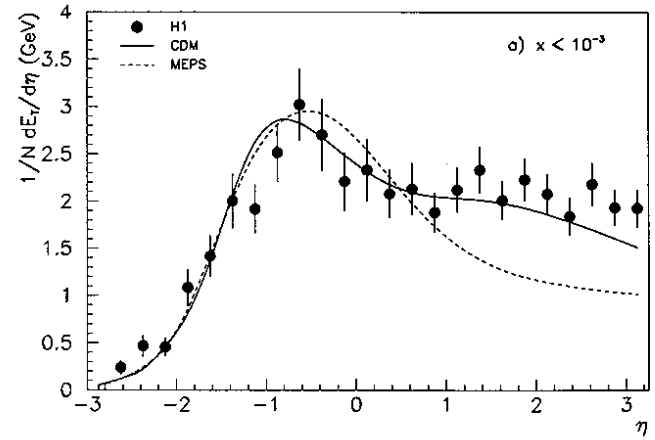

Figure 54: Transverse energy flow E_T in the laboratory system as a function of the pseudo-rapidity η with $x < 10^{-3}$, measured by H1. The proton direction is to the right. The error bars contain the statistical and systematic errors added in quadrature, except for an overall 6% energy scale uncertainty.

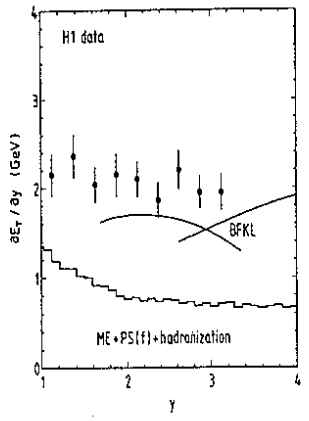

Figure 55: The same data as Fig. 54 (η is termed y here). The continuous curve shows the BFKL predictions at the parton level of $x = 5.7 \cdot 10^{-4}$ and $Q^2 = 15$ GeV^2, which correspond to the average values of the data sample. The histogram is the MEPS Monte Carlo estimate, including hadronization.

The transverse energy flow has been studied by H1.[104] Fig. 54 shows the transverse energy flow corrected for detector effects as a function of the pseudo-rapidity η, in the laboratory system for values of $x < 10^{-3}$. Away from the current quark the data show a plateau of $E_T \approx 2$ GeV per unit of rapidity. The CDM and LEPTO model predictions are compared to the data. While the CDM model describes the data reasonably well, the DGLAP based MEPS model fails to describe the plateau away from the current quark and clearly undershoots the data in this region. Recently numerical calculations predicting the transverse energy flow at the parton level have been performed[118] both for DGLAP and BFKL scenarios. The result for the BFKL at the parton level is shown in Fig. 55, for $\langle x \rangle = 5.7 \cdot 10^{-4}$ and $\langle Q^2 \rangle = 15$ GeV^2. The BFKL calculation predicts a fairly flat plateau at low x with $E_T \approx 2$ GeV per unit of rapidity. The E_T is considerably lower for predictions based on DGLAP parton showering dynamics. The analytic DGLAP calculation yields about 0.6 GeV E_T at the parton level. The effect of the additional E_T contribution due to fragmentation effects is shown in Fig. 55, by the histogram, using the LEPTO model. The discrepancy with the data remains large.

x range	data	MEPS MRSD0(−)'	CDM
$2 \cdot 10^{-4} - 2 \cdot 10^{-3}$	$128 \pm 12 \pm 26$	69 (53)	32
$2 \cdot 10^{-4} - 1 \cdot 10^{-3}$	$85 \pm 9 \pm 17$	37 (27)	21
$1 \cdot 10^{-3} - 2 \cdot 10^{-3}$	$43 \pm 7 \pm 9$	32 (26)	11

Table 3: Number of DIS events with a selected forward jet compared to Monte Carlo predictions. (H1 preliminary data.)

Another possible footprint of the BFKL dynamics is the rate of jets produced in a DIS event with the following characteristics.[99,119,120] The k_{Tj}^2 of the selected jet should be close to Q^2 and the ratio of the momentum fraction of the jet and the Bjorken-x, x_j/x, should be as large as possible. The process is shown in Fig. 53. The rate of those jets is sensitive to the type of evolution dynamics since for the DGLAP case, due to the strong ordering of k_T,

there is little room for the evolution in Q^2 if $k_{Tj}^2 \approx Q^2$ while for the BFKL ansatz the gluon radiation is governed by the ratio x_j/x. Hence for a low x event the phase space for emission of a high x_j jet is large. Therefore we expected the jet rate to be higher for the BFKL than for the DGLAP scenario. In a sample of DIS events with $Q^2 \approx 20$ GeV^2 and $2 \cdot 10^{-4} < x < 2 \cdot 10^{-3}$ we have counted the jets with $x_j > 0.05$ and $0.5 < k_{Tj}^2/Q^2 < 6$. The resulting number of events, corrected for background contribution, is given in Table 3 and compared to expectations of the MEPS and CDM models simulated in our detector. These predictions were found not to depend significantly on the parametrization of the structure function and generally tend to be below the observations in the data. The size of the errors do not allow yet a firm conclusion. We can however notice that the rate of jets rises with decreasing x. This is expected from BFKL dynamics as an numerical calculation[120] has demonstrated. At the parton level, with the same cuts as for this analysis, the BFKL evolution yields 75 and 36 events for the low and high x bin respectively. Without BFKL evolution, i.e. only taking into account the box diagram, the calculation expects 25 and 20 events respectively. So the data tend to follow the BFKL evolution expectation, but a correction from the measured jet rates to the parton level and more statistics will be necessary before we can make quantitative comparisons with the calculations.

5.7 Deep Inelastic Scattering Events with a Rapidity Gap

In analysing the data taken in 1992, the ZEUS and H1 collaborations observed a peculiar class of DIS events[122,123] which, unlike the majority of the events, had no energy flow in a region around the beampipe in the forward proton direction. Some activity is expected in the forward direction for "conventional" DIS processes (Fig. 1), due to the colour connection between the struck quark and the proton remnant. However, these events show a region with no activity – a gap – in the forward detector region. An example of such an event is shown in Fig. 56, which can be compared to a conventional DIS event shown in Fig. 34. In chapter 4 a class of events with similar characteristics was found in photoproduction interactions and was interpreted as diffractive scattering. An indicative variable to tag diffractive events is the η_{max} of the event, as introduced in section 4.4. The η_{max} distribution for DIS events is shown in Fig. 57 for the ZEUS experiment and can be compared with a corresponding distribution in γp interactions in Fig. 26. A similar behaviour is seen in both distributions. The rate of DIS events with a small η_{max} (i.e. large gap) is substantially above the expectations of standard DIS models,[101] showing these events are not included in the conventional DIS Monte Carlo programs. It may be tentatively assumed that the DIS events which exhibit a rapidity gap are connected with diffractive scattering, in a way similar as for photoproduction.

In fact, it was anticipated that the HERA collider should provide a rather unique possibility to study diffractive dissociation at short distances[124] and that the rapidity gap would be a powerful criterion to eliminate conventional deep inelastic background.[125] An example of a model to explain these events in terms of diffraction is shown Fig. 58b, compared to the conventional DIS process in Fig. 58a. The model assumes that the photon scatters off the partonic content of an object in, or emitted by, the proton, called the Pomeron (introduced in sections 4.2 and 4.4). The Pomeron is not colour connected with the proton and hence there is a region between the proton remnant and the hadronic system probed by the virtual photon without colour flow. This can lead to an observable gap in the detector, and such models can account for the observed η_{max} distribution, as is shown in Fig. 57. These processes are implemented in the Monte Carlo programs POMPYT[53] and RAPGAP.[121] Note however that the mere observation of events with gaps does not unambiguously prove that these events are indeed of a diffractive nature, including Pomeron exchange. In fact other colourless exchange, such as meson exchange, also leads to events with gaps.

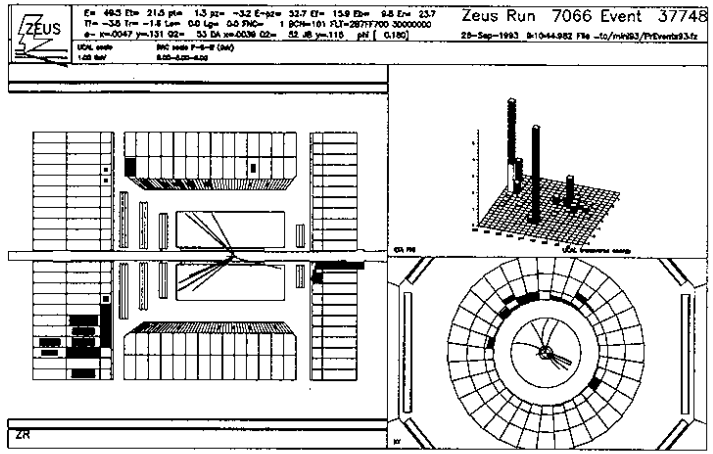

Figure 56: Display of a deep inelastic event with a large rapidity gap observed in the ZEUS detector. There is no energy deposited in a large region of rapidity in the proton direction, to the left in the figure.

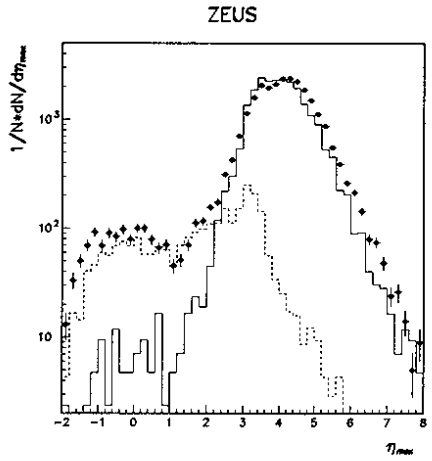

Figure 57: The distribution of the variable η_{max}, the rapidity of the most forward energy deposit above 400 MeV in the calorimeter. The solid circles are ZEUS data points. The full histogram is the CDM Monte Carlo, and the dashed histogram is the POMPYT Monte Carlo.

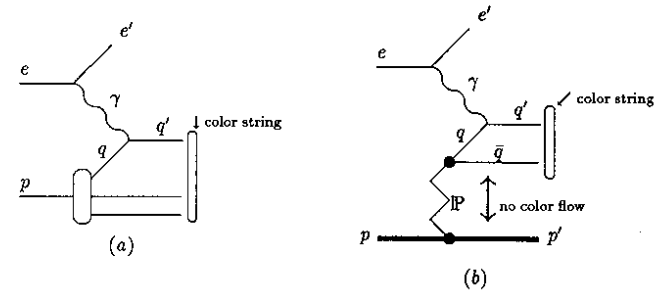

Figure 58: Model for the hadronic final state in usual deep inelastic scattering (**a**) and diffractive deep inelastic scattering (**b**).

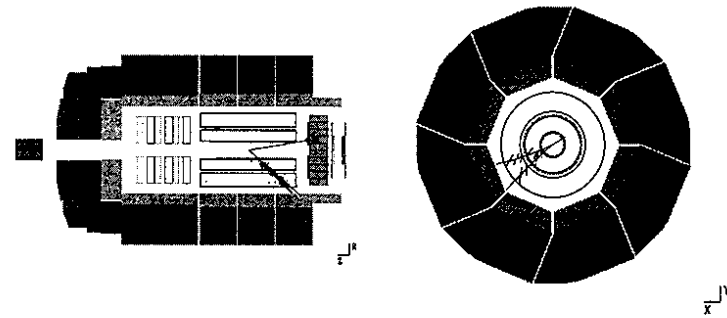

Figure 59: Example of an exclusive $\gamma^* \rightarrow \rho^0 p$ event candidate in the H1 detectór. Apart from the scattered electron only two charged particles are detected.

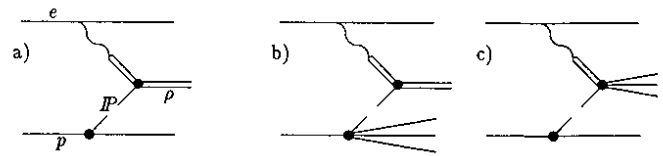

Figure 60: Diagrams which illustrate the VDM description of the rapidity gap events: (a) $\rho^0(770)$ production via elastic VDM; (b) VDM $\rho^0(770)$ production with soft dissociation of the proton; (c) VDM interaction followed by soft dissociation of the vector meson. The double dissociation diagram is not shown.

In the case that diffraction represents the underlying dynamics of the rapidity gap events then these events can be used to probe the partonic content of the Pomeron. These events were most likely also present in the data of fixed target DIS experiments (in fact exclusive $\rho^0(770)$ production has been reported; see below), but due to the large centre of mass energy and the capability to detect the hadronic final state in H1 and ZEUS these events can be isolated at HERA with a topological selection, such as the η_{max} selection. Hence the structure of the Pomeron can be measured and questions on the shape of the parton distributions and on whether quarks or gluons dominate the structure of the Pomeron (see section 4.4) can be studied. So far our knowledge of the structure of the Pomeron is essentially based on the results of the UA8 $p\bar{p}$ experiment.[52]

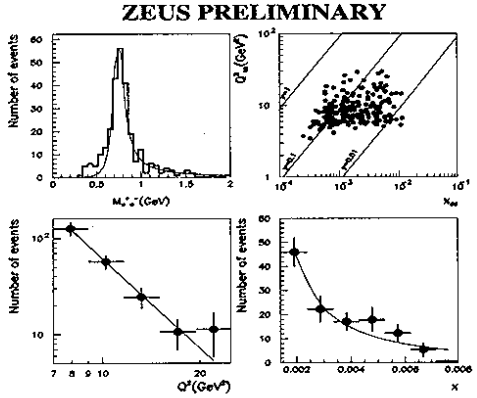

Figure 61: ZEUS data: (a) Mass ($\pi^+\pi^-$) spectrum of particle pairs with a Breit-Wigner fit to the data; (b) Q^2 versus x for ρ^0 events; (c) corrected ep Q^2 distribution for ρ^0 events. The line is an exponential fit to the data; (d) corrected ep x distributions for ρ^0 events. The curve is a $x^{-1.6}$ functional form.

We will argue below that such a mechanism of deep inelastic scattering on a Pomeron is indeed compatible with many of our observations, but other processes are likely to be needed to give a full description of these events. This results from the observation of events which have, apart from the scattered electron, only two charged particles in the detector (Fig. 59). The invariant mass of these particle pairs, shown in Fig. 61, reveals a clear $\rho^0(770)$ vector meson peak. Thus, there is an exclusive vector meson component in the data which amounts to about 15% of all diffractive events. A possible interaction mechanism for this process is a vector meson dominance contribution (VDM), where the photon fluctuates into a vector meson similar to photoproduction processes. Hence exclusive leptoproduction of vector mesons can be elastic (Fig. 60a) or followed by soft dissociation of the proton (Fig. 60b). H1 has shown that the shape of the low η_{max} ($\eta_{max} < 1.5$) distribution can be also reproduced by a VDM motivated simulation.[126] The ZEUS collaboration has studied the exclusive production of vector mesons in the range $7 < Q^2 < 25$ GeV^2 and $0.01 < y < 0.25$. The preliminary data on the x and Q^2 dependence is given in Fig. 61 corrected for detector acceptance and resolution. After fitting the Q^2 distribution to an exponential form, the power of the Q dependence obtained was $-8.2 \pm 1.4(\text{stat})^{+1.4}_{-0.3}(\text{syst})$. The x distribution falls off with increasing x and is reasonably described by the form $x^{-1.6}$. The cross section in the range $7 < Q^2 < 10$ GeV^2 for $\gamma^* \to \rho^0 p$ is $123 \pm 15(\text{stat}) \pm 39(\text{syst})$ nb, to be compared with a prediction of 165 nb.[127] The production of vector mesons at high Q^2 has already been observed in fixed target experiments.[128] In Fig. 62 the preliminary ZEUS results are compared with these data. At $Q^2 = 8.6$ GeV^2, the ZEUS collaboration measures a $\gamma^* p \to \rho^0 p$ cross section which is about 3

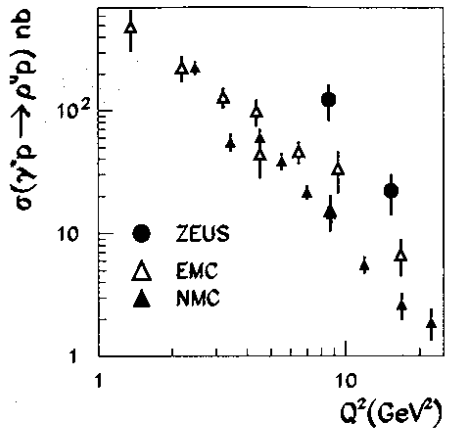

Figure 62: Preliminary ρ^0 cross section for virtual photoproduction as a function of Q^2. The mean $\gamma^* p$ centre of mass energy W is about 10 GeV for the EMC/NMC data points and 100 GeV for the ZEUS data points.

times larger than those of EMC[129] and NMC[130] at the same Q^2 value. Note that both HERA experiments cannot observe the hadronic system on the proton side, since it disappears in the beampipe. This part has been estimated in Monte Carlo studies by the ZEUS collaboration, and could be as large as 15%. Proton tagging devices are being commissioned by both HERA experiments, which will allow in future to select samples of elastic events. The elastic production of $\rho^0(770)$ will remain a hot topic at HERA, since it has been argued that it can be used to probe BFKL dynamics.[131]

A sample of rapidity gap events is defined by the cut $\eta_{max} < 1.8(< 1.5)$ for H1 (ZEUS). The total observed fraction of rapidity gap events in the DIS sample amounts to about 6(5)%. However, the cut on η_{max} has selected only part of the diffractive events, namely those events were the rapidity gap is visible in the detector. After an acceptance correction which depend on the models used to describe the events, the H1 and ZEUS experiments get an estimate of the corrected fraction of diffractive events in the DIS sample which varies between 10 and 15 %.[26,126]

The rapidity gap events at HERA selected with the η_{max} cut are distributed over the entire Q^2 and x range covered by the sample of detected DIS events. Fig. 63 shows the ratio of rapidity gap events to all DIS events as a function of Q^2 in narrow x regions as measured by the ZEUS collaboration. The data are restricted to values of $W > 140$ GeV where Monte Carlo calculations show that the acceptance is flat. It is striking that this ratio has no significant dependence on Q^2, which is consistent with a leading twist QCD production mechanism. The similarity in the Q^2 dependence of rapidity gap events with normal DIS events is as expected in models based on partonic structure of the pomeron. However, given the uncertainties in the Q^2 dependence of VDM models for highly virtual photons it is possible to reproduce the ratio observed in Fig. 63 in a VDM-like picture[126] as well.

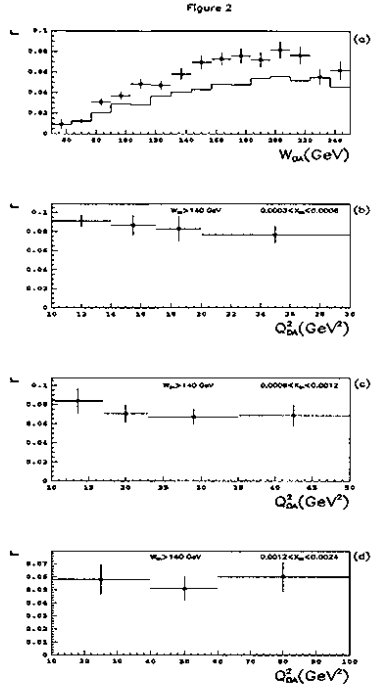

Figure 63: The ratio of DIS events with a large forward rapidity gap ($\eta_{max} < 1.5$) to all DIS events measured by ZEUS, not corrected for detector effects, as function of (a) the total hadronic energy W and (b-d) the Q^2 of the interaction, for different x intervals. The variables W and Q^2 are calculated with the double angle method. The histogram in (a) shows the detector acceptance as function of W. Figs. (b-d) are shown for $W > 140$ GeV.

Next we investigate the contribution of diffractive events to the structure function F_2. A variable $x_{\mathbf{P}/p}$ is defined which is the momentum fraction of the proton carried by the Pomeron. In the H1 analysis the cut on $\eta_{max} < 1.8$ selects mainly events with $x_{\mathbf{P}/p} < 0.01$, as shown in Fig. 64a and hence with $x < 0.01$ because the variables x and $x_{\mathbf{P}/p}$ are related by :

$$x = x_{\mathbf{P}/p} \frac{Q^2}{Q^2 + M_X^2}. \tag{15}$$

Here M_X is the invariant mass of the final state hadronic system observed in the detector. In the following the data are corrected for acceptance to the region $x_{\mathbf{P}/p} < 0.01$ using various models, the difference of which is taken into account for the systematic errors. Thus we define diffraction as the sample of events for which $x_{\mathbf{P}/p} < 0.01$. Note that Regge analyses performed on hadron-hadron collisions at low energies suggest that for $x_{\mathbf{P}/p} < 0.1$ Pomeron exchange is dominant whereas for larger values the contribution from other Reggeons is not negligible.[132] Hence we have some justification to call these events diffractive production, but there is no proof at this stage.

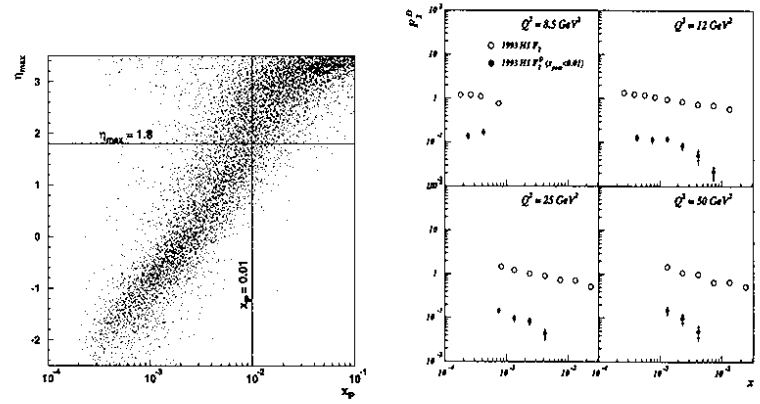

Figure 64: (a) Correlation between η_{max} and $x_{\mathbf{P}/p}$ ($x_{\mathbf{P}}$ in the figure) from Monte Carlo studies by the H1 collaboration. (b) The H1 results on the diffractive contribution F_2^D to F_2 for $x_{\mathbf{P}/p} < 0.01$.

Following[53] one can define $F_2^{D(4)}$:

$$\frac{d\sigma(ep \to epX)}{dx_{\mathbf{P}/p} dt dx dQ^2} = \frac{2\pi\alpha^2}{Q^4 x} \left(2\,(1-y) \;+\; y^2\right) F_2^{D(4)}(x, Q^2, x_{\mathbf{P}/p}, t) \tag{16}$$

as the unintegrated diffractive contribution to the structure function. We adopt the notation $F^{D(n)}$ for the diffractive contribution to the structure function, where n presents the number of variables. The contribution of the longitudinal structure function has been neglected in eqn. 16. Here t is the square momentum transfer between the incident and the outgoing proton or proton dissociative system, a quantity we cannot measure with sufficient resolution with the present detector setup. The integral of $F_2^{D(4)}$ over $x_{\mathbf{P}/p}$ and t gives the contribution from the diffractive events to the structure function $F_2(x, Q^2)$, which we call simply F_2^D :

$$F_2^D(x, Q^2) = \int_{10^{-4}}^{10^{-2}} \int_{t_{min}}^{\infty} F_2^{D(4)}(x, Q^2, x_{\mathbf{P}/p}, t) dx_{\mathbf{P}/p} dt. \tag{17}$$

The resulting diffractive part of the structure function $F_2^D(x, Q^2)$, defined for $x_{\mathbf{P}/p} < 0.01$ is shown together with the total inclusive structure function $F_2(x, Q^2)$ in Fig. 64b. For $x < 10^{-3}$, $F_2^D(x, Q^2)$ contributes about 10% to $F_2(x, Q^2)$. Clearly the diffractive events cannot explain the rise of F_2 at low x. The x dependence of F_2^D as x approaches 10^{-2} has to be taken with caution, since the cut on $x_{\mathbf{P}/p} < 0.01$ forces F_2^D to zero at $x = 10^{-2}$. Analysing F_2^D as a function of Q^2 reveals that there are no significant scaling violations observable, within the present experimental errors.[70]

An important characteristic of many models for diffractive hard scattering is the factorization of $F_2^{D(4)}$ into a Pomeron flux term and a Pomeron structure function :

$$F_2^{D(4)}(x, Q^2, x_{\mathbf{P}/p}, t) = f(x_{\mathbf{P}/p}, t) F_2^{\mathbf{P}/p}(\beta, Q^2) \tag{18}$$

where $\beta = \frac{x}{x_{\mathbf{P}/p}}$ is the fraction $x_{q/\mathbf{P}}$ of the $\mathbb{P}$ momentum carried by the quark interacting with the virtual boson, and $f(x_{\mathbf{P}/p}, t)$ is the Pomeron flux factor. If the factorization is true, then

$$F_2^{D(3)} = \int_{t_{min}}^{\infty} F_2^{D(4)} dt \tag{19}$$

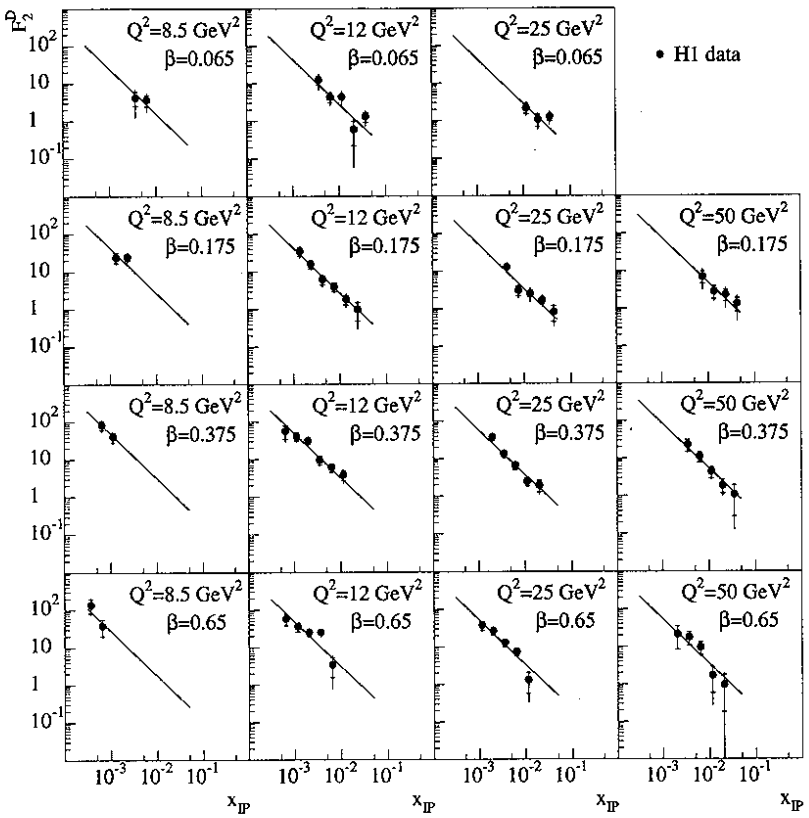

Figure 65: The diffractive contribution $F_2^{D(3)}(\beta, Q^2, x_{I\!P/p})$ to the proton structure function F_2 as a function of $x_{I\!P/p}$ ($x_{I\!P}$ in the figure) for different β and Q^2; the inner error bar is the statistical error; the full error shows the statistical and systematic error added in quadrature; superimposed is the result of the fit establishing a factorisable dependence of the form $\propto x_{I\!P/p}^{-n}$ (see text). Note that an overall systematic error of 8% is not included.

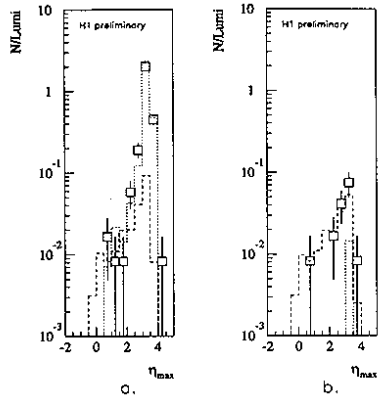

Figure 66: η_{max} distribution of (a) all (2+1) jet events and (b) those satisfying the forward detector selection, described in the text obtained by the H1 collaboration (preliminary). The dotted line shows the prediction from the deep inelastic scattering Monte Carlo[100] and the dashed line shows the prediction from hard diffractive scattering.[121]

should have the same $x_{I\!P/p}$ behaviour independent of β and Q^2.

In a dedicated analysis, the H1 collaboration has replaced the η_{max} selection by a set of cuts based on forward detectors. These detectors are mainly sensitive to secondaries produced by forward going hadrons interacting in collimators close to the proton beam axis.[133] The detectors are sensitive to particles produced in the pseudo-rapidity region $3.6 < \eta < 6.6$. The advantage is that this selection gives access to higher values of $x_{I\!P/p} < 0.1$. Hence larger values of M_x can be reached (see eqn. 15), and correspondingly smaller values of β are accessible. The resulting diffractive sample has been divided into four bins of Q^2 ($Q^2 = 8.5, 12, 25, 50$ GeV^2) times four bins of β ($\beta = 0.065, 0.175, 0.375, 0.65$). The results are shown[133] in Fig. 65. In all the bins the dependence of $F_2^{D(3)}(x, Q^2, x_{I\!P/p})$ on $x_{I\!P/p}$ can be fitted by a simple expression:

$$F_2^{D(3)}(x, Q^2, x_{I\!P/p}) = x_{I\!P/p}^{-n} \tilde{F}_2(\beta, Q^2) \tag{20}$$

with

$$n = 1.19 \pm 0.06(\text{stat}) \pm 0.07(\text{syst}). \tag{21}$$

$\tilde{F}_2(\beta, Q^2)$ represents the structure of diffraction. The χ^2/ d.f = 32/46 for the fit. Within the present errors the diffractive cross section is compatible with factorization. Furthermore, in Regge theory for hadronic exchange, the $x_{I\!P}$ dependence of the flux factor is related to the leading Regge trajectory $\alpha(t)$ via $x_{I\!P}^{-[2\alpha(t)-1]}$. Hence the leading trajectory has $\alpha(t) \sim 1.10$, neglecting the presumably small t dependence. The leading trajectory is close to the trajectory of the soft Pomeron, for which $\alpha_0 = 1.08$. This is the first evidence that the rapidity gap events can be interpreted as diffraction! Thus the study of deep inelastic scattering events with a rapidity gap at HERA will allow the study of the structure of diffraction. First results[133] on this topic became recently available.

Finally, we study jet production in diffractive events. High E_T jets are expected if the underlying process of these events is hard scattering of the virtual photon with constituent partons of the Pomeron. ZEUS has analysed the data for jets, using a cone algorithm, requiring a jet to have an E_T larger than 4 GeV. The analysis presented in Fig. 67 shows that in the laboratory frame 15% of the rapidity gap events are of the 1-jet type with a negligible 2-jet production rate. With a lower jet transverse energy cut of 2 GeV, a small 2-jet production

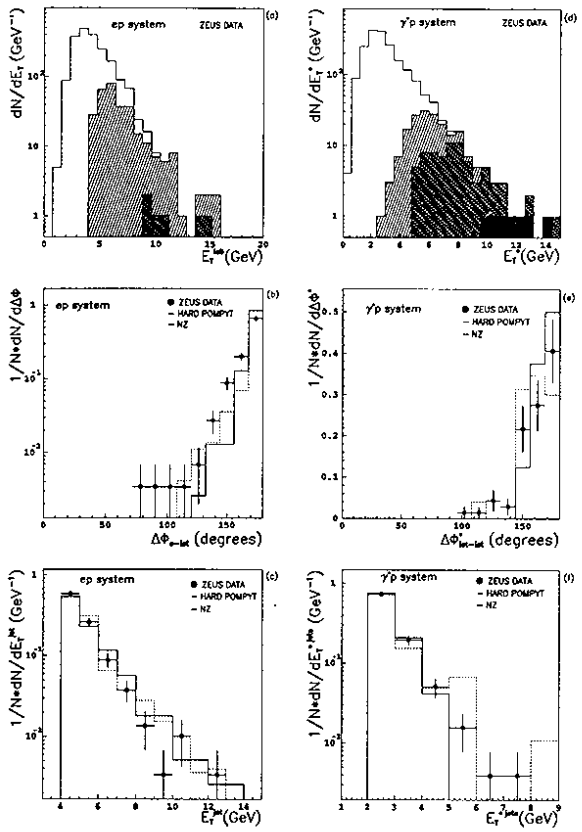

Figure 67: ZEUS data: (a) The distribution of the total hadronic transverse energy seen in the calorimeter, E_T, for DIS events with a large rapidity gap and those with, in addition, ≥ 1 (hashed) and ≥ 2 jets (cross-hashed). A jet is required to have at least 4 GeV transverse energy with respect to the beam direction. (b) The difference in azimuthal angle between the scattered electron and the jet. (c) The jet transverse energy in the laboratory for events in the DIS sample with a large rapidity gap. (d) The total hadronic energy transverse to the virtual photon direction, E_T^*, for DIS events with a large rapidity gap and those with, in addition ≥ 1 (hashed), ≥ 2 (cross-hashed) or 3 jets (solid) in the final state. Here a jet is required to have at least 2 GeV with respect to the virtual photon direction. (e) The difference in azimuthal angle between the the two jets in the $\gamma^* p$ centre-of-mass system (2-jet sample). (f) The distribution of the jet energy transverse to the virtual photon direction for the 1– and 2–jet samples. In figures (b), (c), (e) and (f) the data are shown as black dots with errors and the results from the POMPYT and NZ[51] models as full and dashed histograms respectively.

rate is observed in the $\gamma^* p$ centre of mass frame. A similar analysis is shown in Fig. 66 for the H1 collaboration. Events with 2 jets with $E_T > 3.5$ GeV and an invariant mass of the two jets of $m_{ij} > 10$ GeV have been observed. In the figure the η_{max} distribution is shown for the events with two jets, with and without a rapidity gap requirement, as defined by the forward selection. The data without rapidity gap requirement are well described by the standard DIS Monte Carlo calculation, while the Monte Carlo calculation based on RAPGAP accounts well for the data with a rapidity gap. Since the forward selection gives access to larger M_X values compared to the η_{max} cut analysis, jet production is less suppressed by the available phase space. The observation of two jet events in rapidity gap events is consistent with the assumption that these events are produced in the interaction of the virtual photon with partons in the Pomeron.

The properties of the rapidity gap events in deep inelastic scattering at HERA can be summarized as follows.

- After acceptance correction, the diffractive events represent about 10% of the DIS sample.
- The Q^2 dependence is similar to all DIS events.
- The rapidity gap events do not explain the rise of F_2.
- About 10% of the observed rapidity gap events are exclusive vector mesons with or without proton dissociation.
- In the laboratory frame 15% of the rapidity gap events are of the 1-jet type with $E_T^{jet} \geq 4$ GeV
- The diffractive cross section can be factorized in a Pomeron flux term and a Pomeron structure function.

The interpretation of the events is still subject to discussion and further studies, but the physics potential is clearly very large.

6 Electroweak Measurements

One of the major physics topics conceived at HERA are studies of the electroweak theory. Indeed, the high Q^2 range accessible at HERA enables studies in the region of $Q^2 \simeq M^2_{W,Z^0}$, where W and Z^0 exchange is no longer mass suppressed w.r.t. photon exchange and becomes of competitive magnitude. The exchange of the charged W results in events with a spectacular signature due to the escaping neutrino (see Fig. 1b) with generally large p_T. Hence, these charged current events are characterized by a large missing transverse momentum, p_T^{miss}. This characteristic is exploited to isolate charged current events from other processes. A typical charged current event is shown in Fig. 68.

In the past decades the weak charged current has been extensively studied in νN scattering experiments.[134] The total cross section was found to rise linearly with the neutrino beam energy. The cross section has the form

$$\sigma \sim s \frac{1}{(1 + \frac{Q^2}{M_W^2})^2}. \qquad (22)$$

The squared CMS energy, s, is proportional to the incoming lepton energy in a fixed target experiment. Clearly, if $Q^2 \sim M_W^2$ the effect of the W propagator becomes visible and the

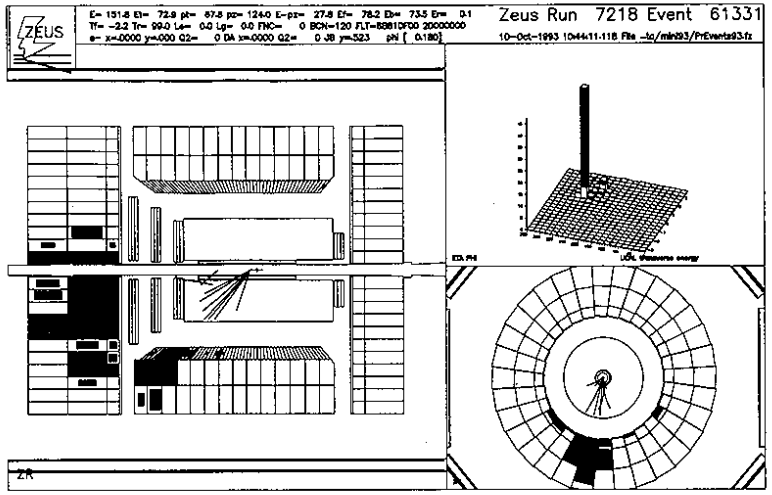

Figure 68: A charged current event in the ZEUS detector.

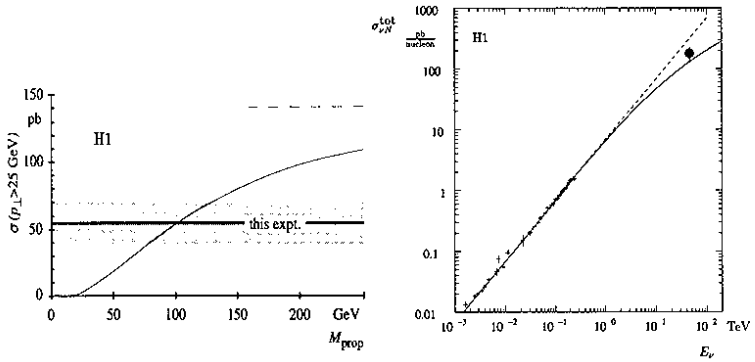

Figure 69: **(left)** Charged current cross-section $\sigma_{CC}(p_t^\nu > 25\,GeV)$ as a function of the propagator mass. The shaded band shows the H1 measurement ($\pm 1\sigma$) and the thin curve the theoretical expectation. The dashed line indicates the asymptotic case $M_{prop} = \infty$.
(right) The energy dependence of the νN cross section. The crosses represent the low energy neutrino data while the full point has been derived from the H1 measurement at HERA. The straight dashed line is the extrapolation from low energies assuming $M_W = \infty$ while the curve represents the predicted cross section including the W propagator with $M_W = 80.22\,\mathrm{GeV}$.

cross section is expected to deviate from linearity. However the beam energies in fixed target experiments were too low to observe the effect of the propagator mass, nowadays expected to be $M_W = 80$. At HERA the equivalent fixed target energy is 50 TeV, so the effect of the W propagator should become visible for the first time in charged current interactions.

The H1 collaboration has measured the total charged current cross section for events with $p_T^{miss} > 25$ GeV.[135] After all selection criteria and background filters 14 events remain in the

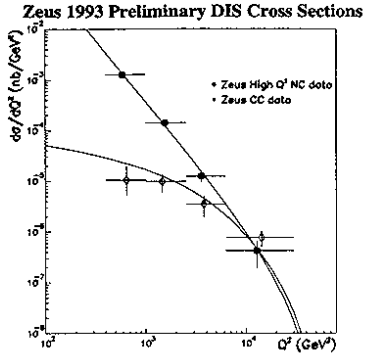

Figure 70: Preliminary cross section from ZEUS for neutral current (full circles) and charged current (open circles) scattering as a function of Q^2 together with predictions from simulation.[100]

sample. The prediction from the electroweak theory for the cross section for $p_T^{miss} > 25$ GeV is 40.9 pb. The measurement gives $55 \pm 15 \pm 6$ pb, in good agreement with theory. The result is shown in Fig. 69a as function of the propagator mass. The result is consistent with a propagator mass of the known W resonance, $M_W = 80$ GeV. An infinite propagator mass is excluded by five standard deviations. The measured ep cross section can be converted to an equivalent νN cross section, by extrapolating to $p_T^{miss} = 0$ and taking into account the relevant flavour contributions. The result is shown in Fig. 69b. It shows that the cross section at HERA deviates from a linear dependence on the neutrino energy.

The ZEUS collaboration has measured the Q^2 dependence[136] of the cross sections $ep \to \nu X$ and $ep \to eX$. As expected the two cross sections seem to become equal at a Q^2 of about 10^4 GeV^2, the scale where the electromagnetic and weak forces are unified. This expectation is confirmed by Born level calculations, obtained with the program LEPTO, shown in the figure. Clearly these are just the first appetizers for electroweak physics at HERA. Much more is expected, when much larger statistics data samples will become available.

7 Searches Beyond the Standard Model

For every new high energy collider the search for new particles and phenomena is a "must". Due to its large centre of mass energy and the presence of an electron in the initial state, HERA is particularly suited to look for leptoquarks (gluons) and excited leptons, which can be produced either by fusion of the incoming lepton with a quark (gluon) of the proton, or fusion of the lepton with an exchanged boson.

The 1993 data have been analysed but so far no clear signal has been found for any of these channels. Limits have been deduced[137,138] which depend on the coupling of these new particles with the lepton and quark or exchanged boson. For leptoquarks the results are shown in Fig. 71 and for leptogluons in Fig. 72 for the H1 experiment. For couplings as large as the electromagnetic coupling, the excluded mass range is typically below 230 GeV for various types of scalar and vector leptoquarks. New limits for excited electrons and neutrinos are shown in Fig. 73 from ZEUS. Both experiments have produced similar limits on leptoquarks and excited leptons.

ZEUS has presented results on the first search for excited quark (q^*) production through electroweak coupling. They are complementary to searches at $p\bar{p}$ colliders – which reached

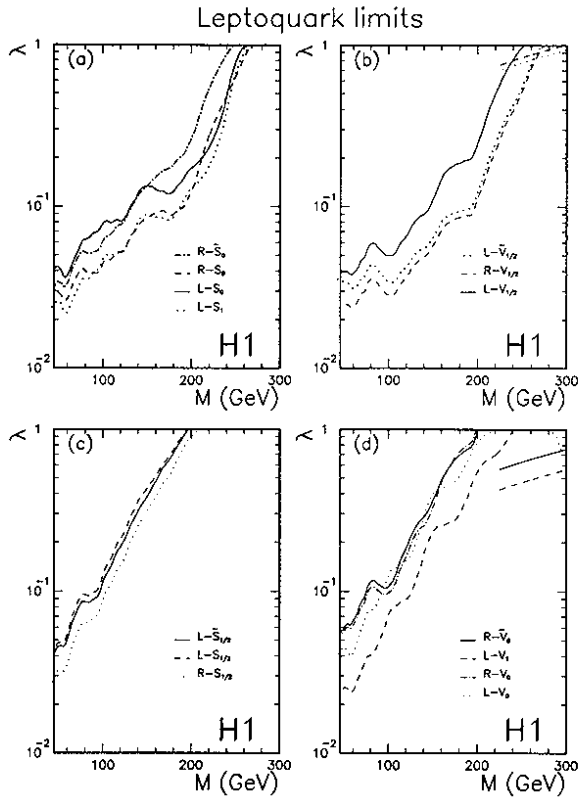

Figure 71: Upper limits at 95% C.L. from H1 as a function of mass on the couplings $\lambda_{L,R}$ for scalar and vector leptoquarks decaying into (a,b) lepton+q and (c,d) lepton+$\bar{q}$. The regions above the curves are excluded. The limits on λ_L for S_0, S_1, V_0 and V_1 combine $e+X$ and $\nu+X$ decays. The additional lines at high masses in (b) and (d) represent the result of the indirect search via the contact term analysis.

a mass limit of 540 GeV[139] – and hold for excited quark production via the gluon coupling. The limits are shown in Fig. 74.

The H1 collaboration made a search for R-parity violating supersymmetric squarks. In the accessible range of couplings, the squarks have mainly leptoquark-like signals. The rejection limits obtained for leptoquarks can thus be re-interpreted as a function of the squark masses. The results are shown in Fig. 75. Assuming couplings of electromagnetic strength masses of squarks in an R-parity violating susy environment below about 240 GeV can be excluded, depending on the photino mass

The search for new bosons or eq compositeness can be considerably extended beyond the kinematic production limit of HERA through the study of indirect effects from virtual particle exchange. Such virtual effects are conveniently described by contact interactions and show up as deviations from the Standard Model at high Q^2 values. H1 has made a contact interaction analysis for leptoquarks and compositeness. The leptoquark limits are shown in Fig. 71. The

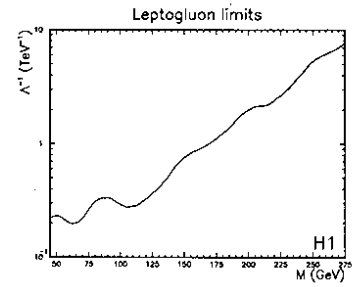

Figure 72: Upper limit at 95% C.L. from H1 for the inverse of the scale parameter Λ versus the mass M for leptogluons. The region above the curve is excluded

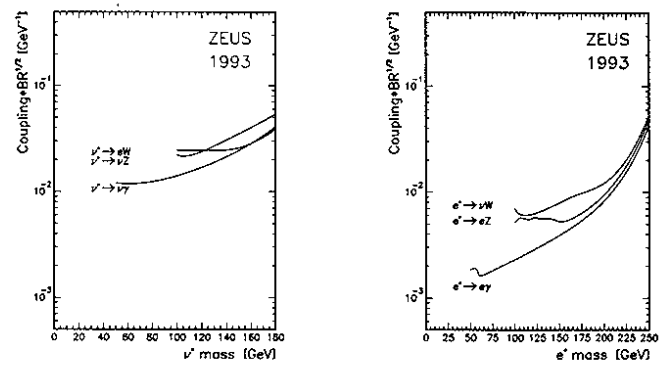

Figure 73: Rejection limits at the 95% C.L. from ZEUS for (a) e^* and (b) ν^* for different decay modes. Regions above the curves are excluded. Decay modes of the W and Z bosons are combined.

result on the compositeness scale Λ is with the 1993 statistics $\Lambda > O(1\text{TeV})$. Similar limits from e^+e^- and $p\bar{p}$ colliders yield values roughly a factor 2 to 3 higher.

In the 1994 data one event was found with an unusual topology. The event is shown in Fig. 76, where one sees a large hadronic activity on one side of the detector and an isolated penetrating track on the other side of the detector. This penetrating particle is found to be compatible with a high energy muon emerging from the interaction vertex. No scattered electron is seen the detector. The hadronic system and the muon candidate have a large transverse momentum, $p_T = 41.1 \pm 4.2$ GeV and for $p_T = 23.4 \pm 2.4^{+7}_{-5}$ GeV, for the hadronic system and muon respectively. The azimuthal angle between the muon and hadronic system is 183^0, i.e. they are essentially back to back. There is room for missing longitudinal momentum in the electron beam direction of more than 20 GeV and $p_T^{miss} = 18.7 \pm 4.8^{+5}_{-7}$ GeV. The muon candidate has the same charge as the incident lepton (which is a positron, since this event

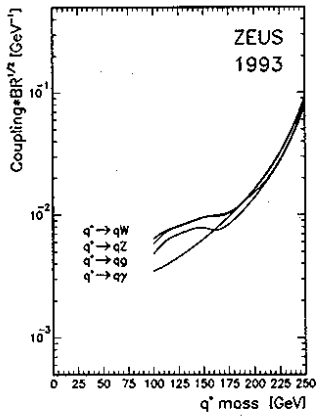

Figure 74: Rejection limits at the 95% C.L. from ZEUS for q^* for different decay modes. Regions above the curves are excluded. Note that these are limits on q^* production through electroweak coupling.

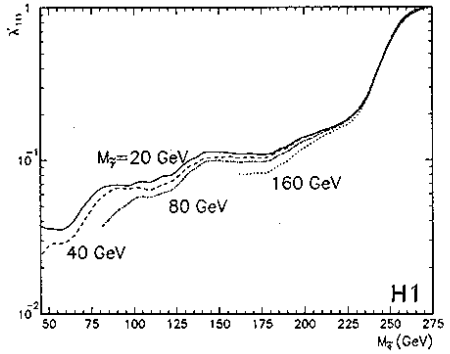

Figure 75: Rejection limits at the 95% C.L. from H1 for the couplings λ'_{111} as a function of the squark mass for various values of the photino mass. Regions above the curves are excluded. Note that these limits combine all charged and neutral decays of the $\tilde{d}$ and $\tilde{u}$.

was found in the second part of the 1994 luminosity period). This event has been analysed[140] and the most probable Standard Model interpretation is the production and leptonic decay of a W boson, for which 0.03 events are expected given the total collected luminosity. Evidently this small expectation value leaves room for speculation on more exotic interpretations. To settle this matter the approximately fivefold larger luminosity for the 1995 data taking period is eagerly awaited for...

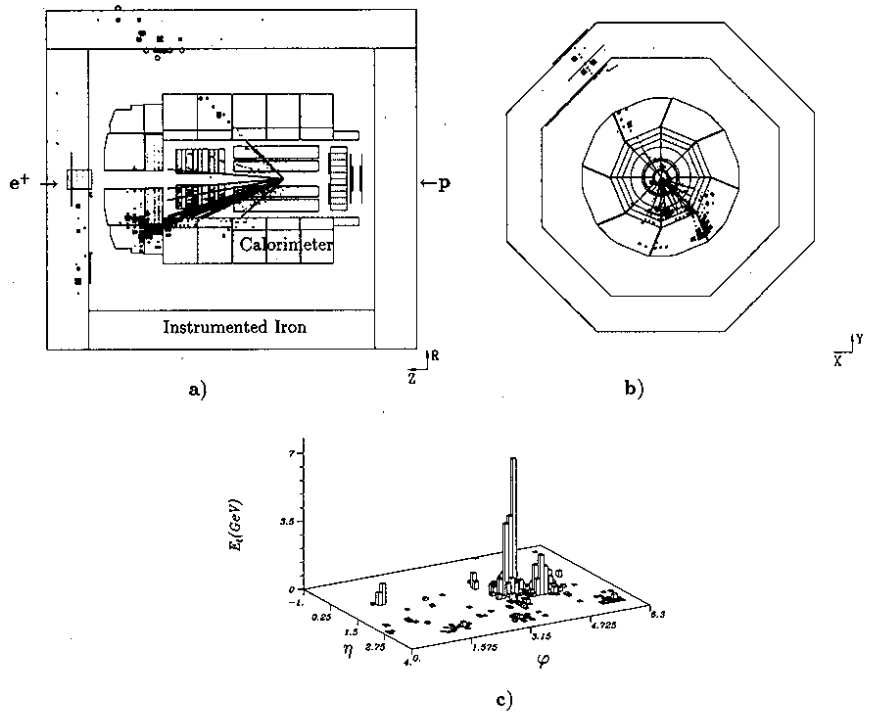

Figure 76: Event display of the "muon" event observed in the H1 detector: (a) $R-z$ view (b) $R-\varphi$ view and (c) transverse calorimetric energy.

8 Conclusions

After two years of experimenting at the new ep collider HERA many new results have been obtained. In this report we have presented results on interactions of high energy photons with matter, and showed that similar to hadronic interactions, hard scattering is observed in these collisions. The different photoproduction processes have been isolated, and a first attempt was made to measure the structure of the photon at HERA. A new region has been explored for deep inelastic scattering interactions. The proton structure is probed to very small values of Bjorken-x, showing a large increase of with decreasing x. Events with a large rapidity gap have been observed and are identified as diffractive scattering. These events eventually will

allow us to study structure of the Pomeron, an object used in soft hadronic physics to describe diffractive phenomena, but so far rather poorly known. The first electroweak results became available by studying the production of charged current events. Searches for new, exotic phenomena were made, but no evidence for the breakdown of the standard model has been found. Many of the topics in this report will strongly benefit from the increase in luminosity of HERA, expected for the next year(s). Clearly, HERA and its physics program still have a bright future ahead.

Acknowledgment I would like to thank my colleagues from the H1 and ZEUS collaborations for their efforts in accumulating this large amount of nice results. I wish to thank in particular J. Bartels, D. Cussans, M. Erdmann, J. Feltesse, T. Haas, H. Jung, M. Klein, M. Kuhlen, J. Kurzhoefer, M. Leenen, A. Martin, R. Martin, J. Phillips, G. Rädel, J. Riedlberger, H. Rick, U. Stösslein and J. Withmore for discussion, critical reading of the text and valuable help with some of the figures.

References

[1] M. Breidenbach et al., Phys. Rev. Lett. **23** (1969) 935.

[2] R.P. Feynmann, *Photon-Hadron Interactions*, W.A. Benjamin Co., New York, (1972).

[3] M. Gell-Mann and Y. Ne'eman, *The Eightfold Way*, W.A. Benjamin Co., New York, (1964).

[4] F. Jacquet and A. Blondel, Proceedings of *the Study for an ep Facility for Europe*, ed. U.Amaldi, DESY 79/48 (1979) 391.

[5] J.Bartels and J.Feltesse, Proceedings of the Workshop *Physics at HERA*, ed. W. Buchmüller and G. Ingelman, Hamburg (1992) 133;
Workshop on *Deep Inelastic Scattering*, April 1992, Teupitz, Germany, J. Blümlein and T. Riemann editors;
E.M. Levin, Proceedings of the Internatinal Conference on *QCD, 20 Years Later*, ed. P.M. Zerwas and H.A. Kastrup, Aachen (1992).

[6] A.A. Sokolov and M. Ternov, Dokl. Sov. Akad. Nauk. **8** (1964) 1203.

[7] H1 Collaboration, *The H1 Detector at HERA*, DESY preprint DESY 93-103 (1993).

[8] ZEUS Collaboration, *The ZEUS Detector*, Status Report (1993).

[9] H1 Calorimeter Group, B. Andrieu et al., NIM **A336** (1993) 460.

[10] H1 Calorimeter Group, B. Andrieu et al., NIM **A336** (1993) 499.

[11] H. Bethe and W. Heitler, Proc. Roy. Soc. **A146** (1934) 83.

[12] H1 Collaboration, T. Ahmed et al., Phys. Lett. **B299** (1993) 374.

[13] ZEUS Collaboration, M. Derrick et al., Phys. Lett. **B293** (1992) 465.

[14] H1 Collaboration, T. Ahmed et al., *Experimental Study of Hard Photon Radiation Processes at HERA*, DESY preprint DESY-95-024 (1995).

[15] ZEUS Collaboration, M. Derrick et al., *Measurement of the Proton Structure Function F_2 from the 1993 HERA Data*, DESY preprint DESY 94-143 (1994).

[16] HERMES Collaboration, *A Proposal to Measure the Spin Dependent Structure Functions of the Neutron and the Proton at HERA*, DESY PRC 93/06 (1993).

[17] HERA-B Collaboration, *HERA-B: An Experiment to Study CP Violation in the B System Using an Internal Target at the HERA Proton Ring*, DESY-PRC 94/02 (1994).

[18] G. Schuler and T. Sjöstrand, Phys. Rev. **D49** (1994) 2257.

[19] J.K. Storrow, J. Phys. **G19** (1993) 1641.

[20] J.D. Bjorken, *Geometry of Multihadron Production*, summary talk of the 24th International Symposium on Multiparticle Dynamics, Vietri Sul Mare, September 1994.

[21] I. Pomeranchuck, Ya. JETP, 7 (1958), 499.

[22] A. Donnachie and P.V. Landshoff, Phys. Lett. **B296** (1992) 227.

[23] G. Yodh, Nucl. Phys. **B** (Proc. Suppl.) 12 (1990) 277.

[24] A. Levy, Proceedings of the Workshop *Physics at HERA*, ed. W. Buchmüller and G. Ingelman, Hamburg (1992) 481.

[25] H. Abramovicz et al., Phys. Lett. **B269** (1991) 465.

[26] C.F Weizsäcker, Z. Phys. **88** (1934) 612; E.J. Williams, Phys. Rev. **45** (1934) 729.

[27] ZEUS Collaboration, M. Derrick et al., Z. Phys. **C63** (1994) 391.

[28] ZEUS Collaboration, F. Barreiro et al., *New Results from HERA*, DESY preprint, DESY 94-204 (1994).

[29] P. Söding, Phys. Lett. **B19** (1966) 702.

[30] Z. Koba, H.B. Nielsen, P. Olesen, Nucl. Phys. **B40** (1972) 317.

[31] E.A. De Wolf, contributed talk to ICHEP94, 27th Int. Conf. on High Energy Physics, Glasgow, July 1994, to be published.

[32] B.A. Kniehl and G. Kramer, Z. Phys. **C62** (1994) 53.

[33] H1 Collaboration, I. Abt et al., Phys. Lett. **B328** (1994) 176.

[34] M. Glück, E. Reya and A. Vogt, Z. Phys. **C53** (1992) 651.

[35] H. Abramowicz, K. Charchula and A. Levy, Phys. Lett. **B269** (1991) 458.

[36] J. E. Huth et al., Fermilab-Conf-90/249-E (1990).

[37] H. Bengtsson and T. Sjöstrand, Comp. Phys. Comm. **46** (1987) 43;
T. Sjöstrand, CERN-TH-6488-92 (1992).

[38] ZEUS Collaboration, M. Derrick et al., Phys. Lett. **B342** (1995) 417.

[39] H1 Collaboration, V. Brisson et al., *New Results from HERA on Deep Inelastic Scattering at low x, the Proton Structure Function, Jets in Photoproduction, Heavy Flavour Production and Searches for New Particles*, DESY preprint DESY 94-187 (1994).

[40] C. Marchesini et al., Comp. Phys. Comm. **67** (1992) 465.

[41] S. Catani, Yu.L. Dokshitzer and B.R. Webber, Phys. Lett. **B285** (1992) 291.

[42] OPAL Collaboration, R. Akers et al., Z. Phys. **C61** (1994) 199.

[43] AMY Collaboration, R. Tanaka et al., Phys. Lett. **B277** (1992) 215;
AMY Collab., B.J. Kim et al., Phys. Lett. **B325** (1994) 248;
TOPAZ Collab., H. Hayashii et al., Phys. Lett. **B314** (1993) 149;
ALEPH Collab., D. Buskulic et al., Phys. Lett. **B313** (1993) 509;
DELPHI Collab., P. Abreu et al., Phys. Lett. **B342** (1995) 402.

[44] V. Blobel, DESY preprint DESY 84-118, and Proceedings of the 1984 CERN School of Computing, Aiguablava (Spain), CERN 1985.

[45] J.D. Bjorken, talk given at the 21nd Annual SLAC Summer Intitute Topical Conference, Stanford, August 1993.

[46] K. Goulianos, Phys. Rep. **101** (1983) 169.

[47] D. Amati et al., Nuovo Cimento **26** (1962) 896.

[48] F. E. Low, Phys. Rev. **D12** (1975) 163; S. Nussinov, Phys. Rev. Lett. **34** (1975) 1286.

[49] G. Ingelman and P. Schlein, Phys. Lett. **B152** (1985) 256.

[50] A. Donnachie and P. V. Landshoff, Phys. Lett. **B191** (1987) 309.

[51] N. N. Nikolaev and B. G. Zakharov, Z. Phys. **C53** (1992) 331.

[52] UA8 Collaboration, A. Brandt et al., Phys. Lett. **B297** (1992) 417.
UA8 Collaboration, R. Bonino et al., Phys. Lett. **B211** (1988) 239.

[53] P. Bruni and G. Ingelman, Proc. of the Europhysics Conference, Marseilles, France, July 1993, p. 595.

[54] H1 Collaboration, T. Ahmed et al., Nucl. Phys.**B435** (1995) 3.

[55] ZEUS Collaboration, M. Derrick et al., *Observation of Hard Scattering in Photoproduction Events with a Large Rapidity Gap at HERA*, DESY preprint DESY 94-210 (1994).

[56] M. Aguilar-Benitez et al., PDG, Phys. Rev. **D45** (1992).

[57] H. Jung, D. Krücker, C. Greub and D. Wyler, Z. Phys. **C60** (1993) 721.

[58] E.L. Berger, D. Jones, Phys. Rev. **D23** (1981) 1521.

[59] M.G. Ryskin, Z. Phys. **C57** (1993) 89.

[60] H1 Collaboration, T. Ahmed et al., Phys. Lett. **B338** (1994) 507.

[61] R.K. Ellis, P. Nason, Nucl. Phys. **B312** (1989) 551.

[62] A.D. Martin, W.J. Stirling, R.G. Roberts, Phys. Lett. **B306** (1993) 145, Erratum **B309** (1993) 492.

[63] ZEUS Collaboration, M. Derrick, et al., *Study of D^{*+-} (2010) production in e p collisions at HERA*, DESY preprint DESY-95-013 (1995).

[64] G. Altarelli, G. Martinelli, Phys. Lett. **B76** (1978) 89.

[65] P. Amaudruz et al., Phys. Lett. **B295** (1992) 159.

[66] J. Bartels and J. Feltesse, Proceedings of the Workshop *Physics at HERA*, ed. W. Buchmüller and G. Ingelman, Hamburg (1992) 133.

[67] V.N. Gribov and L.N. Lipatov, Sov. Journ. Nucl. Phys. **15** (1972) 438 and 675;
G. Altarelli and G. Parisi, Nucl. Phys. **B126** (1977) 298 ;
Yu.L. Dokshitzer, Sov. Phys. JETP **46** (1977) 641.

[68] E.A. Kuraev, L.N. Lipatov and V.S. Fadin, Phys. Lett. **B60** (1975) 50;
Zh.E.T.F **72** (1977) 377.

[69] V.N. Gribov, E.M. Levin and M.G. Ryskin, Phys. Rep. **100** (1983),1.

[70] H1 Collaboration T. Ahmed et al., *A Measurement of the Proton Structure Function F_2*, DESY preprint DESY 95-006 (1995).

[71] J. Feltesse, in Proceedings of the Workshop Proc. HERA Workshop (DESY, 1987) p.33.

[72] D. Yu. Bardin et al., Z. Phys. **C42** (1989) 679;
M. Böhm and H. Spiesberger, Nucl. Phys. **B294** (1987) 1081;
J. Blümlein, *$O(\alpha^2)$ Radiative Corrections to Deep Inelastic ep scattering for different kinematical variables*, DESY preprint DESY 94-044 ;
A. Akhundov et al., CERN Preprint CERN-TH.7339/94.
H. Spiesberger et al., Proceedings of the Workshop *Physics at HERA*, ed. W. Buchmüller and G. Ingelman, Hamburg (1992) 798.

[73] S. Bentvelsen, P. Kooijman and J. Engelen, Proceedings of the Workshop *Physics at HERA*, ed. W. Buchmüller and G. Ingelman, Hamburg (1992) 23.
K.C. Hoeger, Proceedings of the Workshop *Physics at HERA*, ed. W. Buchmüller and G. Ingelman, Hamburg (1992) 43.

[74] U. Bassler and G. Bernardi, DESY preprint DESY 94-231 (1994), submitted to Nucl. Inst. and Meth.

[75] H1 Collaboration, I. Abt et al., Nucl. Phys. **B407** (1993) 515.

[76] ZEUS Collaboration, M. Derrick et al., Phys. Lett **B316** (1993) 412.

[77] E665 Collaboration, A.V. Kotwal et al., *Proton and Deuteron Structure Functions in Muon Scattering at 470 GeV/c*, presented at the XXXth Rencontres de Moriond, QCD in High Energy Interactions, March 1995, FERMILAB-Conf-95/046-Expt.

[78] L.W. Whitlow et al., Phys. Lett. **B282** (1992) 475.

[79] BCDMS Collaboration, A.C. Benvenuti et al., Phys. Lett. **B223** (1989) 485.

[80] NMC Collaboration, P. Amaudruz et al., Phys. Lett. **B295** (1992) 159.

[81] A.D. Martin, W.J. Stirling, R.G. Roberts, Phys. Rev. **D47** (1993) 867.

[82] M. Glück, E. Reya and A. Vogt, Z. Phys. **C53** (1992) 127 and Phys. Lett. **B306** (1993) 391.

[83] M. Glück, E. Reya and A. Vogt, *Dynamical Parton Distributions of the Proton and Small-x Physics* DESY preprint DESY-94-206 (1994).

[84] A.D. Martin, W.J. Stirling, R.G. Roberts, Proc. Workshop on *Quantum Field Theoretical Aspects of High Energy Physics*, Kyffhässer, Germany, eds B. Geyer and E.M. Ilgenfritz, Leipzig (1993) p.11.

[85] A. Capella et al., Phys. Lett. **B337** (1994) 358.

[86] A. Donnachie and P. V. Landshoff, Z. Phys. **C61** (1994) 139.

[87] A.J. Askew, J. Kwieciński, A.D. Martin, P.J. Sutton, Phys. Rev. **D47** (1993) 3775;
A.J. Askew, K. Golec-Biernat, J. Kwieciński, A.D. Martin, P.J. Sutton, Phys. Lett. **B325** (1994) 212;
A.J. Askew, J. Kwieciński, A.D. Martin, P.J. Sutton, Phys. Rev. **D49** (1994) 4402.

[88] N.N. Nikolaev and B.G. Zakharov, Phys. Lett. **B327** (1994) 149.

[89] K. Golec-Biernat, M.W. Krasny and S. Riess, Phys. Lett. **B337** (1994) 367.

[90] W. Zhu, D. Xue, Kang-Min Chai and Zai-Xin Xu, Phys. Lett. **B317** (1993) 200.

[91] D.W. McKay and J.P. Raltson, Nucl. Phys. **B** (Proc. Suppl.) 18C (1990) 86.

[92] R.D. Ball and S. Forte, Phys. Lett. **B335** (1994) 77;
R.D. Ball and S. Forte, Phys. Lett. **B336** (1994) 77.

[93] A. De Rujula et al., Phys. Rev. **D10** (1974) 1649;
F.Wilczek and A.Zee, Phys. Rev. **D10** (1974) 1649;
A.Zee, F.Wilczek and S.B.Treiman, Phys. Rev. **D10** (1974) 2881.

[94] R.D. Ball and S. Forte, CERN preprints CERN-TH.7421/94 and CERN-TH.7422/94.

[95] K. Prytz, Phys. Lett. **B311** (1993) 286;
K. Prytz, Rutherford-Appleton Laboratory preprint : RAL-94-036.

[96] H1 Collaboration, I. Abt et al., Phys. Lett. **B321** (1994) 161.

[97] K. Golec-Biernat, Phys. Lett. **B328** (1994) 495.

[98] R.K. Ellis, Z. Kunszt and E.M. Levin, Fermilab preprint : Fermilab-PUB-93/350-T.

[99] A.H. Mueller, Nucl. Phys. **B** (Proc. Suppl.) 18C (1990) 125.

[100] G. Ingelman, LEPTO 6.1, Proceedings of the Workshop *Physics at HERA*, ed. W. Buchmüller and G. Ingelman, Hamburg (1992) 1366.

[101] L. Lönnblad, ARIADNE version 4.03, Comp. Phys. Commun. 71 (1992) 15, and references therein.

[102] L. Lönnblad, Z. Phys. **C65** (1995) 285;
A. H. Mueller, Nucl. Phys. **B415** (1994) 373.

[103] B.R. Webber, J. Phys. **G19** (1993) 1567.

[104] H1 Collaboration, I. Abt et al., Z. Phys. **C64**, (1994) 377.

[105] DELPHI Collaboration, P. Abreu et al., Phys. Lett. **B311** (1993) 408.

[106] ZEUS Collaboration, M. Derrick et al.,*Measurement of multiplicity and momentum spectra in the current fragmentation region of the Breit frame at HERA*, DESY preprint DESY 95-007 (1995)

[107] ZEUS Collaboration, M. Derrick et al., Phys. Lett. **B306**, (1993) 158.

[108] H1 Collaboration, I. Abt et al., Z. Phys. **C61**, (1994) 59.

[109] JADE Collaboration, W. Bartel et al., Z. Phys. **C33** (1986) 23.

[110] ZEUS Collaboration, M. Derrick et al., *Jet production in high Q^2 deep inelastic e p scattering at HERA*, DESY preprint DESY-95-016 (1995).

[111] D. Graudenz, Phys. Lett. **B256**, (1991) 518;
D. Graudenz, Phys. Rev. **D49**, (1994) 3291;
D. Graudenz, PROJET4.1, CERN-TH.7420/94.

[112] T. Brodkorb, J.G. Körner, Z. Phys. **C54**, (1992) 519;
T. Brodkorb, E. Mirkes, Univ. of Wisconsin, MAD/PH/820 (1994).

[113] H1 Collaboration, T. Ahmed et al., *Determination of the Strong Coupling Constant from Jet Rates in Deep Inelastic Scattering*, DESY preprint DESY 94-220 (1994).

[114] S. Bethke, J.E. Pilcher, Annual Review of Nuclear and Particle Science **42**, 251 (1992).

[115] V. Hedberg, G. Ingelman, C. Jacobsson and L. Jönsson, Proceedings of the Workshop *Physics at HERA*, ed. W. Buchmüller and G. Ingelman, Hamburg (1992) 331.

[116] C. Jacobsson, *Jet Azimuthal Angle Asymmetries in Deep Inelastic Scattering as a Test of QCD*, Phd thesis, University of Lund, (1994), unpublished.

[117] J. Bartels, H. Lotter, Phys. Lett. **B309** (1993) 400.

[118] K. Golec-Biernat, J. Kwieciński, A. D. Martin and P. J. Sutton, Phys. Rev. **D50** (1994) 217;
K. Golec-Biernat, J. Kwieciński, A. D. Martin and P. J. Sutton, Phys. Lett. **B335** (1994) 220.

[119] A.H. Mueller, J. Phys. **G17** (1991) 1443;
J. Bartels, A. De Roeck, M. Loewe, Z. Phys. **C54** (1992) 635;
W.K. Tang, Phys. Lett. **B278** (1992) 363.

[120] J. Kwieciński, A.D. Martin, P.J. Sutton, Phys. Rev. **D46** (1992) 921.

[121] H. Jung, *Hard diffractive scattering in high-energy e p collisions and the Monte Carlo generation RAPGAP*, DESY preprint DESY 93-182.

[122] ZEUS Collaboration, M. Derrick et al., Phys. Lett. **B315** (1993) 481.

[123] H1 Collaboration, A. De Roeck, *Results from the H1 Experiment*, to appear in Proc. of the Europhysics Conf. on HEP, Marseille, France, July 1993. DESY preprint : DESY 94-005 (1994);
J. B. Dainton, *Results from the H1 Experiment at HERA*, in Proc. XVI International Symposium on Lepton Photon Interactions, Cornell, Ithaca, USA, August 1993.

[124] G. Ingelman and K. Prytz, Z. Phys. **C58** (1993) 285.

[125] M.G.Ryskin and M.Besançon, Proceedings of the Workshop *Physics at HERA*, ed. W. Buchmüller and G. Ingelman, Hamburg (1992) 215 and references therein.

[126] H1 Collaboration, T. Ahmed et al., Nucl. Phys. **B429** (1994) 477.

[127] S.J. Brodsky et al., Phys. Rev. **D50** (1994) 3134.

[128] NMC Collaboration, M. Arneodo et al., *Exclusive ρ^0 and phi Muoproduction at Large Q^2*, CERN preprint CERN-PPE-94-146 (1994).

[129] EMC Collaboration, J.J. Aubert et al., Phys. Lett. **B161** (1985) 203 and J. Ashman et al., Z. Phys. **C39** (1988) 169.

[130] NMC Collaboration, P. Amaudruz et al., Z. Phys. **C54** (1992) 239.

[131] J. Nemchik, N.N. Nikolaev and B.G. Zakharov, Phys. Lett. **B341** (1994) 228.

[132] G. Alberi and G. Goggi, Phys. Rep. **74** (1981) 1.

[133] H1 Collaboration, T. Ahmed et al. *First Measurement of the Deep Inelastic Structure of Proton Diffraction.*, DESY preprint DESY 95-036 (1995).

[134] For a review see D. Haidt and H. Pietschmann, Lanolt-Börnstein New Series I/10, Springer (1988).

[135] H1 Collaboration, T. Ahmed et al., Phys. Lett. **B324** (1994) 241.

[136] T. Haas, *Recent Results from ep Scattering at HERA*, DESY preprint DESY 94-160 (1994).

[137] H1 Collaboration, T. Ahmed et al., Phys. Lett. **B340** (1994).
H1 Collaboration, T. Ahmed et al., Z. Phys. **C64** (1994) 545.

[138] ZEUS Collaboration, M. Derrick et al., *A Search for Excited Fermions in Electron-Proton Collisions at HERA* DESY preprint DESY 94-175.

[139] CDF Collaboration, F. Abe et al., Phys. Rev. Lett. **72** (1994) 3004.

[140] H1 Collaboration, T. Ahmed et al., *Observation of an $e^+p \to \mu^+X$ Event with High Transverse Momenta at HERA* DESY preprint DESY 94-248 (1994).